University of Alberta

Surface Spectroscopic Studies of Molecular Recognition on Bare and Functionalized Silica

by

Md. Shafiul Azam

A thesis submitted to the Faculty of Graduate Studies and Research
in partial fulfillment of the requirements for the degree of

Doctor of Philosophy

Department of Chemistry

©Md. Shafiul Azam
Fall 2013
Edmonton, Alberta

Abstract

Understanding the molecular recognition processes at the solid/liquid interface is of central importance in numerous environmental, biological and materials applications. We studied the unorthodox behavior of molecules and ions at the silica/liquid interfaces using surface specific spectroscopic techniques. For instance, we used nonresonant second harmonic generation (SHG) spectroscopy to investigate the effect of specific cations on the acid-base equilibria of the silica/water interface. The silanol groups on planar silica are known to exhibit two acid dissociation constants with pK_a values of ~4 and ~9. We observed that varying the alkali chloride significantly changed the effective pK_a values for the less acidic silanols by as much as 2.5 log units.

The effect of anions on the acid-base behavior of the silica/water interface was even more striking. Varying the halides in the aqueous phase led to drastically different effective pK_a values for both types of silanol sites. The acid-base titration curves became increasingly sharp with increasing halide size, which was indicative of cooperative acid-base behavior. This has been the first clear observation of cooperative acid-base behavior at a mineral oxide interface.

Next, to study the molecular recognition processes on a functionalized surface we selected DNA-tethered silica as our surface of interest. Utilizing the molecular specificity of resonant SHG we monitored the hybridization and thermal dissociation of DNA immobilized at the silica/water interface in real time. The timescale of hybridization for immobilized DNA was comparable to that of

gold-supported DNA. However, the measured dissociation temperature of DNA immobilized at the silica/water interface was significantly lower than what is usually observed for gold tethered DNA, which we attributed to the additional charge repulsion between silica and the hybridizing complementary DNA.

To increase complexity at the silica/liquid interface we introduced an orthogonally reactive azide-amine mixed monolayer, which provided a general starting point for synthesizing mixed monolayers with controlled ratios. Using X-ray photoelectron spectroscopy, we determined the azide/amine surface ratio as well as the reactivity of the functional groups in the mixed self-assembled monolayer (SAM). The subsequent functionalization of this mixed monolayer generated a bifunctional surface with a similar functional group ratio to the azide-amine precursor SAM.

Acknowledgements

First and foremost I would like to express my sincere gratitude to my advisor Julianne Gibbs-Davis for her stimulating inspiration, worthy criticism and wise advice throughout my entire graduate career. I feel fortunate to be the first graduate student of Juli's group at University of Alberta. Her confidence in my chemistry skills and abilities has been an invaluable source of motivation towards the successful completion of this prestigious degree.

I am very fortunate to have Professors Yunjie Xu, Christopher Cairo, and Gabrial Hanna as my thesis committee members. I am grateful for your constant support, critiques, and suggestions to improve my research in many aspects. A cordial thanks is also extended to Professor John Davis of physics for his continuous encouragement throughout my research.

I also must acknowledge the support of my colleagues, in particular Kausar, Delwar, Champika, Li, Julian, Yimeng, Akemi, and Sean. You all have been so amazing throughout this entire PhD journey.

Most importantly, I must thank my family and friends for helping me stay focused on my research. I express heartfelt thanks to my wife Nazia, for her tireless emotional support. And thanks to our small son Arsh, for adding so much fun in my life that kept me always cheered up. I would like to thank my mother, parents in law and siblings for their unending love, support and sacrifice. Without them I wouldn't be able to see this day of the completion of my PhD.

Finally, I thank almighty Allah for His unbound blessings in my life.

This thesis is dedicated to the memory of my father,

Dr. Ali Ahmed (1939 – 2001),

the first person who inspired my fascination in nature and science

Table of Contents

Chapter 5 Increasing complexity at the silica/liquid interface using orthogonally reactive azide-amine mixed monolayers ...……….…... 156

List of Tables

List of Figures

List of Schemes

CHAPTER 1

Introduction

1.1 The Solid/Liquid Interface

Understanding the confined environment at the interface of solid and liquid phases is critical to understand a number of phenomena encountered in physical, chemical, and biological processes that occur in nature.[1,2] The chemistry of the solid/liquid interface is quite complex and in most cases is yet in the process of comprehensive understanding. The source of complexity is partially that the molecules at the interface no longer behave like their counterparts in the bulk and rather show different properties depending on the nature of the interface. For instance, the hydrogen-bonding structure of interfacial water is substantially different form that of bulk water when in contact with a charged solid surface,[3-6] or even when in the proximity of apparently an inert surface, such as a simple metal.[7] Elucidating interfacial molecular processes has been important in many applications such as heterogeneous catalysis, biological transport across the cell membrane, and electrochemistry occurring at various solid/liquid interfaces. Among all the solid/liquid interfaces, naturally occurring mineral oxide/water interfaces have attracted the attention of researchers in the last several decades because of their importance in many geochemical and environmental applications.[8] The presence of diverse inorganic and organic species in the aqueous phase makes the systems more complex by affecting the inherent properties of the mineral oxide surfaces.[8,9] Although much work has been done studying silica and functionalized silica interfaces, many techniques are not intrinsically sensitive to the small region that represents the interface.[10-18] Consequently, these methods can provide indirect information about the

interfacial processes, which leaves many questions still unanswered.

The focus of this thesis has been to investigate molecular and ion recognition processes at silica/liquid interfaces using surface-specific spectroscopic methods. The first part is focused on monitoring acid-base processes at the bare silica/aqueous interface, whereas the second half is aimed at understanding molecular recognition at more complex functionalized silica interfaces. Specifically, we studied the effects of specific ions and the electrolyte concentration on the bimodal acid-base behavior of the silica/water interface to significantly increase the level of scientific understanding regarding the environmental and geochemical processes on silica surface.[9,19] In addition to the environmental significance, silica has also been used as the support material for immobilizing organic molecules in many applications ranging from catalysis[20] to diagnostics.[21,22] In the later part of this thesis, we studied the kinetic and thermodynamic behavior of DNA immobilized at the silica/water interface, which is important in optimizing DNA biodetection platforms using DNA chips and microarrays. Finally, in this thesis we described our strategy of synthesizing bifunctional self-assembled monolayers (SAMs) with tunable ratios of functional groups that are desirable in the construction of new materials, such as biomimetic responsive surfaces.

1.2 Methods for Studying the Acid-Base Behavior and Dissolution Properties of the Bare Silica/Water Interface

Because of the imperative role of the silica/water interface in the natural

environment, the properties of silica have been the subject of research for the last several decades. A variety of techniques have been applied to the study of deprotonation and dissolution processes at the silica/water and functionalized silica/water interface. These bulk and surface specific techniques described in this section can provide complimentary pieces of information, which can aid in forming a complete picture of these interfacial processes.

Nuclear magnetic resonance (NMR) is a widely used spectroscopic technique for studying bulk systems. However, NMR has also been used to study the silica gel/liquid interface. Using ^{29}Si – ^1H cross polarization one can avoid detection of silicon nuclei from the bulk and instead the resultant ^{29}Si NMR spectra reflects only surface silicon atoms that are nearer to the hydroxyl protons. ^{29}Si NMR studies combined with cross polarization and magic-angle spinning provide spectra with a useful level of structural resolution, allowing the detailed study of surface silanol structures on the silica gel surface.[11-14,23,24] One of these studies suggested the presence of three silanol groups on the silica surface which are $-SiOH$, $-SiOH_2^+$, and $-SiO^-$ at neutral pH.[14] Another study measured the surface concentration of the hydroxyl groups, which ranged between 5 and 10 groups / nm^2, as a function of dehydrating temperature.[12]

Another linear spectroscopic method, fourier transform infrared (FT-IR) absorbance spectroscopy has been utilized to study the solid/liquid interface of aerosol silica and silica gel morphologies in the presence of water. FT-IR studies have been performed to investigate the structural change upon adsorption of water on both the intra-molecular hydrogen-bonded[23,25] and the freely vibrating silanol

groups[26] of the silica materials. While these techniques provide important information regarding the structure of the silica surface, the NMR and FT-IR both spectroscopic techniques are limited to only silica gel, aerosol or nanoparticle morphologies and can not be applied for bigger silica particles or planar silica.

Potentiometric methods have commonly been used to estimate the surface properties of colloidal[27-29] and mesoporous[30] silica. The surface charge density of silica particles is measured with acid-base potentiometric titrations that are carried out using an automated titrator system. To conduct the titration experiments, the silica suspension was first titrated using HCl titrant to expel any remaining dissolved CO_2 and then titrated using NaOH titrant. Surface charge was calculated by determining the difference of the total proton concentration and the free proton and hydroxyl concentrations from the potentiometric measurements of the colloidal suspension. Potentiometric acid-base titration serves as an effective technique for determining the surface charge density as a function of pH, concentration, and identity of electrolytes in the aqueous phase. In addition, the acidity constants of surface hydroxyl groups and surface complexation constants for various metal ions on colloidal silica have also been determined by employing this analytical method by measuring the surface charge density over a pH range of 6.5 to 9.5. However, performing the potentiometric titration below neutral pH is not experimentally possible and another challenge in monitoring acid-base equilibria of silica particles is that the colloidal dispersions are not stable at relatively higher pH.[31,32] As a result, these potentiometric methods can only operate over a limited pH range making this method unsuitable to map out the

entire acid-base equilibrium.

Replacing silica particles with the macroscopic planar silica is a smart way of avoiding aggregate instability. Evanescent wave cavity ring-down spectroscopy (EW-CRDS)[33] uses transparent planar silica as a surface to monitor the deprotonation and estimate changes in the surface charge density of the silica/water interface. In this highly sensitive absorption spectroscopy, a laser pulse is trapped in a detection cavity that consists of a planar silica/water interface under total internal reflection. The light is partially absorbed by the molecules present within the evanescent field at the interface and the absolute absorbance of these molecules is measured from the decay rate of the light within the cavity. To monitor surface deprotonation, a pH-sensitive dye is either adsorbed or tethered to the silica surface and its absorbance at a fixed wavelength is measured using evanescent wave cavity ring-down spectroscopy[33] as a function of solution pH.[33-35] The interfacial pH values are then calculated from the pH-dependent absorbance from the dye tethered to the surface. However, it has been a long debate whether the pK_a of the dye is different or the same at the interface. Assuming the intrinsic pK_a of the dye is unchanged at the interface directly influences the calculations of the surface pH. If that assumption is not correct, then it results in a misinterpretation of the acid-base properties of the interface.[36,37]

Nonlinear optical (NLO) techniques such as second harmonic generation (SHG) serve as label-free and surface-sensitive methods for monitoring the acid-base behavior at the interface.[38-40] Because of their surface specificity NLO

techniques can overcome many other challenges encountered by the bulk analytical and spectroscopic techniques mentioned above. In this thesis nonresonant SHG is used to study the acid-base behavior of the silica/water interface. The technique is discussed below.

1.3 Second Harmonic Generation (SHG) Spectroscopy

SHG is a powerful tool for studying the surface and interface because of its surface specificity. The SHG process is forbidden, within the electric dipole approximation, in centrosymmetric media presented by the bulk.[38,41-44] The SHG response from the interface, therefore, represents only the interfacial region between the bulk phases where centrosymmetry is broken. Second harmonic light is generated when an incident light of frequency ω interacts with the aligned dipoles at the interface causing an induced polarization that oscillates at twice the frequency 2ω ($P_{2\omega}$). Due to the oscillation of this induced polarization a new electric field at 2ω is generated at the interface ($E_{2\omega}$) as shown in Figure 1.1A. The intensity of the SHG response from an interface ($I_{2\omega}$) is proportional to the induced second order polarization ($P_{2\omega}$) as follows:[38,45-48]

$$\sqrt{I_{2\omega}} = E_{2\omega} \; \alpha \; P_{2\omega} = \chi^{(2)} E_\omega E_\omega \qquad (1.1)$$

In this expression, E_ω is the incident electric field and $\chi^{(2)}$ is the nonlinear susceptibility of the interface.
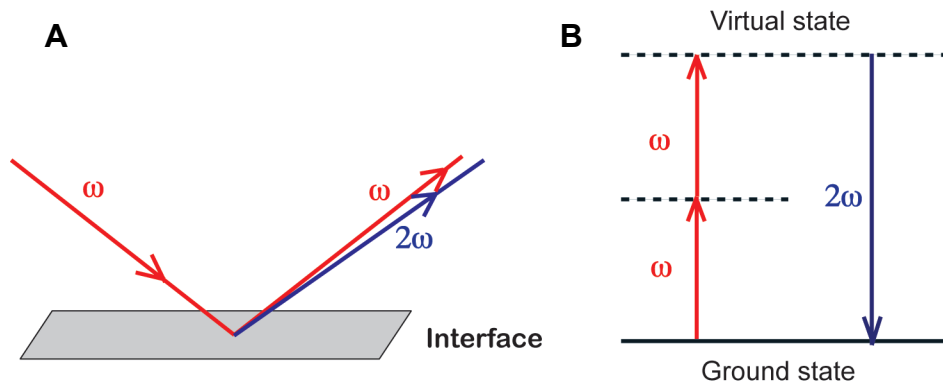
Figure 1.1 A) Geometry of second harmonic generation at the interface. B) Energy-level diagram illustrating nonresonant second harmonic generation.

The SHG process can also be described by considering the interaction of photons as shown in Figure 1.1B. The figure shows that two photons of the same frequency ω are destroyed and a photon of frequency 2*ω* is simultaneously generated in a single quantum-mechanical process. The horizontal solid line represents the atomic ground state and dashed lines represent the virtual states. For the nonresonant SHG both higher energy states are virtual states, whereas for a system where either of these two states is real we observe resonantly enhanced SHG. The first half of this thesis discusses the acid-base behavior of the silica/water interface using nonresonant SHG.

1.3.1 Background Theory of the Nonresonant SHG Spectroscopy

Nonresonant SHG was pioneered by Eisenthal and coworkers as the "$\chi^{(3)}$ technique" originally for SHG studies to study the charge behavior of interfaces. The $\chi^{(3)}$ technique utilizes the dependence of the SHG signal on the interfacial potential that is set up by the interfacial charge density. The charged interface, such as the negatively charged fused silica/aqueous phase interface above pH 2,

8

possesses a static electric field, which sets up an interfacial potential. The presence of an interfacial potential leads to an additional third-order contribution, $\chi^{(3)}E_\omega E_\omega \Phi_0$, to the second harmonic electric field, $E_{2\omega}$. The resultant second harmonic electric field then can be expressed by the following equation:[40,49]

$$\sqrt{I_{2\omega}} = E_{2\omega} \, \alpha \, P_{2\omega} = \chi^{(2)}E_\omega E_\omega - \chi^{(3)}E_\omega E_\omega \Phi_0 \qquad (1.2)$$

Here Φ_0 is the interfacial potential, and $\chi^{(3)}$ is the third-order susceptibility of the interface. The second- and third-order susceptibilities depend on the intrinsic properties of the interface that are assumed to undergo negligible changes throughout the SHG experiments compared to the change in the interfacial potential. On the other hand, the incident electric field is held constant throughout the experiments allowing that any changes in interfacial potential will result in a direct change in the SHG E-field.

We applied this technique to monitor the acid-base behavior of the silica/water interface, and the results are presented in this thesis. At our experimental conditions as described in the following chapters, the interfacial potential turns out to be directly proportional to the charge density on silica surface obeying the constant capacitance model (described in section 1.4) within the pH range from 2 to 13. Again, the charge density represents the fraction of dissociated silanol groups on the surface. Therefore, by monitoring the SHG E-field over this broad pH range we can directly measure the acid dissociation constants for the titration curve of the silica/water interface.

SHG spectroscopy has also been used in determining the kinetic and thermodynamic parameters for the interaction of metal ions, inorganic oxides,

proteins, surfactants, and organic pollutants with the silica/water interface.[50-55] Another NLO technique sum frequency generation (SFG) spectroscopy, on the other hand, has been utilized to study the structure of water and other adsorbed molecules in the confined environment of the silica/water interface with environmentally relevant electrolyte concentrations. This technique is discussed in later section of this chapter.

To gain a more detailed view of the interfacial chemistry involved in the acid-base behavior and metal ion adsorption to silica, the experimental results are often modeled with the aid of surface complexation models.[56,57] Although there are many surface complexation models only a few of them are established and widely used.

1.4 Surface Complexation Models

Surface complexation models (SCMs) are widely accepted among surface scientists because of their capability of relating the experimentally measured acid-base parameters to a molecular view of the mineral oxide/water interface.[8] The SCMs are also capable of simulating the adsorption of aqueous species as a function of changes in model parameters such as solution pH, solute concentrations, and ionic strength.[56,58,59] By modeling the sorption processes, SCMs illustrate the surface interactions with a set of intrinsic thermodynamic constants that are independent of variability in solution compositions. A variety of surface complexation models have been developed over the past few decades that describe the acid base behavior of mineral oxide interfaces in the presence of

different species in solution. However, the three most common SCMs that have widely been used for describing the surface chemical reactions of mineral oxides are the diffuse layer model (DLM), the constant capacitance model (CCM), and the triple layer model (TLM).[56,57]

The application of CCM is restricted to constant high ionic concentration. At the electrolyte concentration greater than 0.1 M the surface charge density on the mineral oxide reaches the upper limit when the metal ions are adsorbed to the negatively charged surface yielding inner-sphere complexes. As depicted in Figure 1.2A, under these conditions the interfacial double layer acts like a capacitor and for a constant electrolyte concentration the capacitance remains constant establishing a charge-potential relationship given by,

$$\sigma_0 = C\Phi_0, \tag{1.3}$$

where σ_0 is the surface charge density at the 0-plane and C is the inner-layer capacitance.
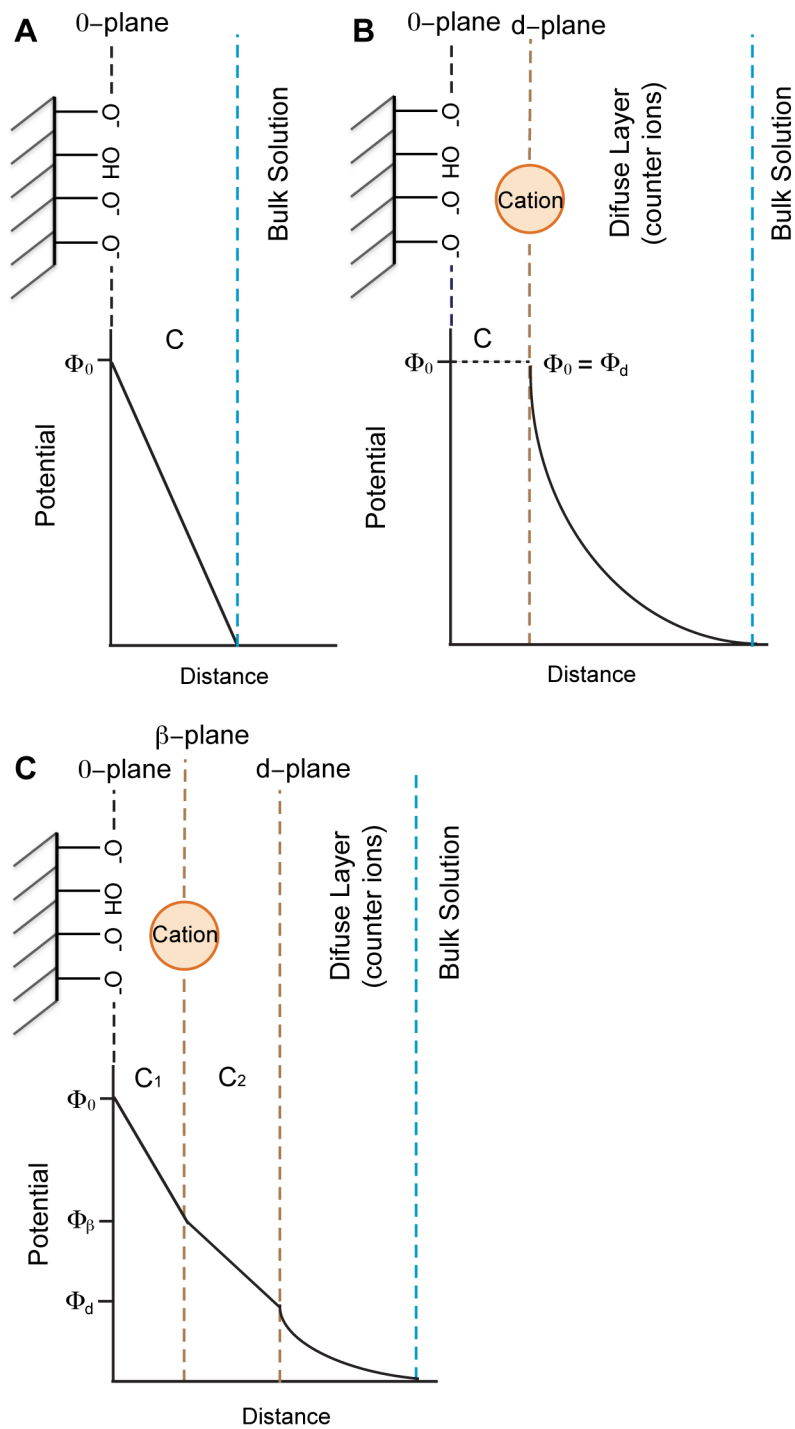
Figure 1.2 Schematic representation of the structure of the mineral oxide/water interface as proposed by A) the constant capacitance model (CCM), B) the diffuse layer model (DLM), and C) the triple layer model (TLM). The notation C represents the inner-layer capacitance.

At very low concentration of electrolytes, when there are not enough cations in the aqueous solution to approach the surface closely to neutralize the negative charge, the compact double layer disappears and a diffuse plane of ions neutralize the surface according to the diffuse double layer model (DLM). This model assumes that the surface charge densities and surface potentials at the 0-plane and at the d-plane are equal ($\sigma_0 = -\sigma_d$ and $\Phi_0 = \Phi_d$) as shown in Figure 1.2B.

In the DLM, the relationship between surface potential and charge density of the mineral oxide/water interface as a function of the screening electrolyte concentration is described by the Gouy-Chapman diffuse charge model.[60-62] According to this model the interfacial potential, Φ_0, is expressed by,

$$\Phi_0 = \frac{2k_B T}{ze} \sinh^{-1}\left(\sigma \sqrt{\frac{\pi}{2\varepsilon\varepsilon_0 T C_{elect}}}\right) \qquad (1.4)$$

where k_B is the Boltzmann constant, e is the elementary charge, ε_0 is the dielectric constant of vacuum, ε is the dielectric constant for bulk water at 25°C, T is the temperature in Kelvin scale, z is the valency of the electrolytes in solution, σ is the surface charge density, and C_{elect} is the electrolyte concentration. The DLM has usually been limited to describe the interfacial potential at low ionic strength as it has been observed that this model overpredicts the diffuse-layer-potential at high ionic strengths.[59]

TLM is relatively more complex among these three models and can be used to model surface reactions over electrolyte concentrations ranging from near zero to 0.1 M.[56,59] SCMs usually describe the electrostatic neutralization of the surface charge by considering the opposite charges in two parallel planes, which

then behave as a parallel plate capacitor. For the silica/water interface the parallel plate capacitors are formed by the negative surface charge coming from the siloxide sites on the silica surface (0-plane) and specifically adsorbed cations (β-plane) as depicted in Figure 1.2C. These two planes correspond to the planes of uniform electric potentials Φ_0 and Φ_β, respectively. The separation of the 0- and β-planes has significant effects on the properties of the silica/water interface and depends on the ion size and hydration state of the adsorbing electrolytes at the β-plane, and also on the nature of the water molecules confined in between the 0- and β-planes.[56] These specific ion effects on the properties of silica/water interface will be discussed in latter sections of this thesis. The third layer consists of the diffusely held counterions (cations in the case of the silica/water interface) that are adsorbed nonspecifically to neutralize the remaining charge. The relationships between surface charge densities and surface potentials are given by the following equations:

$$\sigma_0 = C_1(\Phi_0 - \Phi_\beta) \tag{1.5}$$

and

$$\sigma_d = C_1(\Phi_d - \Phi_\beta) \tag{1.6}$$

where C_1 and C_2 are the inner layer capacitance and diffuse layer capacitance, respectively.

Despite the greater complexity involved in the TLM, incorporation of the surface reactions of the surface hydroxide sites and the aqueous electrolytes makes this model more applicable to systems over a wider range of concentrations compared to other simpler SCMs.

In addition to these three models, other modern SCMs, such as the multi site ion complexation (MUSIC) model or charge distribution multi site ion complexation (CD-MUSIC) model have also been employed widely as frameworks for interpreting ion adsorption on mineral oxide surfaces.[63] The advanced version of the triple layer model (TLM) is the CD-MUSIC model where charges are distributed over several layers or electrostatic planes.[63] A key difference is that the CD-MUSIC model takes into account the chemical nature and arrangement of the surface functional groups. Therefore, the relevant physical or chemical surface parameters are required to utilize this model for a system.

1.5 Acid-Base Behavior of Silica/Water Interface

The adsorption of charged species at the silica/water interface largely depends on the charge density on the silica surface. The charge density, on the other hand, is directly related to the acid-base chemistry of the silanol groups on the surface.[1,8,64] The surface silanol groups, $-SiOH$, deprotonate upon increasing the pH to generate siloxide groups, $-SiO^-$, that eventually lead to a negatively charged surface. Some early NMR[13,14,23] and IR[65-67] spectroscopic studies revealed the presence of two types of silanol groups with two different pK_a values at the silica/water suspension interface. Moreover, second harmonic generation studies of the planar silica/water interface as function of pH also indicated that the silica/water interface possessed two unique acidic sites as shown in scheme 1.1 and Figure 1.5.[39,68,69]
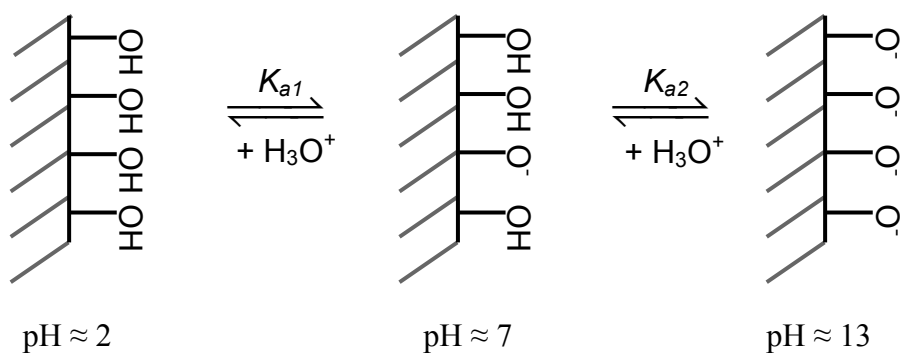
Figure 1.3 Progressive dissociation of the silaol groups with the increase of pH. K_{a1} and K_{a2} represent the acid dissociation constants for more acidic and less acidic sites, respectively.

The presence of two different acidic sites that are chemically identical is unusual for mineral oxide interfaces and more structural elucidation is required to explain this bimodal behavior of the silica/water interface. Another nonlinear optical technique complementary to SHG, vibrational sum frequency generation spectroscopy, allows the vibrational modes of interfacial water molecules to be observed, which provides a means of investigating the interfacial hydrogen-bonding network of water as a function of pH[6,70-73] and electrolyte composition.[15] The resulting SFG spectra reveal the presence of two major populations of water at the silica/water interface, one weakly coordinated and the other strongly coordinated with respect to hydrogen bonds as shown in Figure 1.4A and B, respectively.[70] Based on the sensitivity of these two peaks to changes in pH, weakly hydrogen-bonded water are often associated with the more acidic silanols (lowest pK_a) while silanols in contact with strongly hydrogen-bonded water are thought to be less acidic (highest pK_a).[70,72] Other researchers have suggested that the silanol groups lacking hydrogen bonds are the more acidic.[74] However, recent

ab initio molecular dynamics simulations of the silica/water interface suggested that silanol groups in hydrophobic regions of restructured quartz exhibit the lowest pK_a. The authors also found that the pK_a of the silanols increased as the number of water layers increased.[75]
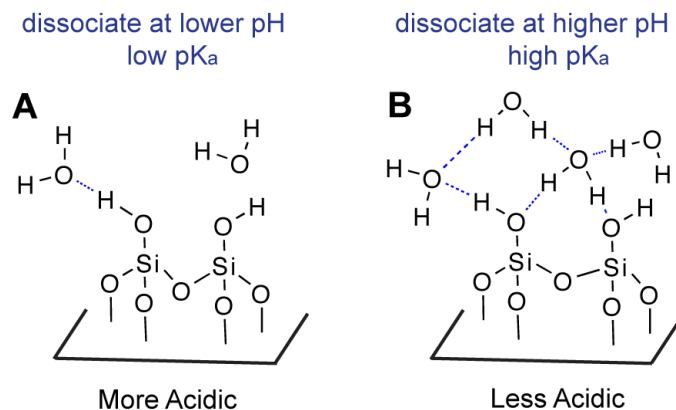
Figure 1.4 Two types of acidic groups at the silica/water interface which are proposed to be (A) silanol groups associated with weakly hydrogen-bonded water resulting in a pK_a ~4-5 and (B) silanol groups associated with strongly hydrogen-bonded water resulting in a pK_a of ~9.

Another recent theoretical work analyzed the SFG spectra of the interfacial water using density functional theory based molecular dynamics simulations of the interface (DFTMD).[76,77] The simulations suggested that the existence of two different acidic sites on the surface is the consequence of the competition of hydrogen-bonds formed between silanol-water and silanol-silanol groups. The in-plane and out-of-plane –SiOH groups form two types of intra-surface hydrogen-bonds as shown in Figure 1.5. The silanols that donate a hydrogen bond in the plane exhibit less acidic character (pK_a of 8.5) by forming weak and long hydrogen-bonds with the nearby water molecules at the interface.

17

In contrast, the out-of-plane silanols with a pK_a of 5.6 form strong and short hydrogen-bonds with the interfacial water molecules as depicted in Figure 1.5.
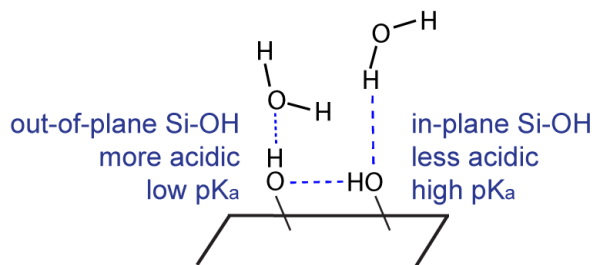
Figure 1.5 Schematic illustration of the hydrogen-bonding nature of two types of acidic sites at the silica/water interface. The out-of-plane silanol group at the left side that donates a hydrogen-bond to water is more acidic than the in-plane silanol group at the right side that accepts a hydrogen-bond from water. This figure is inspired by Ref [76].

Owing to their different pK_a values, at neutral pH the more acidic sites become ionized while the less acidic sites still remain protonated. Consequently, the surface charge density of silica directly depends on the relative population of these two silanol groups. From the discussion above it is implicit that the acidity of silanol sites is directly influenced by the strength of hydrogen bonds formed with water molecules. Therefore, it is possible that the presence of electrolytes at the aqueous phase of the interface affects the relative population of the two acidic sites by changing the water structure accordingly. We note that the previous SHG study that determined the bimodal distribution of acidic sites at the silica/water was performed in the presence of 0.5 M NaCl. According to this study, 19% of the silanol groups were ionized at neutral pH indicating that one-fifth of the total silanol groups were more acidic (Figure 1.6).
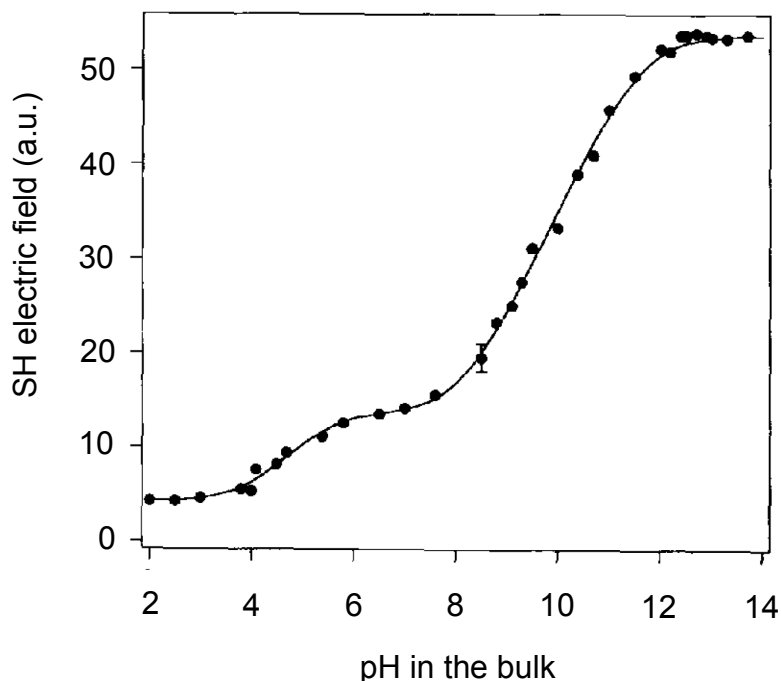
Figure 1.6 Plot of SH electric field as a function of pH in the bulk solution representing two acid-base equilibria of silica/water interface. The dots are experimental points, while the solid line is the theoretical fit with constant capacitance model. 19% of the surface silanol sites are more acidic with pK_{a1} = 4.5; and 81% are less acidic with pK_{a2} =8.5. The figure is adapted and modified from Ref[68], copyright 1992, with permission from Elsevier.

1.6 Functionalization of the Silica Surface

In addition to its environmental significance, insulating mineral oxides like silica are often used as the support material for many monofunctional and multifunctional surfaces that have applications in various areas such as sensing, molecular recognition,[78] chromatography, and catalysis.[79,80] By introducing organic moieties onto a silica surface one can tailor the organic functionalities in a defined and controlled way toward a particular application. Although the organic monolayers are extremely thin with only a few angstroms to nanometers thickness, they are able to completely change the surface properties of silica. The

role of the silica substrate in these functional materials is to make the organic functional groups more accessible and to provide mechanical stability of the hybrid materials.[81] The organic monolayers are typically synthesized using the chemisorption method where the surface-reactive organosilane molecules from solution are allowed to spontaneously self-assemble on the silica surface (Figure 1.7).

Self-assembled monolayers (SAMs) are well-defined and highly ordered two-dimensional array of organic molecules immobilized on a variety of surfaces including silica. Although there has been a long debate about the formation mechanism of SAMs on silica, it is established that the covalent nature of the assembly process results in high stability of the monolayers on the surface.[82] This stability allows further chemical derivatization of the surface groups without deterioration of the monolayers as shown in Figure 1.7. The chemical modification of the SAMs allows immobilization of new functional groups, catalysts, and biomolecules that can not be attached to the silica surface directly via simple silane chemistry.
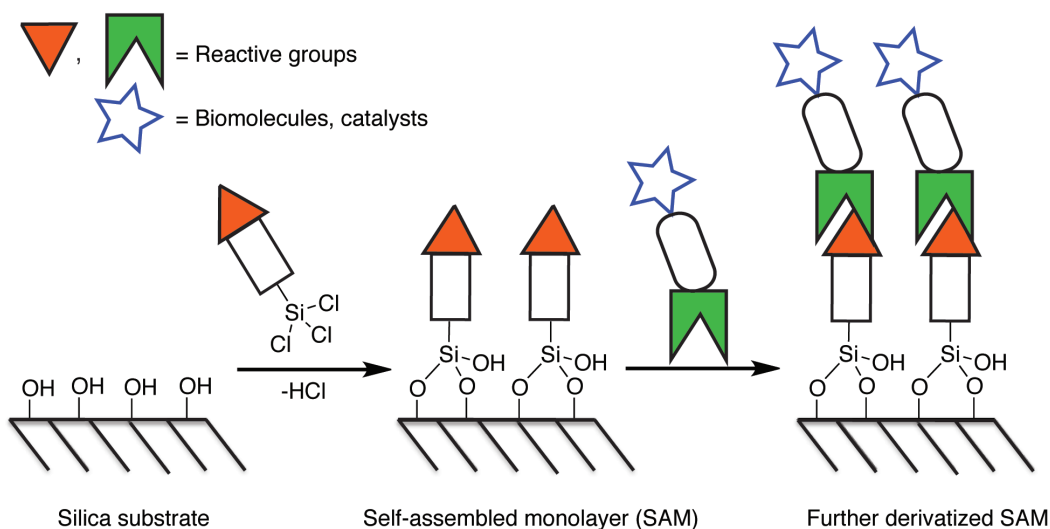
Figure 1.7 Schematic representation of self-assembly of an organotrichlorosilane on silica surface to form a well-defined SAM. Further chemical modification of the SAM yields a uniform layer of a new set of functional groups that could be either biomolecules or catalysts.

1.7 Methods for Studying the Functionalized Silica Surface

1.7.1 Methods for Characterizing the Surface

The development of analytical methods has been remarkable in the last couple of decades for the study of functionalized silica surfaces. The common methods that are used to characterize the properties of SAMs are discussed briefly in this section. Measuring the contact angle between a water droplet and the functionalized surface is a very intuitive and easy way to understand the wettability of the surfaces. It has been adopted widely in surface science research to obtain information on hydrophobicity or polarity, roughness and order of the SAMs.[83] Ellipsometry is another common surface characterization technique that is used for determining thickness of organic films that are thinner

than the wavelength of the probing light itself.[83] To measure the surface morphology, surface roughness, and molecular scale lattices atomic force microscopy (AFM) has been employed very commonly. AFM provides surface information by measuring the repulsive and attractive forces between a very sharp AFM tip (with 10-100 nm radius) and the sample surface.[84] In contrast, detailed quantitative information on the elemental composition, chemical state, and valence state of the elements that exist within the SAM can be obtained by X-ray photoelectron spectroscopy (XPS).[85,86] XPS is a surface specific chemical analysis technique that probes the kinetic energy and number of electrons that escape form the top 1 to 10 nm of the surface when irradiated with a beam of X-rays, which can be related to the above parameters and the relative amount of each element in the monolayer, respectively. The detection limits of XPS for most of the elements are usually in the range of parts per thousand, so it provides a good reliability about the measured elemental composition of the surface. An alternative technique to determine the elemental composition of SAMs is secondary ion mass spectrometry (SIMS), which is the mass spectrometry of ionized particles emitted by a solid surface upon bombardment by high-energy primary particles or ions.[87] Fourier transform infrared (FTIR) spectroscopy is also often employed to characterize the functional groups in SAMs. This spectroscopy is sensitive to the molecular packing and orientation of the molecules on the surface.[88] Fluorescence confocal microscopy is another technique frequently used to visualize the desired organic molecules or unique surface features of SAMs. The sample of interest is tagged through post monolayer formation modification with a fluorescent dye and

then the dye is excited with light of a particular wavelength so that the dye emits light of another wavelength.[89] The image of the dye on the surface is then generated from the emission data. While each of these techniques discussed here provides information highlighting a specific feature of the SAMs, a complete picture of the thin films can only be obtained by combining several techniques.

1.7.2 Methods for Monitoring Binding at the Interface

Total internal reflection fluorescence (TIRF) spectroscopy has been extensively used to monitor the binding behavior of various biological molecules at the interfaces. Specifically, TIRF has been successfully applied to study protein adsorption, antibody-antigen interaction and cell adhesion to surfaces because of the surface selectivity of this technique.[90,91] The surface selectivity in TIRF is attained by detecting the fluorescent molecules that are excited by the evanescent wave, which decays exponentially within approximately 100 nm pathlength from the surface. Attenuated total reflectance Fourier transform infrared (ATR-FTIR) spectroscopy is another surface selective analytical technique that detects only the molecules in the region of evanescent wave penetration depth. Like TIRF, this spectroscopy is also commonly used for studying the molecular interaction by monitoring the vibrational signatures of the molecules at the interface.[88,92,93] However, both of these techniques largely depend on the fact that all the detectable molecules in the evanescent wave region are adsorbed on to the surface, while being unable to distinguish the bound species and the species in solution. The interface specificity of the SHG and SFG spectroscopic techniques

arises from the presence of the noncentrosymmetry at the interface, which makes the techniques able to monitor only the bound species that cause noncentrosymmetry on the surface.

1.8 NLO Spectroscopies for Monitoring Binding at the Interface

Nonlinear optical spectroscopies such as SHG and sum frequency generation (SFG), with both interface specificity and molecular specificity, provide one with the capability of monitoring molecular recognition processes at the interface in real time. Therefore, in the past few years SHG and SFG have attracted much attention from scientists as tools to study surface reactions,[94-96] molecular binding behavior of surface species,[55] and DNA hybridization[97] at the interface. SHG can also be employed to measure the acid-base behavior of a carboxylic acid functionalized silica/water interface using the $\chi^{(3)}$ technique.[98,99] In this thesis, we utilized the resonantly enhanced SHG to study the molecular recognition processes of DNA immobilized at the silica/water interface.

1.8.1 Theoretical Background for the Resonantly Enhanced SHG

Resonantly enhanced SHG has been successfully applied to studying numerous systems in which the species of interest possess accessible electronic transitions to function as frequency dependent markers for their presence at the interface.[38,47,50,100] By selecting the incident frequency (ω) such that the second harmonic response (*2ω*) is in resonance with an electronic transition of a surface species, the second order nonlinear susceptibility can be described by a resonant

($\chi_R^{(2)}$) and a nonresonant ($\chi_{NR}^{(2)}$) contribution. Equation 1.1 then can be rewritten as follows:

$$\sqrt{I_{2\omega}} = E_{2\omega} \propto \sqrt{\left| \chi^{(2)} \right|^2} = \sqrt{\left| \chi_R^{(2)} + \chi_{NR}^{(2)} e^{i\Delta\phi} \right|^2} \qquad (1.7)$$

In this equation, the SHG E-field is proportional to the square modulus of the nonlinear susceptibility comprised of the resonant and nonresonant components, where the factor $\Delta\phi$ compensates for the phase difference between these two $\chi^{(2)}$ terms. For resonantly enhanced SHG studies, the phase difference between the resonant and nonresonant contributions has been experimentally determined to be 90°, thus eliminating cross terms from the square modulus.[101,102] This experimental measurement of the phase difference of 90° allows one to separate the resonant contribution from the SHG signal by simply following the equation,

$$\chi_R^{(2)} = \sqrt{I_{2\omega} - I_{NR}} \qquad (1.8)$$

where I_{NR} is the SHG signal intensity in absence of any SHG active molecules (*i.e.*, molecules in resonance with 2ω) at the interface. For the case of resonantly enhanced SHG studies at the silica/water interface, the SHG signal is dominated by the resonant susceptibility term ($\chi_R^{(2)}$), whereas the nonresonant contribution ($\chi_{NR}^{(2)}$) is weak and assumed to undergo negligible changes throughout the experiments. The resonant contribution to the nonlinear susceptibility ($\chi_R^{(2)}$) is described as the product of the number density (*N*) of molecules in resonance and the orientational average of their corresponding hyperpolarizability tensor $\beta^{(2)}$.[45, 48]

$$\chi_R^{(2)} = N \left\langle \beta^{(2)} \right\rangle . \qquad (1.9)$$

Since the $\chi_R^{(2)}$ linearly depends on the orientational average of the molecular hyperpolarizability, any molecules that are not oriented at the interface within the electric dipole approximation will not contribute to $\chi_R^{(2)}$. Consequently, $\chi_R^{(2)}$ will remain unaffected by any isotropically distributed SHG active molecules even if they are present within the evanescent field generated by the incident laser field, E_ω. This is how resonant SHG technique becomes capable of distinguishing the bound (oriented) and unbound (unoriented) species within the evanescent field that makes them superior from other surface specific techniques such as TIRF and ATR-FTIR.

To understand the resonance enhancement of the molecular hyperpolarizability, $\beta^{(2)}$ term is expressed as a summation over the electronic states, as represented in the following equation,[45,48]

$$\left\langle \beta^{(2)} \right\rangle = \frac{-4\pi^2 e^3}{h^2} \sum_{b,c} \frac{\left\langle a \left| \vec{\mu}_i \right| b \right\rangle \left\langle b \left| \vec{\mu}_j \right| c \right\rangle \left\langle c \left| \vec{\mu}_k \right| a \right\rangle}{(\omega - \omega_{ba} + i\Gamma_{ba})(2\omega - \omega_{ca} + i\Gamma_{ca})} . \qquad (1.10)$$

Here a, b and c represent the ground, intermediate, and excited electronic states, respectively, as shown in Figure 1.8, ω_{ba} and ω_{ca} are the frequencies of the corresponding electronic transitions, μ is the electric dipole moment operator, Γ_{ba} and Γ_{ca} are the damping coefficients for the corresponding transitions, h is Planck's constant, and e is the elementary charge. When the incident frequency, ω, and/or the SHG frequency, 2ω, matches an electronic transition within the surface species of interest, the molecular hyperpolarizability, $\beta^{(2)}$, is increased. An increase in $\beta^{(2)}$ results in an increase in $\chi_R^{(2)}$, that leads to an enhancement of the SHG signal response as seen in equation 1.7. Since the resonant enhancement of

26

the SHG signal depends on the number density of the resonant molecules (equation 1.9), association and dissociation behavior of these molecules at the interface can be readily quantified by measuring the SHG signal.
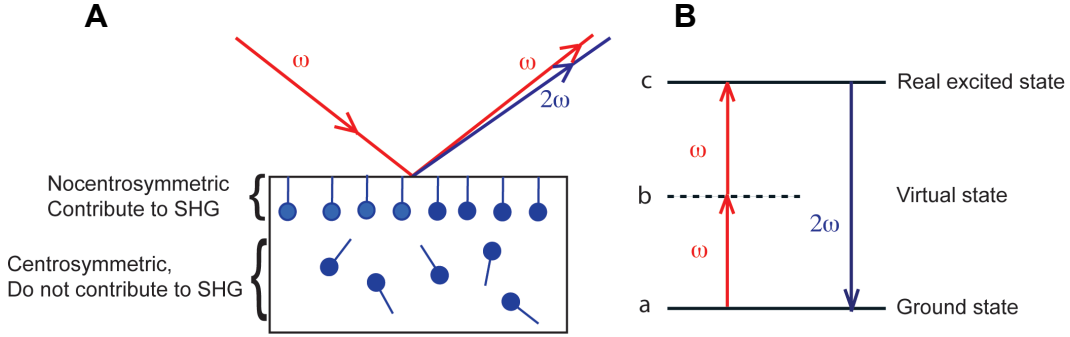
Figure 1.8 A) Geometry of the resonant SHG process. B) Energy-level diagram describing the resonantly enhanced SHG process. The SHG frequency, 2ω, is in resonance with the electronic transition frequency, ω_{ca}, of a surface species of interest.

1.8.2 Theoretical Background for Vibrational SFG

SFG is another surface specific NLO spectroscopy that has been used to study the vibrational signature of various species ranging from water to biomolecules at the interface.[38,103-106] In the case of SFG there are two incident light fields at the interface, one infrared (IR) light centered at ω_{IR} and the other visible light at ω_{Vis} as shown in Figure 1.9. The sum-frequency light field generated at $\omega_{IR} + \omega_{Vis}$ arises from the oscillating polarization $P^{(2)}_{\omega_{IR}+\omega_{Vis}}$.

$$\sqrt{I_{SFG}} = E_{SFG} \propto P^{(2)}_{\omega_{IR}+\omega_{Vis}} = \chi^{(2)}_{\omega_{IR}+\omega_{Vis}} E_{\omega_{IR}} E_{\omega_{Vis}} \qquad (1.11)$$

where $E_{\omega_{IR}}$ and $E_{\omega_{Vis}}$ are the incident light fields for the IR and visible light, respectively, and $\chi^{(2)}_{\omega_{IR}+\omega_{Vis}}$ is the second-order nonlinear susceptibility. Like

resonant SHG, the SFG signal intensity depends on this $\chi^{(2)}_{\omega_{IR}+\omega_{Vis}}$, which in turn

depends on the molecular hyperpolarizability, $\beta^{(2)}$. By tuning the incident IR

frequency such that it is in resonance with the vibrational frequency of a molecule

at the interface one can obtain resonantly enhanced $\beta^{(2)}$, which leads to an

increased SFG signal.
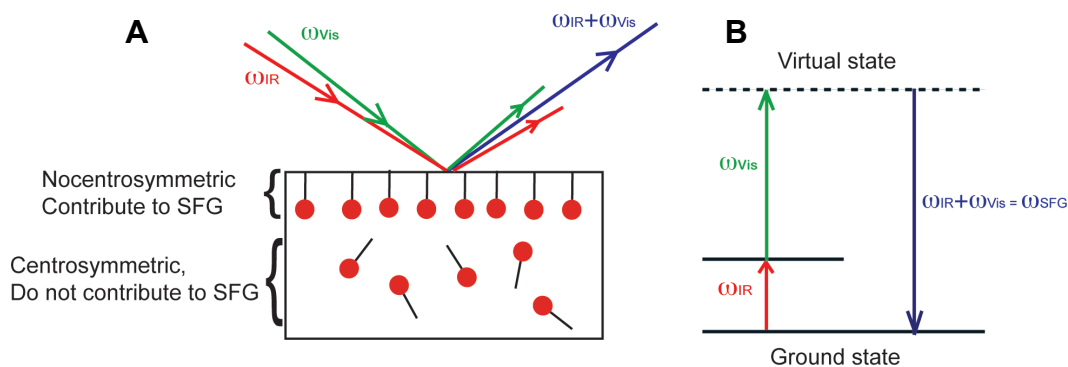
Figure 1.9 A) Geometry of the vibrational SFG process. B) Energy-level diagram describing the resonance enhancement of the SFG process. The IR frequency, ω_{IR}, is in resonance with a vibrational transition frequency of a surface species of interest.

1.9 Thesis Goals and Organization

The goal of this thesis is to obtain quantitative molecular-level insight into

processes that are important in many environmental, industrial and

biotechnological applications. By taking advantage of the surface-specificity of

nonlinear optical spectroscopic techniques we address some fundamental

questions about ion specific effects on the surface charge density of silica over a

broad range of pH. To explore more structurally complex interfaces, our

combined synthetic and spectroscopic approach allows us to attach a functional

group to the silica surface by performing silane chemistry. This functional group can then be further derivatized to generate a surface containing new molecular recognition sites at the interface such as DNA. We characterize the surface synthesis by employing SFG, XPS, AFM, and contact angle measurements. While, to monitor molecular processes in real time, such as association and thermal dissociation of immobilized DNA at the interface, we employed on-resonance SHG spectroscopy. To develop strategies to look at more multifunctional interfaces in the future, we also developed a well-defined mixed monolayer that can be used as a common starting point for making bifunctional monolayers of different composition. The thesis projects described in the subsequent chapters are outlined as follows:

Chapter 2 describes the investigation of specific cation effects on the acid-base behavior of the silica/water interface using nonresonant SHG spectroscopy. We systematically vary the alkali ions in the aqueous phase and monitored the change in surface charge density, which represents the deprotonation state of the surface sites on silica, over a broad pH range. The effective equilibrium constants and the relative population of the two acidic sites described in Section 1.4 are measured from the titration curves in the presence of each alkali ion. The effects of concentration of these alkali ions on the bimodal acid-base behavior of silica/water interface are also discussed in this chapter and a model is proposed to explain the experimental results.

The changes in the bimodal acid-base behavior of the planar silica/water interface are attributed to the influence of the specific ions on the interfacial water

structure and its corresponding effect on surface acidity. Since the halide ions are renowned to show more significant specific ion effects on the interfacial hydrogen-bonded structure of water at other interfaces, our next interest was to explore the effects of halide ions on the acid-base chemistry of the silica/water interface. Chapter 3 demonstrates the utility of SHG and SFG to monitor the influence of sodium and potassium halides on acid-base processes at the negatively charged silica/aqueous electrolyte interface. We measured the sensitivity of the two types of acidic silanols at the surface to the presence of halides in the aqueous phase and a simple cooperative model is employed to explain this sensitivity.

In the subsequent project we utilized planar silica, which is optically transparent permitting spectroscopic characterization of the interface, as the substrate for studying the behavior of immobilized DNA. Chapter 4 describes our synthetic and characterization strategy of immobilizing DNA onto glass support. Using XPS we measure the surface coverage of DNA while resonantly enhanced SHG spectroscopy was used to monitor the association and thermal dissociation of DNA immobilized at the silica/water interface. Specifically, we monitored the hybridization rate and thermal dissociation of DNA immobilized at the silica/aqueous interface utilizing a solution phase complementary DNA strand functionalized with an SHG-active label. The thermal dissociation temperature and thermodynamic changes of the DNA immobilized on silica were also determined and compared with the analogous duplex in solution.

Future work in our group will be aimed at monitoring processes at more

complex biomimetic and catalytic interfaces. Consequently, our final goal was to develop a general strategy for generating bifunctional surfaces where the ratio of each function was well defined. Chapter 5 of this thesis discusses our strategy to synthesize bifunctional surface by exploiting the concept of orthogonal reactivity. This chapter reports the synthesis and self-assembly of azide and amine trimethoxysilanes that result in mixed monolayers on silica. The amine and azide functional groups can be independently reacted with acid chlorides and terminal alkynes, respectively, to generate bifunctional surfaces. Using XPS, we determine the azide/amine surface ratio as well as the reactivity of the azide and amine functional groups in the mixed SAM. AFM, FTIR and contact angle measurements were also employed to characterize the surface.

The general conclusions regarding the results of all the research projects are summarized in the final chapter of this thesis.

1.10 References

(1)   Sposito, G. *The Surface Chemistry of Soils*; Oxford University Press, **1984**.

(2)   Erbil, H. Y. *Surface Chemistry of Solid and Liquid Interfaces*; 1st ed.; Blackwell Publishing Ltd., Oxford, **2006**.

(3)   Shen, Y. R.; Ostroverkhov, V. *Chem. Rev.* **2006**, *106*, 1140.

(4)   Nihonyanagi, S.; Yamaguchi, S.; Tahara, T. *J. Chem. Phys.* **2009**, *130*, 204704.

(5)   Hsu, P. Y.; Dhinojwala, A. *Langmuir* **2011**, *28*, 2567.

(6)   Jena, K. C.; Covert, P. A.; Hore, D. K. *J. Phys. Chem. Lett.* **2011**, *2*, 1056.

(7)   Carrasco, J.; Hodgson, A.; Michaelides, A. *Nat Mater* **2012**, *11*, 667.

(8)   Stumm, W.; Morgan, J. J. *Aquatic Chemistry: Chemical Equilibria and Rates in Natural Waters; Third Edition*; Wiley, **1995**.

(9)   Iler, R. K. *Chemistry of Silica - Solubility, Polymerization, Colloid and Surface Properties and Biochemistry*; John Wiley & Sons, **1979**.

(10)   Kallury, K. M. R.; Macdonald, P. M.; Thompson, M. *Langmuir* **1994**, *10*, 492.

(11)   Sindorf, D. W.; Maciel, G. E. *J. Am. Chem. Soc.* **1983**, *105*, 1487.

(12)   Leonardelli, S.; Facchini, L.; Fretigny, C.; Tougne, P.; Legrand, A. P. *J. Am. Chem. Soc.* **1992**, *114*, 6412.

(13)   Tuel, A.; Hommel, H.; Legrand, A. P.; Kovats, E. S. *Langmuir* **1990**, *6*, 770.

(14)   Maciel, G. E.; Sindorf, D. W. *J. Am. Chem. Soc.* **1980**, *102*, 7606.

(15)   Yang, Z.; Li, Q.; Chou, K. C. *J. Phys. Chem. C* **2009**, *113*, 8201.

(16)   Sonnefeld, J. *Colloid Polymer Sci.* **1995**, *273*, 932.

(17)   Mondragon, M. A.; Castano, V. M.; M., J. G.; S., C. A. T. *Vib. Spectrosc.* **1995**, *9*, 293.

(18)   Franks, G. V. *J. Coll. Interf. Sci.* **2002**, *249*, 44.

(19)   Van Cappellen, P.; Qiu, L. *Deep-Sea Res. Pt II* **1997**, *44*, 1129.

(20)   Corma, A.; Garcia, H. *Adv. Synth. Catal.* **2006**, *348*, 1391.

(21)   Schena, M.; Shalon, D.; Davis, R. W.; Brown, P. O. *Science* **1995**, *270*, 467.

(22)   Heise, C.; Bier, F. F. *Top. Curr. Chem.* **2006**, *261*, 1.

(23)   Morrow, B. A.; Gay, I. D. *J. Phys. Chem.* **1988**, *92*, 5569.

(24)   Bergna, H. E.; Roberts, W. O. *Colloidal Silica: Fundamentals and Applications*; Taylor & Francis, **2005**.

(25)   Zhdanov, S. P.; Kosheleva, L. S.; Titova, T. I. *Langmuir* **1987**, *3*, 960.

(26)   Morrow, B. A.; Cody, I. A. *J. Phys. Chem.* **1976**, *80*, 1995.

(27)   Dove, P. M.; Craven, C. M. *Geochim. Cosmochim. Acta* **2005**, *69*, 4963.

(28)   Karlsson, M.; Craven, C.; Dove, P. M.; Casey, W. H. *Aquat. Geochem.* **2001**, *7*, 13.

(29)   Milonjic, S. K. *Coll. Surf.* **1987**, *23*, 301.

(30)   Salis, A.; Parsons, D. F.; Bostrom, M.; Medda, L.; Barse, B.; Ninham, B. W.; Monduzzi, M. *Langmuir* **2010**, *26*, 2484.

(31)   Kobayashi, M.; Juillerat, F.; Galletto, P.; Bowen, P.; Borkovec, M. *Langmuir* **2005**, *21*, 5761.

(32)   Campen, R. K.; Pymer, A. K.; Nihonyanagi, S.; Borguet, E. *J. Phys. Chem. C* **2010**, *114*, 8465.

(33)   Shaw, A. M.; Hannon, T. E.; Li, F.; Zare, R. N. *J. Phys. Chem. B* **2003**, *107*, 7070.

(34)   Fisk, J. D.; Batten, R.; Jones, G.; O'Reill, J. P.; Shaw, A. M. *J. Phys. Chem. B* **2005**, *109*, 14475.

(35)   O'Reilly, J. P.; Butts, C. P.; I'Anson, I. A.; Shaw, A. M. *J. Am. Chem. Soc.* **2005**, *127*, 1632.

(36)   Petersen, P. B.; Saykally, R. J. *J. Phys. Chem. B* **2006**, *110*, 15037.

(37)   Fisk, J. D.; O'Reilly, J. P.; Shaw, A. M. *J. Phys. Chem. B* **2006**, *110*, 15039.

(38)   Eisenthal, K. B. *Chem. Rev.* **1996**, *96*, 1343.

(39)   Zhao, X.; Ong, S.; Wang, H.; Eisenthal, K. B. *Chem. Phys. Lett.* **1993**, *214*, 203.

(40)   Yan, E. C. Y.; Liu, Y.; Eisenthal, K. B. *J. Phys. Chem. B* **1998**, *102*, 6331.

(41)   Corn, R. M.; Higgins, D. A. *Chem. Rev.* **1994**, *94*, 107.

(42)   Gopalakrishnan, S.; Liu, D.; Allen, H. C.; Kuo, M.; Shultz, M. J. *Chem. Rev.* **2006**, *106*, 1155.

(43)   Schr¨odle, S.; Richmond, G. L. *J. Phys. D: Appl. Phys.* **2008**, *41*.

(44)   Verreault, D.; Hua, W.; Allen, H. C. *J. Phys. Chem. Lett.* **2012**, *3*, 3012.

(45)   Boyd, R. W. *Nonlinear Optics, Third Edition*; Academic Press, **2008**.

(46)   Eisenthal, K. B. *Acc. Chem. Res.* **1993**, *26*, 636.

(47)   Eisenthal, K. B. *Chem. Rev.* **2006**, *106*, 1462.

(48)   Shen, Y. R. *The Principles of Nonlinear Optics*; John Wiley & Sons: New York, **1984**.

(49)   Salafsky, J. S.; Eisenthal, K. B. *J. Phys. Chem. B* **2000**, *104*, 7752.

(50)   Al-Abadleh, H. A.; Mifflin, A. L.; Bertin, P. A.; Nguyen, S. T.; Geiger, F. M. *J. Phys. Chem. B* **2005**, *109*, 9691.

(51)   Jordan, D. S.; Malin, J. N.; Geiger, F. M. *Environ. Sci. Technol.* **2010**, *44*, 5862.

(52)   Beildeck, C. L.; Liu, M. J.; Brindza, M. R.; Walker, R. A. *J. Phys. Chem. B* **2005**, *109*, 14604.

(53)   Beildeck, C. L.; Steel, W. H.; Walker, R. A. *Faraday Discuss.* **2005**, *129*.

(54)   Shang, X. M.; Benderskii, A. V.; Eisenthal, K. B. *J. Phys. Chem. B* **2001**, *105*, 11578.

(55)   Konek, C. T.; Illg, K. D.; Al-Abadleh, H. A.; Voges, A. B.; Yin, G.; Musorrafiti, M. J.; Schmidt, C. M.; Geiger, F. M. *J. Am. Chem. Soc.* **2005**, *127*, 15771.

(56)   Hayes, K. F.; Redden, G.; Ela, W.; Leckie, J. O. *J. Colloid Interf. Sci.* **1991**, *142*, 448.

(57)   Davis, J. A.; Kent, D. B. *Rev. Mineral.* **1990**, *23*, 177.

(58)   Hayes, K. F.; Papelis, C.; Leckie, J. O. *J. Colloid Interf. Sci.* **1988**, *125*, 717.

(59)   Dzombak, D. A.; Morel, M. M. *Surface Complexation Modeling*; Wiley: New York, **1990**.

(60)   Bockris, J. O.; Reddy, A. K. N. *Modern Electrochemistry*; Plenum Press: New York, **1970**.

(61)   Gragson, D. E. R., G. L. *J. Am. Chem. Soc.* **1998**, *120*, 366.

(62)   Morel, F. M. M. *Principles of Aquatic Chemistry*; John Wiley & Sons: New York, **1983**.

(63)   Riemsdijk, W. H. v.; Hiemstra, T. In *Interface Science and Technology*; Johannes, L., Ed.; Elsevier: **2006**; Vol. Volume 11, p 251.

(64)   Langmuir, D. *Aqueous Environmental Geochemistry*; Prentice Hall, **1997**.

(65)   Allen, L. H.; Matijevic, E. *J. Colloid Interf. Sci.* **1969**, *31*, 287.

(66)   Allen, L. H.; Matijevic, E. *J. Colloid Interf. Sci.* **1970**, *33*, 420.

(67)   Allen, L. H.; Matijevic, E.; Meites, L. *J. Inorg. Nucl. Chem.* **1971**, *33*, 1923.

(68)   Ong, S.; Zhao, X.; Eisenthal, K. B. *Chem. Phys. Lett.* **1992**, *191*, 327.

(69)   Azam, M. S.; Weeraman, C. N.; Gibbs-Davis, J. M. *J. Phys. Chem. Lett.* **2012**, 1269.

(70)   Du, Q.; Freysz, E.; Shen, Y. *Phys. Rev. Lett.* **1994**, *72*, 238.

(71)   Li, I.; Bandara, J.; Shultz, M. J. *Langmuir* **2004**, *20*, 10474.

(72)   Ostroverkhov, V.; Waychunas, G.; Shen, Y. *Phys. Rev. Lett.* **2005**, *94*.

(73)   Jena, K. C.; Hore, D. K. *J. Phys. Chem. C* **2009**, *113*, 15364.

(74)   Dong, Y.; Pappu, S. V.; Xu, Z. *Anal. Chem.* **1998**, *70*, 4730.

(75)   Leung, K.; Nielsen, I. M. B.; Criscenti, L. J. *J. Am. Chem. Soc.* **2009**, *131*, 18358.

(76)   Gaigeot, M.-P.; Sprik, M.; Sulpizi, M. *J. Phys.: Condens. Matter* **2012**, *24*, 124106.

(77)   Sulpizi, M.; Gaigeot, M.-P.; Sprik, M. *J. Chem. Theory Comput.* **2012**, *8*, 1037.

(78)   Kessler, D.; Nilles, K.; Theato, P. *J. Mater. Chem.* **2009**, *19*, 8184.

(79)   Huh, S.; Chen, H.-T.; Jerzy W. Wiench; Pruski, M.; Lin, V. S.-Y. *Angew. Chem., Int. Ed.* **2005**, *44*, 1826

(80)   Banet, P.; Marcotte, N.; Lerner, D. A.; Brunel, D. *Langmuir* **2008**, *24*, 9030.

(81)   Onclin, S.; Ravoo, B. J.; Reinhoudt, D. N. *Angew. Chem., Int. Ed.* **2005**, *44*, 6282

(82)   Ninham, B. W. *Molecular forces and self assembly : in colloid, nano sciences and biology / Barry W. Ninham and Pierandrea Lo Nostro*; Cambridge University Press: Cambridge, UK, **2010**.

(83)   Ulman, A. *An Introduction to Ultrathin Organic Films*; Academic Press: Boston, **1991**.

(84)   Morita, S.; Wiesendanger, R.; Meyer, E. *Nanocontact Atomic Force Microscopy*, 2002; Vol. XVII.

(85)   Watts, J. F.; Wolstenholme, J. *An Introduction to Surface Analysis by XPS and AES*; Wiley, Chichester, UK, **2005**.

(86)   Nefodov, V. I. *X-ray Photoelectron Spectroscopy of Solid Surfaces*; VSP, Utrecht, **1988**.

(87)   Vickerman, J. C. *Surface Analysis - The Principal Techniques*; Wiley, Chichester, **1997**.

(88)   Tolstoy, V. P.; Chernyshova, I.; Skryshevsky, V. A. *Handbook of Infrared Spectroscopy of Ultrathin Films*; Wiley, **2003**.

(89)   Pawley, J. B. *Handbook of Biological Confocal Microscopy*; Springer: New York, **2006**.

(90)   Andrade, J. D.; Hlady, V.; Wey, A.-P.; Ho, C.-H.; Lea, A. S.; Jeon, S. I.; Lin, Y. S.; Stroup, E. *Clinical Materials* **1992**, *11*, 67.

(91)   Brash, J. L.; Wojciechowski, P. W. *Interfacial phenomena and bioproducts*; Marcel Dekker: New York, **1996**.

(92)   Sukhishvili, S. A.; Kharlampieva, E.; Izumrudov, V. *Macromolecules* **2006**, *39*, 8873.

(93)   Bargar, J. R.; Reitmeyer, R.; Davis, J. A. *Env. Sci. Tech.* **1999**, *33*, 2481.

(94)   Stokes, G. Y.; Buchbinder, A. M.; Gibbs-Davis, J. M.; Scheidt, K. A.; Geiger, F. M. *J. Phys. Chem. A* **2008**, *112*, 11688.

(95)   Kutz, R. B.; Braunschweig, B. r.; Mukherjee, P.; Dlott, D. D.; Wieckowski, A. *J. Phys. Chem. Lett.* **2011**, *2*, 2236.

(96)   Kutz, R. B.; Braunschweig, B.; Mukherjee, P.; Behrens, R. L.; Dlott, D. D.; Wieckowski, A. *J. Catal.* **2011**, *278*, 181.

(97)   Boman, F. C.; Musorrafiti, M. J.; Gibbs, J. M.; Stepp, B. R.; Salazar, A. M.; Nguyen, S. T.; Geiger, F. M. *J. Am. Chem. Soc.* **2005**, *127*, 15368.

(98)   Konek, C. T.; Musorrafiti, M. J.; Al-Abadleh, H. A.; Bertin, P. A.; Nguyen, S. T.; Geiger, F. M. *J. Am. Chem. Soc.* **2004**, *126*, 11754.

(99)   Voges, A. B.; Al-Abadleh, H. A.; Musorrafiti, M. J.; Bertin, P. A.;

Nguyen, S. T.; Geiger, F. M. *J. Phys. Chem. B* **2004**, *108*, 18675.

(100)   Al-Abadleh, H. A.; Voges, A. B.; Bertin, P. A.; Nguyen; Geiger, F. M. *J.

Am. Chem. Soc.* **2004**, *126*, 11126.

(101)   Mifflin, A. L.; Musorrafiti, M. J.; Konek, C. T.; Geiger, F. M. *J. Phys.

Chem. B* **2005**, *109*, 24386.

(102)   Al-Abadleh, H. A.; Mifflin, A. L.; Musorrafiti, M. J.; Geiger, F. M. *J.

Phys. Chem. B* **2005**, *109*, 16852.

(103)   Richmond, G. L. *Chem. Rev.* **2002**, *102*, 2693.

(104)   Eftekhari-Bafrooei, A.; Borguet, E. *J. Phys. Chem. Lett.* **2011**, 1353.

(105)   Isaienko, O.; Nihonyanagi, S.; Sil, D.; Borguet, E. *J. Phys. Chem. Lett.*

2012, *4*, 531.

(106)   Mondal, J. A.; Nihonyanagi, S.; Yamaguchi, S.; Tahara, T. *J. Am. Chem.

Soc.* **2010**, *132*, 10656.

CHAPTER 2

Specific Cation Effects on the Acid-Base Behavior

of the Silica/Water Interface

Portions of this chapter are reproduced in part with
permission from the American Chemical Society

2.1 Introduction

Understanding the interactions of cations with mineral oxides is of central importance in predicting geochemical processes like deprotonation,[1] dissolution,[2] and adsorption.[3] Indeed, the accuracy of pollutant transport models depends on correctly identifying the influence of common spectator ions like sodium and potassium on geochemical systems involving mineral oxides.[4-8] In addition to the environmental significance, the behavior of insulating mineral oxides like silica is also pertinent to applications ranging from catalysis[9] to diagnostics[10,11] as such oxides are often used as the support material. In particular, the binding affinity of the mineral oxide interface for aqueous species is often influenced by the surface charge density as a result of electrostatic interactions.[4] Consequently, there has been a great deal of work aimed at quantifying the acid-base equilibria of silica, and a range of pK_a values has been reported that vary depending on silica morphology.[1,8,12-15] However, despite the large amount of attention, the influence of specific ions on the acid-base behavior of planar silica over a broad pH range has not been quantified, despite the fact that planar silica exhibits two distinct equilibria between pH 2 - pH 13.

Over the last decade interest in specific ion effects has often focused on the influence of ion polarizability on the interfacial structure of water at air/aqueous electrolyte and Langmuir-Blodgett interfaces.[7,16-22] More recent work has turned to identifying the water structure of the solid/liquid interface and the role of specific ions at mineral oxide surfaces.[23] For example, at the fused silica/water interface the extent of hydrogen-bonding and ordering of interfacial

water was found to depend on the polarizability of the alkali ion,[23] which had been observed at the air/water interface.[18] The properties of silica are also influenced by the presence of different specific ions. The nature of the alkali ion was found to influence the surface charge density[1,20] and zeta potential[24,25] of colloidal silica, indicating that the charge of mineral oxides cannot be predicted from pH alone. In the former example, Ninham and co-workers were able to predict the changes in surface charge density over a narrow pH range in the presence of $LiCl_{(aq)}$, $NaCl_{(aq)}$ or $KCl_{(aq)}$ by incorporating ion polarizability, hydration, and alkali-chloride ion-pair interactions into their silica surface model.[20] Nevertheless, a complete picture has yet to emerge regarding the effect of the electrolyte identity on the bimodal acid-base equilibria of the planar silica/water interface. Determining specific ion effects on the surface charge density and the corresponding acid-base equilibria over a broad pH is critical to understand and predict the behavior of silica under environmentally relevant conditions.[4] Moreover, the impact of specific cations on acid-base chemistry could prove general for other biological or material interfaces, where water-ion, water-surface and ion-surface interactions are thought to play major roles.[26]

Monitoring the acid-base behavior of insulating mineral oxides often relies on indirect measurements using pH-sensitive molecules with spectroscopic signatures[27-29] or potentiometric titration techniques that only operate over a limited pH range.[1] However, in 1992 Eisenthal and co-workers demonstrated that non-resonant second harmonic generation (SHG) spectroscopy provided a surface-sensitive and label-free method of monitoring the acid-base behavior of

silica.[30] Herein we apply SHG to identify the role of specific ions on the acid-base equilibria at the silica/water interface. Our results indicate that the nature of the alkali ion has a dramatic effect on the equilibrium behavior and silanol speciation at the silica/water interface.

2.2 Results and Discussion

2.2.1 Background Theory of Second Harmonic Generation

Second harmonic generation (SHG) was selected to probe the acid-base chemistry of the silica/water interface owing to its surface selectivity and sensitivity to interfacial charges. The reason that SHG is inherently surface specific in centrosymmetric materials like fused silica is because it requires a lack of inversion symmetry to occur.[13] At the fused silica-water interface where inversion symmetry is broken, the interaction of light of frequency ω will lead to an induced polarization with twice the incident frequency ($P_{2\omega}$). As a result of this induced polarization a new electric field is generated at 2ω, which emanates coherently from the interface ($E_{2\omega}$). The intensity of this response is a function of the second-order susceptibility, $\chi^{(2)}$, which is non-zero at the interface and depends on the composition and order of interfacial molecules.[13] Additionally, $E_{2\omega}$ is also modulated by the presence of a third static electric field arising from charge sites at the surface according to the third-order susceptibility, $\chi^{(3)}$.[30,31] Consequently, $E_{2\omega}$ can be expressed as:

$$E_{2\omega} \propto P_{2\omega} = \chi^{(2)} E_\omega E_\omega + \chi^{(3)} E_\omega E_\omega \Phi \qquad (2.1)$$

where Φ_0 is the interfacial potential that depends on this static electric field.[13] At high salt concentrations the change in interfacial potential varies linearly with surface charge density according to the constant capacitance model.[6] At the silica/water interface the interfacial potential is generally pH sensitive, as deprotonation of the surface above the point of zero charge (pzc ~ 2) occurs over a wide pH range. In contrast, $\chi^{(2)}$ and $\chi^{(3)}$ are considered to be much less sensitive to changes in pH.[13,32] Consequently, the change in $E_{2\omega}$ can be directly correlated with deprotonation of the interface.[8,13]
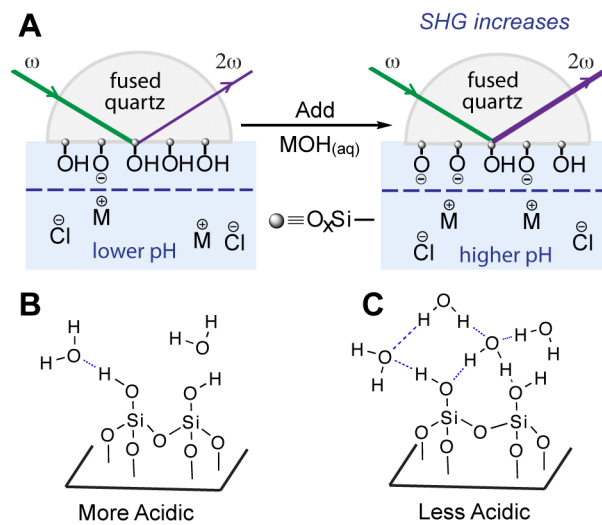
Figure 2.1 (A) Schematic illustrating how increasing the pH will deprotonate acidic sites causing an increase in the SHG intensity (proportional to $|E_{2\omega}|^2$). The 0-plane where the interfacial potential originates is depicted by the dashed line.[8] There are two types of acidic groups at the interface which are proposed to be (B) silanol groups associated with weakly hydrogen-bonded water resulting in a pK_a ~4-5 and (C) silanol groups associated with strongly hydrogen-bonded water resulting in a pK_a of ~9.

Figure 2.1 illustrates the origin of the expected increase in the SHG intensity as silica surface sites are deprotonated owing to the increase in

magnitude of the interfacial potential, even in the presence of screening electrolyte.[30] This planar silica/water interface has been shown by SHG and other methods to exhibit two distinct acidic sites.[26,27,29-31,33] One explanation for the two acidic sites attributes the more acidic site to silanols in contact with weakly hydrogen-bonded water (Figure 2.2B) and the less acidic site to silanols in contact with strongly hydrogen-bonded water (Figure 2.2C), which is supported by sum frequency generation experiments.[26,34] Other researchers have suggested that the more acidic site is silanolium (protonated silanol)[35] or silanols lacking hydrogen bonds.[27] However, recent ab initio molecular dynamics simulations lend support to the role of interfacial water finding that silanol groups on hydrophobically restructured quartz exhibit the lowest pK_a.[14] They also observed that the pK_a of silanols increased as the number of water layers increased.[14] Finally, the less acidic sites exhibit a $pK_a \sim 9$, which is similar to that of the monomeric form of silica, monosilicic acid (pK_a ($Si(OH)_4$) = 9.9),[12] which also supports that strong solvation decreases silanol acidity. Based on the apparent role of water on surface acidity, we expected that the perturbation of the water structure by the alkali ions would affect the corresponding acid-base equilibrium of the silica interface.

2.2.2 Specific Ion Effects on the Acid-Base Equilibria of the Silica/Water Interface

To determine the role of specific ions on the acid-base chemistry of planar silica, we performed multiple SHG titration experiments in the presence of 0.5 M alkali chloride. Representative acid-base titration curves are shown in Figure 2.2

and illustrate the pH dependence of the normalized SHG electric field, which is proportional to the fraction of deprotonated silanols at the interface. As expected, the silica/water interface exhibited two distinct acidic sites: one site that dissociated below pH 7 and the other that dissociated above pH 7 (Figure 2.2A and B, respectively). For the more acidic silanol groups deprotonated below pH 7, we observed slight differences in behavior for all of the silica/alkali chloride electrolyte interfaces (Figure 2.2A). However, at higher pH the titration profiles exhibited striking shifts in the inflection point, which revealed that the stability of these less acidic silanols depended strongly on the local electrolyte (Figure 2.2B). For example, in the presence of NaCl half of these less acidic silanol groups were deprotonated at pH 8.6(1). In contrast, the corresponding point in the titration curve occurred at pH 11.1(1) in the presence of CsCl, indicating that this interface was much less acidic.
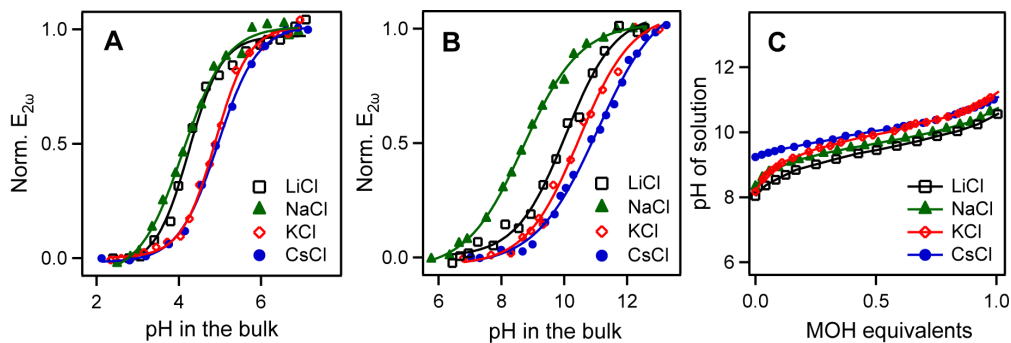
Figure 2.2 Representative titration curves of normalized $E_{2\omega}$ proportional to the fraction of deprotonated groups as a function of (A) low pH and (B) high pH for the silica/water interface in the presence of 0.5 M alkali chloride electrolyte. The solid lines represent the fit of a sigmoidal function to the data. (C) Representative titrations of pH versus aqueous alkali hydroxide (MOH) equivalents added to the corresponding alkali bicarbonate (initially at 0.1 M).

Although one cause of these specific ion effects involves altering the interfacial water structure and the corresponding surface acidity (vide supra),[14,26,30] we can also envision that the different cations stabilize the siloxide form of surface sites to varying extents thereby influencing silanol acidity. To quantify this effective pK$_a$ (pK_a^{eff}) we propose a simple model based on the affinity of the alkali ion for the siloxide sites that are generated after deprotonation. We first consider the acid dissociation of the surface silanol groups leading to the corresponding siloxide conjugate base:

$$SiOH + H_2O \xrightleftharpoons{Ka} SiO^- + H_3O^+ \qquad (2.2)$$
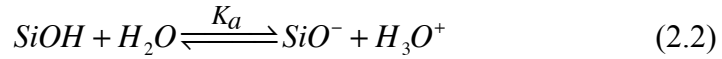
The cation, M$^+$ can then coordinate to the siloxide through electrostatic interactions.

$$SiO^- + M^+ \xrightleftharpoons{Kassc} SiO^- \cdot M^+ \qquad (2.3)$$
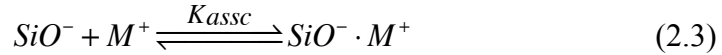
This electrostatic interaction does not neutralize the surface charge, which would lead to no change in the SHG signal, consequently it must be considered a screening interaction that is specific for the siloxide sites.[8] Finally, the overall equilibrium expression is:

$$K_a^{eff} = K_a K_{assc} = \frac{[SiO^- \cdot M^+][H_3O^+]}{[SiOH][M^+]} \qquad (2.4)$$

Owing to the relationship between E$_{2\omega}$ and the surface charge density, the pH where E$_{2\omega}$ is equal to 0.5 occurs when [SiO$^-$M$^+$]/[SiOH] for a given type of silanol is one.[30,31] The value of pK_a^{eff} can then be determined from this pH (pH$_{0.5}$) and the $-\log$[M$^+$], or pM$^+$ value, according to:

47

$$pK_a^{eff} = p(K_a K_{assc}) = pH_{0.5} - pM^+ .$$

<div style="text-align: right;">(2.5)</div>

It is important to note that this model does not implicitly include ion hydration or the presence of the chloride counterion, which could influence the surface behavior of the alkali ions.[3] Moreover it assumes that the surface alkali and hydronium concentrations depend similarly on their bulk concentrations such that the ratio of their surface concentrations and bulk concentrations are equal. Nevertheless, this simple model represents a good starting point for evaluating the influence of specific ions on the two acidic sites of silica based on the experimental relationship between $E_{2\omega}$ and bulk pH.

Table 2.1. Salt-dependent pK_a^{eff} Values of the Silica/Water Interface and Aqueous Bicarbonate. Values in bracket represent the standard deviations, for example, 4.1(2) means the average value is 4.1 with a standard deviation of 0.2.

Salt	pK_a^{eff} (low-pH)	pK_a^{eff} (high-pH)	pK_a^{eff} (MHCO$_3$)
LiCl	4.1(2)	9.6(2)	9.13(3)
NaCl	3.76(4)	8.3(1)	9.34(4)
KCl	4.6(2)	9.9(2)	9.62(2)
CsCl	4.5(2)	10.8(1)	9.73(2)

From the inflection point, pH$_{0.5}$ was determined and used to calculate pK_a^{eff} values for the various alkali chlorides and the more acidic and less acidic silanol groups (Table 2.1, *low pH* and *high pH*, respectively). There was not a large trend in the lower pH region for the more acidic silanol groups, but generally the K_a^{eff} values decreased with an increase in cation polarizability. The trend in K_a^{eff} values for the higher pH was more pronounced in the order: K_a^{eff}

(NaCl) > K_a^{eff} (LiCl) > K_a^{eff} (KCl) > K_a^{eff} (CsCl) with the relative position of LiCl

or NaCl leading to a deviation from the Hofmeister trend. Moreover, the pK_a^{eff}

values for these less acidic silanols differed by more than two log units, which

corresponds to significant differences in silanol stability.

From hard-soft acid-base theory[36] we would expect that smaller hard

cations should interact more strongly with the hard siloxide leading to a higher

K_a^{eff} and a lower pK_a^{eff}, which is indeed what we observed for both the low pH

and high pH equilibria. However, for both equilibria Na^+ rather than Li^+ exhibited

the strongest affinity for the siloxide surface. In addition to the hard-soft acid-base

model another model that is useful for explaining trends in binding behavior as a

function of ion polarizability is the Collins theory of matching water affinities,

which suggests that ions with similar water affinities can share their hydration

layer leading to ion-pair formation.[37] Based on the trend in our data, we reasoned

that Na^+ and SiO^- have more closely matched water affinities than Li^+ and SiO^-,

which leads to a stronger interaction between Na^+ and the surface. However, the

larger shifts in $pH_{0.5}$ that we observed for the higher pH region suggested that

other interactions besides those between the siloxide and cation were also critical

for these less acidic silanol groups. As previously discussed, these less acidic

silanol groups are thought to be stabilized in the neutral form by association with

strongly hydrogen-bonded water.[14,26,30] The presence of strongly hydrogen-

bonded water and consequently the stability of these silanol groups should be

perturbed based on the ability of the cation to disrupt the interfacial water

structure.[23] Thus, we propose the large range of $pH_{0.5}$ values for the less acidic

silanols stemmed from a combination of cation stabilization of the siloxide and perturbation of the interfacial water structure. To confirm that the interfacial structure was amplifying these specific ion effects, we compared these results with that of a solution-phase acid in the presence of 0.5 M alkali halide. For aqueous bicarbonate, which has a pK_a of 10.3,[38] we observed a trend in pK_a^{eff} following the Hofmeister series with Li^+ rather than Na^+ leading to the lowest pK_a^{eff}, yet the change in pK_a^{eff} was much less significant varying only by 0.6 log units (Figure 2C, Table 1). These results supported that interfaces can enhance specific ion effects, which is consistent with previous studies that concluded that specific ion effects are primarily interfacial effects.[16,39-42]

2.2.3 Specific Ion Effects on the Population of the Two Silanol Sites

Thus far we have considered the influence of the cation identity and concentration on the overall pK_a^{eff} values for the more acidic and less acidic silanol groups. The relative populations of these two types of silanol groups should also be ion specific, as the presence of each type of silanol is associated with different hydrogen-bonded structures of interfacial water (Figure 2.2B and C).[26] Owing to the ability of ions to disrupt the structure of interfacial water,[23] the relative amounts of the weakly and strongly hydrogen-bonded interfacial water should be very sensitive to the specific ion present, which in turn should influence the population distribution of the more and less acidic silanol groups. Recent SFG studies by Chou and co-workers have shown that the relative amount of strongly hydrogen-bonded, or high coordinate, water at the silica/alkali chloride

electrolyte interface varied with salt concentration and cation polarizability. At electrolyte concentrations less than 0.1 M, they found that lithium was more disruptive to the strongly hydrogen-bonded water than sodium, but potassium led to the most disruption.[23] The authors attributed this lack of trend to potassium's greater affinity for the silica surface at pH 7 (from potentiometric measurements performed on colloidal silica)[1] and the hydrated lithium's greater ability to perturb the interfacial water structure.[23] Based on these results and the previous SFG studies that correlated the extent of water hydrogen bonding with surface acidity,[26,34] we were interested to determine how the bimodal distribution of silanol groups varied with the hydrated ion radius. The relative amount of the acidic silanol groups is equivalent to the fraction deprotonated at pH 7, which can be determined from the relative change in $E_{2\omega}$ at low and high pH.[30,31]

Salt	f_{pH7}(%)
LiCl	60(3)
NaCl	20(2)
KCl	40(7)
CsCl	52(6)
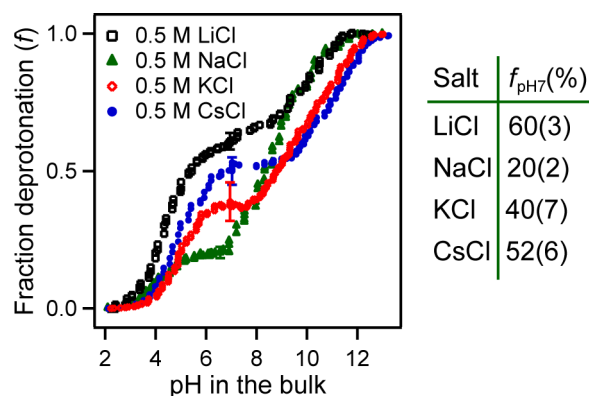
Figure 2.3 The fraction of deprotonated surface sites as a function of pH for the silica/electrolyte interface at 0.5 M salt concentration. Table: the percent deprotonated of the silica/electrolyte interface at pH 7.

As shown in Figure 2.3A, the fraction of more acidic silanol groups in presence of 0.5 M salts depended drastically on the identity of the alkali ion. As first reported by Eisenthal and co-workers, in the presence of 0.5 M NaCl the

51

number of silica sites deprotonated at pH 7 represents 19% of the acidic groups, which we also observed within error for this alkali halide (Figure 2.3, 20(2)%). For LiCl, however, the percentage of these sites increased to 60(3)%, with KCl and CsCl exhibiting intermittent percentages of 40(7), and 52(5)%, respectively. We observed that f decreases with a decrease in the hydrated cation radius:[43] $f_{pH7}(Li^+) > f_{pH7}(K^+) \cong f_{pH7}(Cs^+)$, with the exception of Na^+ (Figure 2.5). These results support that ions with larger hydration radii most disrupt the strongly hydrogen-bonded water leading to a larger fraction of acidic sites on the surface. The deviation of sodium from the trend, however, provided further support that sodium formed unique interactions with the surface that we once again attribute to ion pair formation rather than an outer sphere complex.[44] We reason that ion-pair formation allowed water to remain strongly hydrogen bonded at the interface in the presence of these high Na^+ concentrations. Although sodium is often considered to be hydrated at colloidal silica interfaces,[45] other surface complexation models suggest that sodium can form inner sphere complexes between neighboring silanol groups such that the ion is level with the surface silanol sites, which might explain the lack of disruption of strongly hydrogen-bonded water molecules for this cation.[12]

2.2.4 Effects of Decreasing the Salt Concentration on the Acid-Base Equilibria of the Silica/Water Interface

According to the proposed coupled equilibria, increasing the cation concentration should stabilize the siloxide form shifting the equilibrium to the

right leading to a more acidic surface. Conversely, decreasing the cation concentration should shift the equilibrium to the left, resulting in a less acidic surface. To test whether the presence of the cation stabilized the less acidic siloxide sites, which are the most sensitive to the cation, we decreased the concentration of the cation to 0.1 M for NaCl and monitored the resulting acid-base behavior (Figure 2.4B). As expected, decreasing the Na^+ cation concentration indeed led to an increase in the pH at which $E_{2\omega}$ equaled 0.5. Using the $pH_{0.5}$ values of 9.6(1) and 8.6(1) for 0.1 and 0.5 M NaCl concentrations and the corresponding p[Na^+] values in equation 2.7 yielded pK_a^{eff} values of 8.6(1) and 8.3(1), respectively (Table 2.2). The decent agreement for the two pK_a^{eff} values suggests that our simple model whereby sodium stabilizes the siloxide provides a reasonable interpretation of its influence on the surface equilibria. Very similar salt-dependent behavior was also observed for the nanoporous silica/NaCl electrolyte interface in a recent SHG experiment by Borguet and co-workers indicating this is general for different silica morphologies.[8]
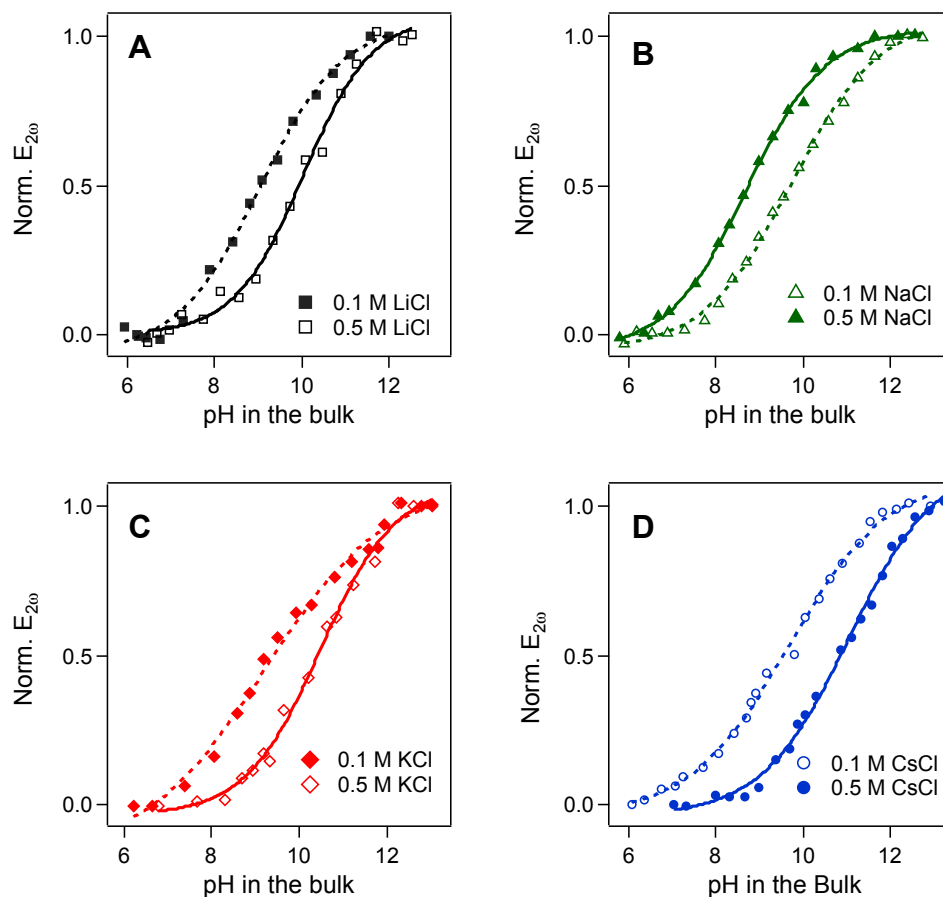
Figure 2.4 Representative plots of normalized $E_{2\omega}$ as a function of pH for the silica/electrolyte interface with aqueous (A) LiCl, (B) NaCl, (C) KCl and (D) CsCl at 0.1 M and 0.5 M concentrations. The solid lines (for 0.5 M) and dashed lines (for 0.1 M) represent the fit of a sigmoidal function to the data. The trend in salt concentration for $E_{2\omega}$ as a function of pH is opposite for the NaCl and other alkali chloride salts.

Repeating the concentration variation measurement for the other cations led to very different results. Specifically, decreasing the salt concentration of Li^+, K^+, and Cs^+ led to a *decrease* in the pH at which half the less acidic surface sites were deprotonated contrary to equation 2.7 (Figure 2.4A, C, D). These results suggested that the presence of alkali chlorides other than sodium chloride actually

54

stabilized the protonated rather than the siloxide form of these less acidic silanol groups, thereby requiring more basic environments to achieve deprotonation. To rationalize the observed concentration-dependent behavior for these salts, we neglect association of the cation to the siloxide and instead consider that the first step is cation dissociation from the silanol,

$$SiOH \cdot M^+ \underset{}{\overset{K_d}{\rightleftharpoons}} SiOH + M^+, \tag{2.6}$$
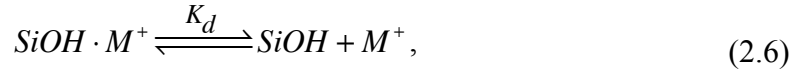
which results in the following overall equilibrium expression.

$$SiOH \cdot M^+ + H_2O \underset{}{\overset{K_d K_a}{\rightleftharpoons}} SiO^- + M^+ + H_3O^+. \tag{2.7}$$
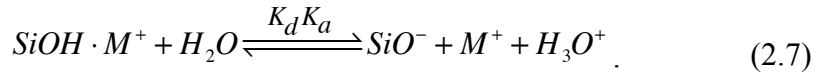
When half of the surface sites are deprotonated the salt-dependent equilibrium equation that results is:

$$K_a^{'eff} = K_d K_a = \frac{[SiO^-][M^+][H_3O^+]}{[SiOH \cdot M^+]} = [M^+][H_3O^+] \tag{2.8}$$

or

$$pK_a^{'eff} = p(K_d K_a) = pH_{0.5} + pM^+. \tag{2.9}$$

According to this revised mechanism for the lithium, potassium, and cesium salts the pH at which half the surface is deprotonated should decrease with decreasing salt concentration (corresponding to an increase in pM^+), which was observed in our experiment (Figure 2.4A, C, D). Specifically the $pH_{0.5}$ value decreased to 8.9(1) from 9.9(2) for LiCl, to 9.9(3) from 10.2(2) for KCl, to 9.5(2) from 11.1(1) for CsCl, when the salt concentration was decreased to 0.1 M from 0.5 M. From these titration results and the corresponding salt concentrations, we measured pK_a^{eff}' values of 9.9(2) and 10.2(1) for the silica/LiCl$_{aq}$, 9.9(3) and

10.5(1) for the silica/KCl$_{aq}$, and 10.5(2) and 11.4(1) for the silica/CsCl$_{aq}$ electrolyte interfaces at 0.1 M and 0.5 M salt, respectively using equation 2.9 (Table 2.2). We observed that the differences between the calculated values of $pK_a^{eff}{}'$ for these two salt concentrations increase (LiCl < KCl < CsCl) with the increase of cation size or polarizability suggesting that other equilibria besides those considered in equation 2.9 contributed to the salt-dependent behavior for KCl and CsCl. Nevertheless, the trend in salt concentration suggests that all alkali ions but Na$^+$ inhibited deprotonation, effectively stabilizing the less charged form of the surface. It is important to note that the surface at pH 7 that is stabilized in the presence of Li$^+$, K$^+$, and Cs$^+$ was still negatively charged, so electrostatic interactions with these cations and the surface were possible at this pH although they are expected to increase at higher pH. The trend of the pH$_{0.5}$ values at 0.1 M concentration was yet again in the order: pH$_{0.5}$(LiCl) $\cong$ pH$_{0.5}$(KCl) < pH$_{0.5}$(CsCl) with the exception of NaCl that yielded a pH$_{0.5}$ equaled to 9.6(1). However, all the pH$_{0.5}$ values at 0.1 M concentration were very close compared to the pH$_{0.5}$ values at 0.5 M salt concentration. This observation also indicates that at higher concentration the specific cation effect is more substantial than that at low concentration.

Table 2.2. Thermodynamic Parameters from the Salt Concentration Variation Experiments.[a]

Salt	[Salt] (M)	pM^+	$pH_{0.5}$	$p(K_dK_a)$	$p(K_aK_{assc})$
NaCl	0.1	1.0	9.6(1)	-	8.6(1)
	0.5	0.3	8.6(1)	-	8.3(1)
LiCl	0.1	1.0	8.9(1)	9.9(2)	-
	0.5	0.3	9.9(2)	10.2(2)	-
KCl	0.1	1.0	8.9(3)	9.9(3)	-
	0.5	0.3	10.2(2)	10.5(2)	-
CsCl	0.1	1.0	9.5(2)	10.5(2)	-
	0.5	0.3	11.1(1)	11.4(1)	-

[a]All the given values are the average of at least two independent measurements and the error represents the range of measured values.

Thus far we have utilized the bulk hydronium and cation concentrations to determine the pK_a^{eff} values. However, most surface models consider that the surface concentration of the hydronium ion and cations are not equal to their corresponding bulk concentrations but can be related to the bulk concentration by a potential dependent term. If we consider the surface concentrations then equation 2.4 (for sodium ion) and equation 2.8 (for other alkali ions) take different forms. For sodium ions that stabilize the more charged surface, we assumed that the surface concentration ratio of $[H_3O^+]$ and $[M^+]$ was equal to that of the bulk concentration ratio. However, according to the triple layer model, the hydronium ions can partition to the 0-plane, while the larger cations are present at the β-plane. Consequently, a more accurate depiction of pK_a^{eff} is:

$$K_a^{eff} = K_a K_{assc} = \frac{[SiO^- \cdot M^+][H_3O^+]_s}{[SiOH][M^+]_s}$$

$$= \frac{[SiO^- \cdot M^+][H_3O^+]_b \exp\left(\dfrac{e\Phi_0}{kT}\right)}{[SiOH][M^+]_b \exp\left(\dfrac{e\Phi_\beta}{kT}\right)} \quad , \tag{2.10}$$

where e is the elementary charge, Φ_β is the potential at the β-plane, k is the Boltzmann constant and T is the temperature in Kelvin. Taking the negative logarithm of equation 2.10 and determining it at the point where the siloxide and silanol ratio is one yields:

$$pK_a^{eff} = p(K_a K_{assc}) = (pH_{0.5})_b - (pM^+)_b + \frac{e(\Phi_0 - \Phi_\beta)}{2.303kT} \tag{2.11}$$

For the other alkali ions, such as Li^+, K^+ and Cs^+, that stabilize the less charged or neutral pH surface, the equilibrium expression is given by:

$$pK_a^{eff}{}' = p(K_d K_a) = (pH_{0.5})_b + (pM^+)_b + \frac{e(\Phi_0 + \Phi_\beta)}{2.303kT} \tag{2.12}$$

To obtain the surface pH where half of the given silanol groups dissociated, $(pH_{0.5})_s$, we plotted the interfacial potential, Φ_0, as a function of surface pH (Figure 2.5). Surface pH values were determined from

$$(pH)_s = (pH)_b + \frac{e\Phi_0}{2.303kT} \tag{2.13}$$

using the interfacial potential, Φ_0, at different $(pH)_b$ values. To determine the interfacial potential at a given bulk pH, we used the relationship:

$$\Phi_0 = f \times \Phi(0)_{max} \tag{2.14}$$

where f is the fraction of deprotonation determined by combining the experimental data for the low pH and high pH titrations as described section 2.3.4 of this chapter and $\Phi(0)_{max}$ is the maximum interfacial potential at high pH values (pH $\geq$ 12.5), which was reported to be 140 mV for 0.5 M NaCl as measured by Eisenthal and coworkers.[30] The $(pH_{0.5})_s$, values determined from the sigmoid fitting of the Φ_0 vs. $(pH)_s$ titration curves are listed in Table 2.3.
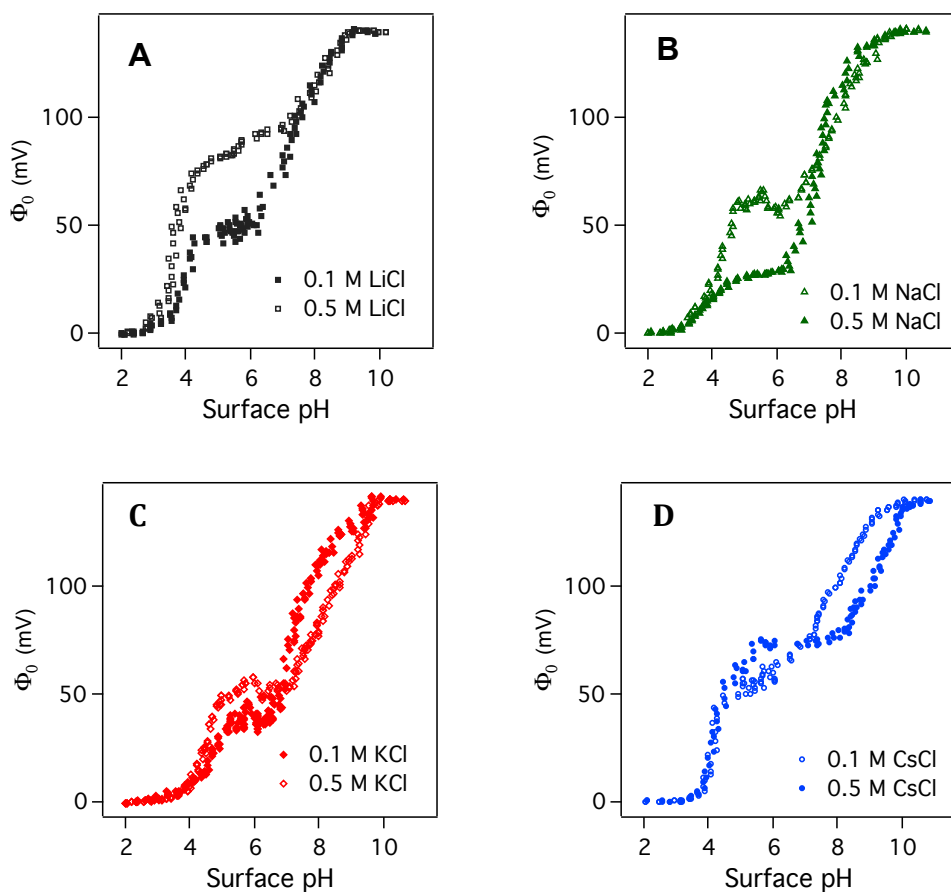
Figure 2.5 Interfacial potential, Φ_0 ($\Phi_0 = f \times \Phi(0)_{max}$), as a function of surface pH for the silica/electrolyte interface at 0.1 M and 0.5 M concentration of (A) LiCl, (B) NaCl, (C) KCl, and (D) CsCl. Solid and dashed line represent the sigmoid fit to the titration data for LA sites at 0.5 M and 0.1 M salts, respectively. $(pH_{0.5})_s$ is determined from the surface pH at the half of the sigmoid fit to the data.

To calculate the surface potential at the β-plane, Φ_β, experienced by the cations, we used the ion specific inner-layer capacitance (C_1) value that relates the surface charge density at the 0-plane (σ_0) to the drop in potential (Φ_0-Φ_β) at a distance β (different for different cations) according to the following equation:

$$C_1 = \frac{\sigma_0}{\Phi_0 - \Phi_\beta} \qquad (2.15)$$

The surface charge density σ_0 that corresponded to each Φ_0 was determined from:

$$\sigma_0 = f \times \sigma_{max} \qquad (2.16)$$

where the maximum surface charge density σ_{max} is 0.139 C/m^2 as measured by Eisenthal and coworkers,[30] and f is the fraction of deprotonation as determined from our ion specific experiments.

In our calculation of Φ_β, we utilized the predicted triple layer model capacitances, C_1, for the cations at the quartz/water/electrolyte interface.[46] As proposed by Sverjensky the capacitance, C_1, can be expressed in terms of the distance β as follows:

$$\frac{1}{C_1} = \frac{\beta}{(8.854)\varepsilon_{int}} \qquad (2.17)$$

where C_1 is the inner-layer capacitance, β is the distance of the β-plane from the 0-plane, and ε_{int} is the dielectric constant of water in the first layer. The position of the β plane can be determined from the hydrated ion radius r_{M^+} and a distance parameter r_1 by the equation: $\beta = r_{M^+} + r_1$. The distance parameter r_1 expresses the distance of the closest approach of the cation to the 0-plane and may vary depending on the nature of the interface. Using the effective dielectric constant,

ε_{int} = 62, and the distance parameter, r_1 = 3.7 Å for the quartz surface, the inner-layer capacitances, C_1 (in µF.cm^{-2}) were determined to be 90 for Li$^+$, 99 for Na$^+$, 108 for K$^+$, and 102 for Cs$^+$. These C_1 values were used to calculate the potential at the β-plane (Φ_β) from equation 2.19, and thus to determine the pK_a^{eff} values in equation 2.11 and 2.12. We obtained very low values for the Φ_β, indicating that at this high salt concentration the cations form a compact layer on the charged surface. However, our calculated Φ_β values for Li$^+$ and Na$^+$ were slightly negative, which is practically unlikely for these systems. We attributed that these strongly hydrated ions with larger hydrated radii, r_{M^+}, get partially dehydrated at the interface. So the hydrated radii that were used to calculate C_1 might be larger than the actual values leading to a lower or slight negative Φ_β value. Consequently, we calculated the pK_a^{eff} and $pK_a^{eff}{}'$ values for these ions with a Φ_β of zero.

Table 2.3 represents the values obtained for the pK_a^{eff} and $pK_a^{eff}{}'$ for all the alkali chlorides with 0.1 M and 0.5 M salts at the interface using the corresponding Φ_β values. We observed that the trends in effective pK$_a$ values obtained for 0.1-M salts after using this approach is pK_a^{eff} (NaCl) $< pK_a^{eff}{}'$ (LiCl) $\approx pK_a^{eff}{}'$ (KCl) $< pK_a^{eff}{}'$ (CsCl). Therefore, the original trend obtained for 0.5-M salts were preserved for the cations even at lower electrolyte concentration (0.1 M) although the (pH$_{0.5}$)$_s$ values were very similar for the 0.1 M data and do not follow the trend where instead Li$^+$ and K$^+$ have the lowest (pH$_{0.5}$)$_s$ value followed by Na$^+$ and Cs$^+$. These observations support the importance of using this approach

for measuring more accurate acid-base behavior of the mineral oxide/water interfaces.

Table 2.3 Thermodynamic Parameters from the Salt Concentration Variation Experiments Using the Surface Concentrations of the Ionic Species.

M^+	$[M^+]$	$(pH_{0.5})_b$	$(pH_{0.5})_s$	pK_a^{eff}	$pK_a^{eff\,\prime}$
Na^+	0.5	8.6	7.3	7.0	-
	0.1	9.6	7.8	6.8	-
Li^+	0.5	9.9	8.0	-	8.3
	0.1	8.9	7.4	-	8.4
K^+	0.5	10.2	8.5	-	8.7
	0.1	8.9	7.4	-	8.3
Cs^+	0.5	11.1	9.2	-	9.2
	0.1	9.5	7.9	-	8.6

2.2.5 Effects of Salt Concentration on the Relative Population of Silanol Sites

The relative population of the silanol groups also depended on the concentration of the cations as made clear by Figure 2.6. The percentage of more acidic silica sites decreased from 60(3)% to 35(6)% for LiCl, from 40(7)% to 27(4)% for KCl, and from 52(6)% to 40(6)% for CsCl with the decrease of salt concentration indicating that the presence of these salts decreased the number of less acidic sites on the surface. Other work has shown that the silica/LiCl(aq) electrolyte interface showed the maximum dependence of charge density on salt concentration by giving about 1.5-fold increased charge density when the salt concentration increased from 0.1 M to 0.5 M at pH 7,[47] which is qualitatively

consistent with our concentration dependent $f_{pH7}(\%)$ values with LiCl. On the

other hand, decrease of NaCl concentration at the interface increases the more

acidic sites and thus increases the percent of deprotonated at pH 7 from 20(2)% to

44(4)%. This observation once again supports our argument that the ion-pair

formation between Na^+ and SiO^- facilitates the strong hydrogen bonding network

at the interface and thus increases the amount of less acidic silanol groups with

higher concentration of NaCl salt. Recently, Sulpizi and coworkers investigated

the interfacial hydrogen bonding using density functional theory-based molecular

dynamics simulation and hypothesized that less acidic strongly hydrogen bonded

Si-OH groups accept hydrogen-bonding from water molecules and also remain

hydrogen-bonded with the neighboring surface Si-OH groups.[48] It is possible that

Na^+ stabilizes the hydrogen-bonding between two neighboring Si-OH groups by

forming inner sphere complexes at this plane. That could be one reason why the

percent of deprotonation decreases or the number of less acidic sites on the

surface increases with the increase of NaCl concentration.
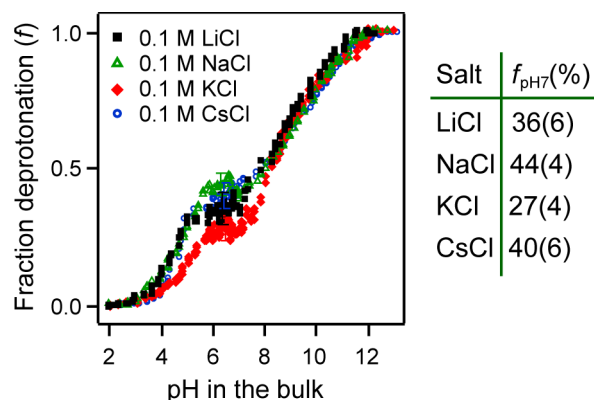
Figure 2.6 The fraction of deprotonated surface sites as a function of solution pH
for the silica/electrolyte interface at 0.1 M salt concentration. Table: the percent
deprotonated of the silica/electrolyte interface at pH 7 in presence of 0.1 M salts.

Another important observation to note is that at low salt concentration there is no particular trend in the *f* traces for different cations as shown in Figure 2.6. Percentages of deprotonation at pH 7 remain unaffected or very slightly affected by the specific ions present in the aqueous phase of the interface as all the values found were within the error (see inset Table of Figure 2.6). The similar *f* traces for all alkali ions indicate that the specific cation effects on the bimodal distribution of the silanol groups almost disappear at low concentration. This observation also supports that the structure of the interfacial water molecules, which is responsible for different population of the two silanol groups, are not influenced by the identity of the cations at 0.1 M electrolyte concentration.

2.3 Concluding Remarks

In conclusion, the surface charge density and corresponding acid-base equilibria for the silica/water interface are very sensitive to the nature of the alkali chloride electrolyte over a broad pH range at salt concentrations of 0.5 M. We proposed two models for the different alkali chlorides to explain the ion specific behavior and concentration dependence of the acid-base equilibra at the silica/water interface. In the model to describe sodium ion effects, we proposed that the silanol groups first dissociate to give siloxide ions that associate with the Na^+ ion through electrostatic interaction, whereas to describe other alkali ion effects we proposed that the silanol groups remain associated with the cations and first step of the acid-base equilibria is the cation dissociation from the silanol. However, we cannot rule out other contributions from the cations that change the

bimodal distribution at the interface such as surface restructuring, which could result in a hydrophobic surface that favors more acidic silanol groups.[14] Nevertheless, these results support that equilibrium behavior and the bimodal distribution of acidic sites depend strongly on the specific ion present in the aqueous phase, particularly at salt concentrations around 0.5 M. Thus, the binding behavior of silica should vary widely at the same pH depending on the concentration and identity of the alkali ion present. The trend in equilibrium constants and site distributions suggests that ion-surface, ion-water, and water-surface interactions can all play significant roles. Consequently, we expect such effects to be general for a variety of other interfaces beyond silica. As surface pK_a values are common parameters in environmental and biological models, properly modeling the influence of the electrolyte identity on interfacial acid-base equilibria will be necessary to improve model accuracy.

2.4 Experimental

2.4.1 General Considerations

All experiments were carried out at least two times and the given errors in the reported data indicate the range of measured values. Highly deionized (18.2 MΩ·cm) water was always used freshly that was purified by a MilliQ-Plus ultrapure water purification systems manufactured by Millipore corporation. pH of all the solutions were measured by using a pH meter (Orion 2 star, Thermo scientific). The pH meter was calibrated with pH 4.00 and pH 7.00 buffers when

the working range was pH 7 to pH 2 and it was calibrated with pH 7.00 and pH 10.00 buffers when the range was pH 7 to pH 13.

2.4.2 Laser Setup

A schematic representation of our laser set up is shown in Figure 2.7. A femtosecond Ti:Sapphire oscillator (Spectra Physics, Mai Tai, 80 MHz, 1.0 W) was used to produce pulses centered at 800 nm (<100 fs, FWHM ~12 nm). This pulse was used as the seed pulse in a regenerative amplifier (Spitfire Pro, Spectra Physics) pumped by a Nd:YLF laser (Spectra Physics, Empower, 11.5 W), which resulted in fs-pulses with high peak power (1 kHz, 2.4 mJ per pulse). This Spitfire output was then passed through a 30/70 beam splitter and the transmitted portion (1 kHz, 1.1 mJ) is used to pump an optical parametric amplifier (Spectra Physics OPA-800CF) to produce light tunable in the visible region. In our experiments, the wavelength of the incident light was tuned to 550 ± 2 nm. The reflected light (1 kHz, 2.3 mJ) is used to pump another computer-controlled optical parametric amplifier (Coherent, TOPAS) to generate tunable IR light, which is used for sum frequency generation (SFG) as discussed in chapter 3.
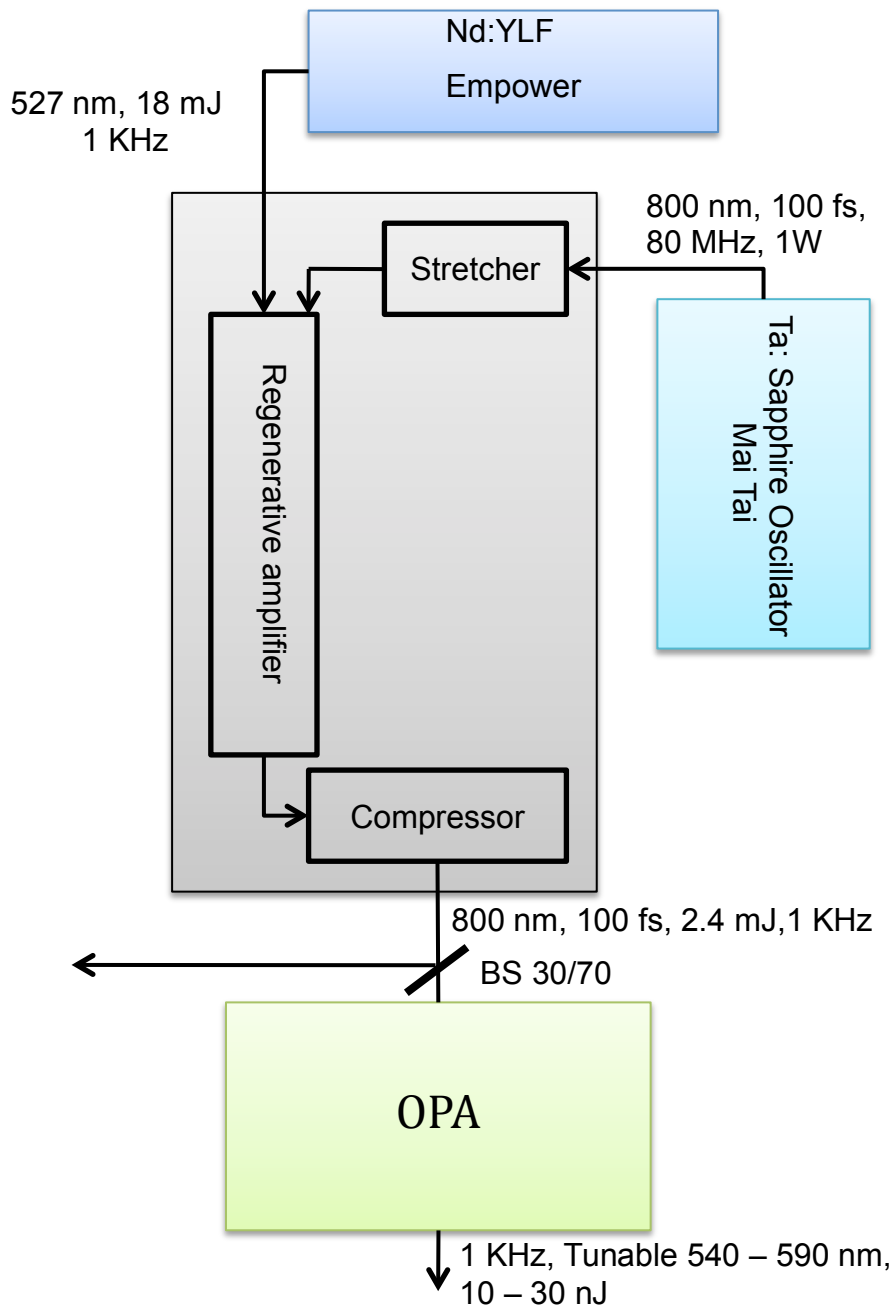
Figure 2.7 Schematic representation of our laser system. Femtosecond pulse from Ti:Sapphire oscillator seeds a regenerative amplifier, which is pumped by a Nd:YLF laser. The amplified beam is spitted up by passing it through a 30/70 beam splitter (BS 30/70) and the transmitted light is used to pump an optical parametric amplifier (OPA) to generate a visible light tunable in 540 – 590 nm range.

2.4.3 SHG Experiments

After attenuation by a dual wheel neutral-density filter (New Focus, cat. #5215), light from the OPA (λ = 550 nm) was passed through a $\lambda/2$ wave plate and Glen- Thompson polarizer (B. Halle, UV-grade Calcite, PGT 4.10) to generate s-polarized light, which was then focused on the interface of a fused silica hemisphere and water. Experiments were also performed with p-polarized light, which led to SHG that exhibited the same pH-dependent behavior. As shown in Figure 2.8, we monitored SHG in reflection geometry with the incident beam 62° from surface normal. The incident light was attenuated to 0.3-0.5 μJ per pulse, because incident power > 0.8 μJ per pulse led to deviations from the expected quadratic relationship between incident power and SHG signal intensity, suggesting that other nonlinear optical processes contributed or the sample was becoming damaged. The SHG light (λ = 275 nm) emanating from the interface was recollimated and focused onto a monochromator (Optometrics Corp., Mini-Chrom MC1-02) connected to a photomultiplier tube (PMT, Hamamatsu Photonics). Prior to entering the monochromator, a bandpass colored glass filter (Thorlabs, UG5) was used to filter out the reflected fundamental (550 nm). The PMT electric response was then amplified and counted with a gated photon counter (Stanford Research Systems). The quadratic power dependence and SHG wavelength dependence were first monitored and confirmed before performing each pH-variation experiment.
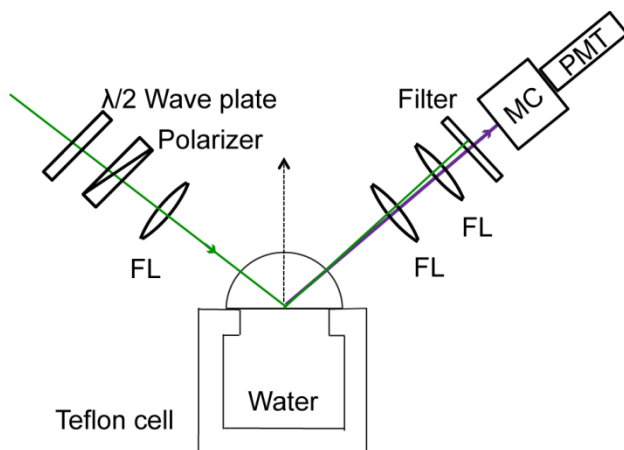
Figure 2.8 Bird's eye view of the second harmonic generation assembly. The fundamental light at ω is shown in green, while the SH light is shown in purple. FL = focusing lens, MC = monochromator, PMT = photomultiplier tube. A fused silica hemisphere is screwed onto the sample cell, which places it in contact with the aqueous reservoir.

2.4.4 Materials

Cesium chloride (99.9%), cesium hydroxide (99.9%, 50 wt% solution in water), lithium chloride (≥99%), and lithium hydroxide (≥98%) were purchased from Sigma-Aldrich. Sodium chloride (≥99%), and sodium hydroxide (≥97%) were purchased from EMD Chemicals Inc. Potassium chloride (≥99%) was purchased from Analchemia Canada Inc, and potassium hydroxide (≥85%), sulfuric acid and hydrochloric acid were obtained from Caledon Laboratory chemicals. All compounds were used without further purification. Ultrapure deionized (18.2 MΩ·cm) water was used shortly after deionization by a MilliQ-Plus ultrapure water purification system (Millipore). The pH of all the solutions was measured with an Orion 2 star pH meter from Thermo Scientific using a double-junction Ag/AgCl (Orion, 9107APMD).

2.4.5 Surface and Solution Preparations

A fused silica hemisphere (ISP optics, 1 inch diameter, QU-HS-25, UV-grade SiO_2) was Cleaned and then placed on a custom-built Teflon cell mounted onto an assembly of translational stages, so the cell could be moved in the x,y and z directions. The silica/water interface was perpendicular to the laser table, and the aqueous phase was exposed so the pH could be routinely changed and monitored. Prior to use, the hemisphere was cleaned with sonication in water followed by methanol and then the flat surface of the hemisphere was covered with a few drops of commercially available glass cleaner Nochromix (Godax Laboratories Inc., ~0.25 g in 5 mL H_2SO_4) for 1 hour followed by copious rinsing in Milli-Q water. The lens was then sonicated three times while immersed in Milli-Q water (5 minutes × 3) followed by methanol (5 minutes), and dried in an oven at 100 ºC for 10 minutes. Finally, the cooled hemisphere was subjected to plasma cleaning (Plasma cleaner, PDC-32G, Harrick Plasma) in air for 3 minutes.

2.4.6 pH Variation Experiments

Each sample was aligned in the presence of water until the SHG signal was optimized. The direct exposure of quartz to neutral water leads to a strongly hydrogen bonded interfacial water layer,[49] and so it is likely contact with water is important prior to the addition of the salt solution. Next, the water was completely removed and ~ 10 mL of electrolyte solution was added to the sample cell. Separate experiments were performed on different fresh samples for the lower and higher pH regions to avoid hysteresis.[50] For the lower pH experiments, the electrolyte solution was first adjusted to pH 7, whereas for the higher pH

70

experiments, the pH of the electrolyte solution was not adjusted for the first data point. This was done to ensure that both experiments captured the flat region between pH 6 and 7, so that the two experiments could be combined as described for Figure 2.5. After adding the electrolyte solution, SHG was monitored for 30 minutes to confirm that the silica/electrolyte interface had reached equilibrium. For the lower pH range, small aliquots of an HCl solution with the same electrolyte concentration were then added and the resulting bulk pH was measured while allowing the sample to equilibrate for 3 minutes. SHG was collected for ~ 2 minutes thereafter and the sequence of steps was repeated. Data for the higher pH range was similarly acquired but small aliquots of an alkali hydroxide solution with the same electrolyte concentration were added instead of HCl. All of the titration curves shown in the figures, with the exception of figure 2.5, are a single experiment that is representative of the data. To illustrate the high-level of reproducibility in these experiments, we include all of the data collected at least in duplicate in the supporting information. The one exception, figure 2.5, represents a compilation of all of the normalized high and low pH data and the corresponding normalization combinations as described by equations 2.2 and 2.3. This compiled data was smoothed using the Box smoothing function in Igor Pro (version 6.05) with a smoothing factor of 7 for all of the alkali chlorides except for KCl. For KCl a smoothing factor of 15 was used since this data set represented experiments performed in triplicate.

2.4.7 Data Fitting

SHG intensity was collected using the LabVIEW 2009 data acquisition program (National Instruments). The square root of the measured SHG intensity (averaged over at least 100 counts) yielded the magnitude of the SHG E-field ($E_{2\omega}$). We then divided $E_{2\omega}$ by the incident laser intensity to account for changes in $E_{2\omega}$ due to incident intensity fluctuations. (Power fluctuations were usually minimal during the course of the experiment, ± 0.03 mW). To determine the pH at which half of the acidic or less acidic silanol groups were deprotonated, the resulting $E_{2\omega}$ versus pH trace corresponding to either pH 2 to pH 7 or pH 7 to pH 12.5, was normalized from zero to one. A sigmoidal function was fit to the normalized $E_{2\omega}$ versus pH data using Igor Pro (version 6.05) software according to:

$$f = base + \frac{max}{1 + \exp(\frac{x_{half} - x}{rate})} \quad ,$$

(2.20)

where x_{half} corresponds to the pH where $E_{2\omega}$ is equal to 0.5 ($pH_{0.5}$), *rate* determines the sharpness of the transition, and *max* and *base* are 1 and 0, respectively. Both the rate and x_{half} parameters were allowed to vary. The pK_a^{eff} values in Table 2.1 were calculated as described in the manuscript using the average $pH_{0.5}$ values determined for duplicate or triplicate experiments. The error in all pK_a^{eff} values represents the range of $pH_{0.5}$ values determined from the individual titrations.

To calculate the fraction deprotonated *f*, separate experiments were

performed at low and high pH, and each experiment was normalized by the average $E_{2\omega}$ value in the flat region at neutral pH ($E_{2\omega}$(pH 7)), resulting in the relative SHG ($rE_{2\omega}$):

$$rE_{2\omega} = \frac{E_{2\omega}}{E_{2\omega}(pH7)} \qquad (2.21)$$

The relative $E_{2\omega}$ values from both the high and low pH experiments were then combined and converted to the relative surface charge density (f) according to:

$$f = \frac{rE_{2\omega} - rE_{2\omega}(pH2)}{rE_{2\omega}(pH12.5) - rE_{2\omega}(pH2)} \qquad (2.22)$$

The f values reported in figure 2.4 are the average of at least two sets of experiments and four compiled high and low pH data sets, with the error representing the range of measured values. Figure 3 represents a compilation of all of the normalized high and low pH data and the corresponding normalization combinations. This compiled data was smoothed using the Box smoothing function in Igor Pro (version 6.05) with a smoothing factor of 7 for all of the alkali chlorides except for KCl. For KCl a smoothing factor of 15 was used since this data set represented experiments performed in triplicate.

2.4.8 Aqueous Bicarbonate Titrations

A freshly prepared alkali bicarbonate solution (0.1 M, 20 mL) was transferred to an Erlenmeyer flask and then titrated with the corresponding 0.1-M solution of alkali hydroxide (0.1 M MOH) in a burette. For Li^+, a 0.1-M LiOH solution was used to titrate a 0.1-M solution of $NaHCO_3$ because $LiHCO_3$ was not

available. After each addition of MOH (~0.5 mL), the pH of the bicarbonate solution was measured. The endpoint of the titration was determined by fitting the S-shaped regime of the titration curve with equation 1, where x_{half} corresponded to one equivalent of MOH having been added. Using this relationship, the volume (mL) of MOH was converted into the number of equivalents of MOH. The pH corresponding to 0.5 equivalents of MOH then yielded the pK_a^{eff} for that alkali bicarbonate (Figure 2.2C, Table 2.1).

2.5 References

(1)   Dove, P.; Craven, C. *Geochim. Cosmochim. Acta* **2005**, *69*, 4963.

(2)   Karlsson, M.; Craven, C.; Dove, P. M.; Casey, W. H. *Aquat. Geochem.* **2001**, *7*, 13.

(3)   Borah, J. M.; Mahiuddin, S.; Sarma, N.; Parsons, D. F.; Ninham, B. W. *Langmuir* **2011**, *27*, 8710.

(4)   Appelo, C. A. J.; Postma, D. *Geochemisytry, Groundwater and Pollution*; 2 ed.; A. A. Balkema Publishers: Amsterdam, **2005**.

(5)   Lützenkirchen, J. *Environ. Sci. Technol.* **1998**, *32*, 3149.

(6)   Lützenkirchen, J. *J. Coll. Interf. Sci.* **1999**, *217*, 8.

(7)   Simon, S. d.; Richmond, G. L. *J. Phys. D: App. Phys.* **2008**, *41*, 033001.

(8)   Campen, R. K.; Pymer, A. K.; Nihonyanagi, S.; Borguet, E. *J. Phys. Chem. C* **2010**, *114*, 8465.

(9)   Corma, A.; Garcia, H. *Adv. Synth. Catal.* **2006**, *348*, 1391.

(10)   Schena, M.; Shalon, D.; Davis, R. W.; Brown, P. O. *Science* **1995**, *270*, 467.

(11)   Heise, C.; Bier, F. F. *Top. Curr. Chem.* **2006**, *261*, 1.

(12)   Iler, R. K. *Chemistry of Silica - Solubility, Polymerization, Colloid and Surface Properties and Biochemistry*; John Wiley & Sons, **1979**.

(13)   Eisenthal, K. B. *Chem. Rev.* **1996**, *96*, 1343.

(14)   Leung, K.; Nielsen, I. M. B.; Criscenti, L. J. *J. Am. Chem. Soc.* **2009**, *131*, 18358.

(15)   de Beer, A.; Campen, R.; Roke, S. *Phys. Rev. B* **2010**, *82*.

(16)   Zhang, Y.; Cremer, P. *Curr. Opin. Chem. Biol.* **2006**, *10*, 658.

(17)   Jungwirth, P.; Tobias, D. J. *Chem. Rev.* **2006**, *106*, 1259.

(18)   Bian, H.-t.; Feng, R.-r.; Guo, Y.; Wang, H.-f. *J. Chem. Phys.* **2009**, *130*, 134709.

(19)   *Specific Ion Effects*; Kunz, W., Ed.; World Scientific: Singapore, **2010**.

(20)   Salis, A.; Parsons, D. F.; Bostrom, M.; Medda, L.; Barse, B.; Ninham, B. W.; Monduzzi, M. *Langmuir* **2010**, *26*, 2484.

(21)   Beildeck, C. L.; Steel, W. H.; Walker, R. A. *Faraday Discuss.* **2005**, *129*.

(22)   Gopalakrishnan, S.; Liu, D.; Allen, H. C.; Kuo, M.; Shultz, M. J. *Chem. Rev.* **2006**, *106*, 1155.

(23)   Yang, Z.; Li, Q.; Chou, K. C. *J. Phys. Chem. C* **2009**, *113*, 8201.

(24)   Kosmulski, M. *J. Coll. Interf. Sci.* **2002**, *253*, 77.

(25)   Franks, G. V. *J. Coll. Interf. Sci.* **2002**, *249*, 44.

(26)   Ostroverkhov, V.; Waychunas, G.; Shen, Y. *Phys. Rev. Lett.* **2005**, *94*.

(27)   Dong, Y.; Pappu, S. V.; Xu, Z. *Anal. Chem.* **1998**, *70*, 4730.

(28)   O'Reilly, J. P.; Butts, C. P.; I'Anson, I. A.; Shaw, A. M. *J. Am. Chem. Soc.* **2005**, *127*, 1632.

(29)   Fisk, J. D.; Batten, R.; Jones, G.; O'Reill, J. P.; Shaw, A. M. *J. Phys. Chem. B* **2005**, *109*, 14475.

(30)   Ong, S.; Zhao, X.; Eisenthal, K. B. *Chem. Phys. Lett.* **1992**, *191*, 327.

(31)   Zhao, X.; Ong, S.; Wang, H.; Eisenthal, K. B. *Chem. Phys. Lett.* **1993**, *214*, 203.

(32)   Konek, C. T.; Musorrafiti, M. J.; Al-Abadleh, H. A.; Bertin, P. A.; Nguyen, S. T.; Geiger, F. M. *J. Am. Chem. Soc.* **2004**, *126*, 11754.

(33)   Du, Q.; Freysz, E.; Shen, Y. *Phys. Rev. Lett.* **1994**, *72*, 238.

(34)   Du, Q.; Freysz, E.; Shen, Y. R. *Phys. Rev. Lett.* **1994**, *72*, 238.

(35)   Duval, Y.; Mielczarski, J. A.; Pokrovsky, O. S.; Mielczarski, E.; Ehrhardt, J. J. *J. Phys. Chem. B* **2002**, *106*, 2937.

(36)   Pearson, R. G. *J. Chem. Educ.* **1968**, *45*, 581.

(37)   Collins, K. D. *Biophys. Chem.* **2006**, *119*, 271.

(38)   *CRC handbook of chemistry and physics*; 92 ed.; CRC Press: Boca Raton, FL, **2011**.

(39)   Chen, X.; Yang, T.; Kataoka, S.; Cremer, P. S. *J. Am. Chem. Soc.* **2007**, *129*, 12272.

(40)   Onorato, R. M.; Otten, D. E.; Saykally, R. J. *Proc. Natl. Acad. Sci.* **2009**, *106*, 15176.

(41)   Collins, K. D.; Washabaugh, M. W. *Quart. Rev. Biophys.* **1985**, *18*, 323.

(42)   Cacace, M. G.; Landau, E. M.; Ramsden, J. J. *Quart. Rev. Biophys.* **1997**, *30*, 241.

(43)   Kielland, J. *J. Am. Chem. Soc.* **1937**, *59*, 1675.

(44)   Rahnemaie, R.; Hiemstra, T.; van Riemsdijk, W. H. *J. Coll. Interf. Sci.* **2006**, *293*, 312.

(45)   Parsons, D. F.; BostroÃàm, M.; Maceina, T. J.; Salis, A.; Ninham, B. W. *Langmuir* **2009**, *26*, 3323.

(46)   Sverjensky, D. A. *Geochimica et Cosmochimica Acta* **2001**, *65*.

(47)   Milonjic, S. K. *Coll. Surf.* **1987**, *23*, 301.

(48)   Gaigeot, M.-P.; Sprik, M.; Sulpizi, M. *J. Phys.: Condens. Matter* **2012**, *24*, 124106.

(49)   Li, I.; Bandara, J.; Shultz, M. J. *Langmuir* **2004**, *20*, 10474.

(50)   Gibbs-Davis, J. M.; Kruk, J. J.; Konek, C. T.; Scheidt, K. A.; Geiger, F. M. *J. Am. Chem. Soc.* **2008**, *130*, 15444.

CHAPTER 3

Specific Anion Effects on the Acid-Base Behavior of

the Silica/Water Interface

3.1 Introduction

The silica/water interface is involved in numerous geochemical, environmental, and industrial processes. Many of these processes such as pollutant transport and weathering involve the electrostatic interactions of aqueous species with the charged oxide surface and thus largely depend on the acid-base chemistry of the silica/water interface.[1-3] Consequently, there is a long history of research aimed at identifying the dissolution and acid-base chemistry of silica, particularly for colloidal and gel morphologies.[4-7]

One challenge in monitoring acid-base equilibria of silica particles is that the stability of colloidal dispersions is often pH dependent.[4] As a result, many potentiometric methods employed to monitor the change in particle mobility as a function of charge can only operate over a limited pH range, making it difficult to map out the entire acid-base equilibrium. One way to avoid aggregate instability is to study the macroscopic planar silica/water interface. Nonlinear optical methods like second harmonic generation and sum frequency generation can be utilized to monitor these buried interfaces based on the break in centrosymmetry that the interface presents.[8-12] For example, using vibrational sum frequency generation (SFG), the interfacial hydrogen-bonding network of water at the silica interface has been studied as a function of pH[13-17] and electrolyte composition.[18] From the SFG spectra, Shen and co-workers concluded in the first investigation at this interface that two major populations of water were present, one weakly coordinated and the other strongly coordinated with respect to hydrogen bonds.[13] As the pH was made more basic, the relative distribution of these two populations

varied significantly. Second harmonic generation (SHG), a related nonlinear optical technique, has been used as a complementary method to probe changes in the potential of the interface. Monitoring the SHG signal as a function of pH indicated that the planar silica/water interface possessed two unique acidic sites.[19-21] This bimodal behavior is unusual for mineral oxide interfaces and has been attributed to different hydrogen-bonding environments of the two silanol sites that lead to stark differences in acidity.[22,23]

Another feature of the silica-water interface that has long interested scientists is the sensitivity of dissolution and surface deprotonation processes to ionic strength[16,17,24,25] and electrolyte composition of the aqueous layer.[18,26-29] Regarding the latter, these specific ion effects reveal that not just the charge but the polarizabity of the ions in the aqueous phase can influence their properties.[30,31] For example, Dove and co-workers found that the dissolution rate of silica varied depended on the identity of the solution-phase alkali and alkaline earth ions present. [24,27,29] They attributed this specific ion dissolution behavior to the ability of the ion to form inner sphere interactions with the silica sites, which facilitated hydrolysis of the O-Si bond coordinated to the cation.[29] Regarding surface deprotonation, Ninham and co-workers[32] and Dove and Craven[33] examined the change in surface charge density using potentiometric methods over a narrow pH range for mesoporous silica and colloidal silica, respectively, dispersed in different alkali chloride solutions. Both reports found that the 6.5-8.5 pH range yielded different surface charge densities depending on the cation present, with potassium leading to the greatest density of charged sites on silica.

Our group has been interested in using second harmonic generation spectroscopy to monitor specific ion effects on acid-base equilibria at the planar silica/water interface. Recently, we monitored the deprotonation of the two types of acidic sites in the presence of different alkali chloride electrolytes over a wide pH range using SHG.[21] We found that the corresponding acid dissociation constants (K_a) for the two sites were very sensitive to the composition of the aqueous electrolyte, with Na^+ leading to the greatest effective K_a and Cs^+ leading to the lowest effective K_a. We attributed this trend in effective K_a values to the stronger interaction of the sodium with the siloxide sites in comparison to the larger, more polarizable cesium. Not only was the measured K_a very sensitive to the nature of the electrolyte, but the population distribution of the two acidic sites also varied greatly depending on the alkali ion. Overall, these studies supported that specific interactions between the cation and siloxide sites, as well as interactions between the alkali chloride and water, influenced the resulting acid-base behavior of the surface. [21,33]

One outstanding question that remains is whether the identity of the halide influences the acid-base chemistry of the silica/water interface. Although halides are generally known to have more significant specific ion effects on the interfacial hydrogen-bonded structure of water at the air/water,[34,35] protein/water[36] and polymer/water interfaces,[37] their influence has been much less explored on negatively charged surfaces like silica, where the point of zero charge occurs at pH 2.[38,39] To illustrate the former, both theoretical simulations and experimental studies have established that the air/water interface shows enhanced affinity for

certain anions like iodide. [31,35,40] Cremer and co-workers found that neutral Langmuir-Blodgett (LB) films of polymers and peptides also have a higher affinity for iodide or bromide than chloride.[36,37,41] This affinity of more polarizable anions like iodide and bromide for neutral LB film interfaces has been attributed to the weak interactions of the larger halides with water that allow it to interact more strongly with the protein or polymer interface, primarily through dipole interactions.[37,41]

In contrast to these air/water and LB film/water investigations, there has been less focus on specific anion effects of halides on negatively charged mineral oxide surfaces. For the planar silica-water interface where the interfacial water structure is expected to play an important role, we would expect the influence of the halide identity to be significant. Herein we apply SHG spectroscopy to monitor the influence of the interfacial halide ions on the effective pK_a of the acid-base equilibria, as well as the bimodal distribution of the two surface acidic sites. Not only do we observe significant effects of the halide identity on the ratio of the more acidic to less acidic sites, but we also observe cooperative acid-base behavior that depends on the nature of the halide ion. To the best of our knowledge, such striking evidence of cooperative deprotonation processes has never before been observed at a mineral oxide interface. Understanding such behavior is key to predicting the surface charge density of silica over a wide pH range, which is essential to both accurate environmental modeling as well as materials applications using silica as the substrate.

3.2 Results and Discussion

3.2.1 Background Theory of Second Harmonic Generation

Owing to its intrinsic surface-selectivity and sensitivity to interfacial charge, we selected SHG spectroscopy to monitor the influence of the interfacial halide ions on the acid-base behavior of the silica/water interface. SHG is a second order nonlinear optical process that occurs in noncentrosymmetric environments. For instance, at the interface of fused (noncrystalline) silica and bulk water, inversion symmetry is broken and SHG is allowed. Second harmonic generation occurs when light of frequency ω interacts with the interface leading to an induced polarization, $P_{2\omega}$, that oscillates at twice the incident frequency. This oscillating polarization generates the second harmonic electric field, $E_{2\omega}$. At a neutral surface, $E_{2\omega}$ depends on the incident electric field, E_{ω}, and the second order susceptibility, $\chi^{(2)}$, which, within the electic dipole approximation, is only non-zero for noncentrosymmetric environments like interfaces. However, Eisenthal and co-workers demonstrated that $E_{2\omega}$ generated from a charged surface is also enhanced by a third static electric field, the magnitude of which depends on the third-order susceptibility, $\chi^{(3)}$.[19,20] Consequently, $E_{2\omega}$ can be expressed as

$$E_{2\omega} \propto P_{2\omega} = \chi^{(2)} E_{\omega} E_{\omega} + \chi^{(3)} E_{\omega} E_{\omega} \Phi_0 , \qquad (3.1)$$

where Φ_0 is the interfacial potential due to the presence of surface charges. This $\chi^{(3)}$ technique has been widely used to monitor surface potentials,[42,43] electrostatic interactions,[44-47] and protonation/deprotonation processes[19,20,25,48-51] based on the second harmonic optical response that can be correlated with changes in the interfacial potential.

To monitor acid-base processes in particular, $\chi^{(3)}$ experiments are often performed at high electrolyte concentrations (~ 0.5 M) as the interfacial potential can be considered to vary linearly with the surface charge density at high ionic strength.[19-21,48,51] This linear dependence arises from the collapse of the diffuse double layer at high ionic strength, leaving only the compact Stern layer present that behaves like a parallel plate capacitor.[52] Under these conditions, $E_{2\omega}$ becomes a function of the potential within this condensed layer rather than the potential within the diffuse layer,[25] and the constant capacitance model can be used to relate the interfacial potential with the surface charge density.[53,54] Accordingly, decreases in SH signal, proportional to $\left|E_{2\omega}\right|^2$, can be correlated with a decrease in surface charge density (Scheme 3.1). As a result, a titration curve can be constructed simply by plotting the normalized $E_{2\omega}$ against solution pH, allowing the pH where half the sites have been deprotonated ($pH_{0.5}$) to be quantified.

Scheme 3.1 Decreasing the pH and Protonating Surface Sites Decreases the SH Signal.[a]
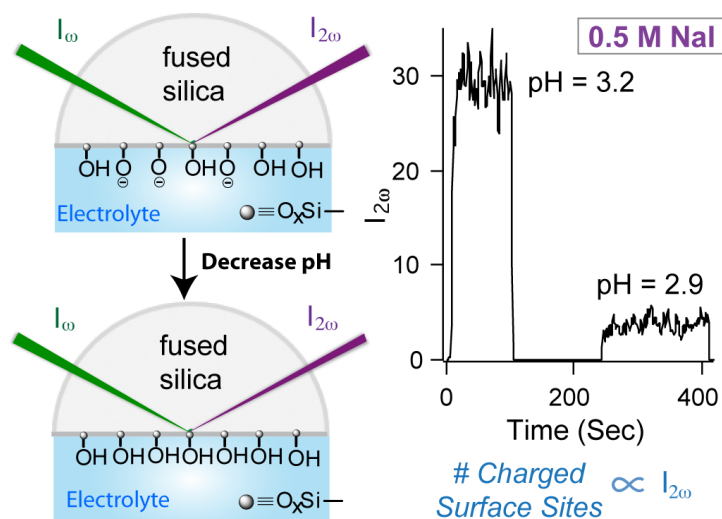
[a]I_ω is the incident intensity proportional to $\left|E_\omega\right|^2$. $I_{2\omega}$ is the SH signal intensity proportional to $\left|E_{2\omega}\right|^2$.

3.2.2 Acid-Base Titrations of the Silica/Electrolyte Interface with Varying Sodium Halides

Figure 3.1 illustrates representative acid-base titration profiles of the normalized SHG electric field versus solution pH. Consistent with previous reports, we observed two acid-base equilibria for the silica/water interface, representative of two distinct acidic sites: one more acidic site that dissociated below pH 7, and the other less acidic site that dissociated above pH 7 (Figure 1A and 1B, respectively).[19-21,51] As the sodium halide was varied, the titration curves for both the more acidic (MA) and less acidic (LA) silanol groups exhibited very dramatic shifts in position. For example, NaCl electrolyte led to a $pH_{0.5}$ value for the MA sites of 4.06(4) and a $pH_{0.5}$ value for the LA sites of 8.6(1). In contrast, in the presence of NaI the corresponding values of $pH_{0.5}$ were 3.2(1) and 11.3(1) for

86

the more acidic and less acidic sites, respectively. Unlike what was observed in the presence of different alkali chlorides where the trend in $pH_{0.5}$ was the same for both MA and LA sites,[21] the sodium halide data exhibited opposite trends for the two acidic groups. Specifically, NaI exhibited the lowest $pH_{0.5}$ value for the MA sites and the highest $pH_{0.5}$ for the LA sites. The opposite trends in $pH_{0.5}$ values for the MA and LA sites indicated that, in the presence of NaI electrolyte, the extent of deprotonation at pH 7 represented a stable configuration for the interface such that further protonation or deprotonation was not favorable until extremely acidic or basic pH conditions were reached. Furthermore, the sharpnesses of the titration curves also varied significantly with the nature of the halide ion. This change in sharpness, which was not observed upon varying the cation identity, suggested that the halide ions not only influenced the stability of the acidic sites but also influenced the mechanism of the acid-base reaction.
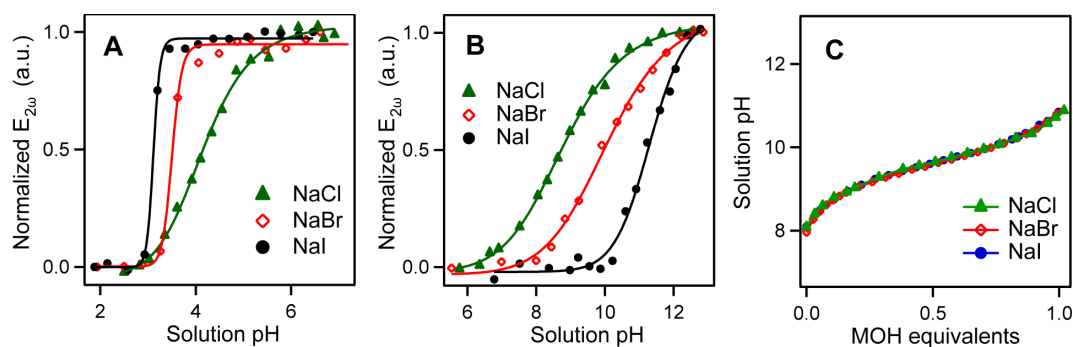
Figure 3.1 Representative titration curves for the silica/water interface in the presence of 0.5 M sodium halide salts. Normalized $E_{2\omega}$, which is proportional to the fraction of deprotonation of the silanol groups, is plotted as a function of (A) low pH and (B) high pH. The solid line is the sigmoidal fit of the titration data. (C) Titration curves for aqueous sodium bicarbonate in the presence of 0.5 M sodium halides, where pH is plotted against the equivalents of sodium hydroxide added.

As a point of comparison we monitored the deprotonation of a solution-phase acid, bicarbonate, in the presence of 0.5 M sodium halide. In the previous chapter (chapter 2) we demonstrated that the $pH_{0.5}$ values of this solution-phase acid varied slightly in the presence of different alkali chlorides, following the Hofmeister series $Li^+(pH_{0.5}) < Na^+(pH_{0.5}) < K^+(pH_{0.5}) < Cs^+(pH_{0.5})$.[21] For the anions, however, no difference in behavior was expected since, there should be minimal interaction between the bicarbonate or carbonate anion and the halide. As anticipated, we did not observe a significant difference in $pH_{0.5}$ values for the different sodium halides (Figure 3.1C). This lack of influence of the halide anion on the solution-phase bicarbonate equilibrium contrasted sharply with the behavior of the silica/water interface supporting that these specific halide effects are primarily interfacial effects, consistent with other specific ion studies.[41]

3.2.3 Quantifying the Acid-Base Behavior of the Silica/Electrolyte Interface with a Cooperative Model

What makes the acid-base chemistry of the interface so sensitive to the identity of the halide ion? To address this question, we focused on the sharpness of the titration curves for iodide and bromide, indicative of cooperative acid-base processes. For acid-base reactions, positive cooperativity occurs when the deprotonation of one site makes the second deprotonation event thermodynamically more favorable, while a decrease in favorability is associated with negative cooperativity. The overall equilibrium constant that represents these cooperative sites with coupled equilibria can be expressed as:

$$K_a^{eff} = K_1 K_2 K_3....K_n = \frac{[(SiO^-)_n][H_3O^+]^n}{[(SiOH)_n]} \qquad (3.2)$$

(SiOH)$_n$ and *(SiO$^-$)$_n$* represent the protonated and deprotonated states of the polymers, respectively, with *n* number of repeating silanol groups. The term, *n* in this equation refers to the number of cooperative sites that interact and has been used to describe cooperativity in amphiphilic polypeptides.[55] After introducing this cooperative term, the modified Henderson-Hasselbach equation becomes:

$$pH = pK_a^{eff} + \frac{1}{n}\log\left(\frac{\alpha}{1-\alpha}\right) \qquad (3.3)$$

where α is the fraction of one type of surface site that is deprotonated, equivalent to normalized $E_{2\omega}$.[55] The pH at which half the acidic sites are deprotonated for a given type of site (pH$_{0.5}$) corresponds to a log(α/(1-α)) value of zero. Therefore, according to this model the pH$_{0.5}$ that can be easily extracted from the titration profiles is equal to pK$_a^{eff}$.

There are numerous models for relating the composition of the electrolyte to the surface acidity of mineral oxides such as silica, some of which consider the effect of ion identity on surface deprotonation rather than cooperativity.[2,52,56-59] Owing to the clear influence of the anion on the sharpness of the titration profile, we utilize the approach presented above as it provides a simple physical model for understanding the influence of cooperativity on the acid-base chemistry of the surface. We note that in equation 3.3 we consider the solution pH rather than the surface pH to calculate the equilibrium constant K$_a^{eff}$. This constant based on the solution pH is sometimes referred to as the acid dissociation quotient Q$_a$ and is related to the K$_a$ derived from the surface pH by a potential-dependent term that

accounts for enhancement or depletion of the surface concentration of H^+ depending on the interfacial potential.[52] One advantage of using the solution pH is that it does not require knowledge of the absolute interfacial potential, which should differ at the same surface charge density depending on the ion identity and position within the electric triple layer.[59,60] Additionally, the solution pH transitions were so sharp in the presence of the larger halides that when the interfacial potential was plotted versus surface pH, the function deviated from sigmoidicity (Section 3.3.8, Figure 3.7). Finally, as discussed in chapter 2, the apparent (non-cooperative) K_a of the surface also reflects interactions between the cations and the siloxide sites.[9] In these specific cation studies the overall equilibrium expression for the apparent K_a included the cation concentration (where $K_a = [SiO^-M^+][H^+]/[SiOH][M^+]$). As the cation surface concentration also depends on the interfacial potential, to a first approximation the potential dependence of the surface hydronium concentration and surface cation concentration cancel out in the final equilibrium expression (see section 2.3.2). The contribution of the salt concentration to the measured K_a is systematic as the salt concentration is kept constant for all of the different electrolytes explored. Here we do not implicitly describe the salt dependence within the equilibrium expression but rather the effect of cooperativity. As a result, we focus our discussion on the trends in K_a rather than their absolute values.
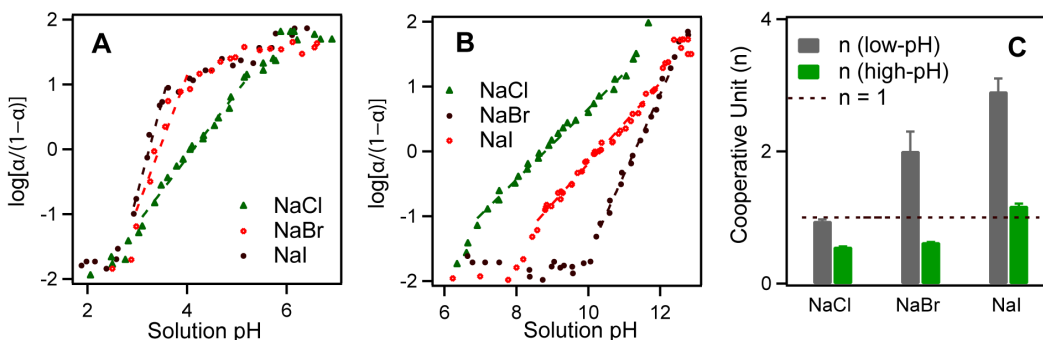
Figure 3.2 Representative plots of *log[α/(1-α)]* versus pH of the silica/water interface as a function of sodium halide (0.5 M) (A) at low pH and (B) at high pH. Dashed lines indicate the fit to the linear region of the modified Henderson-Hasselbalch equation, where the slope is equal to *n*. (C) Cooperative number *n* corresponding to the transitions at low and high pH for the different sodium halides explored. The dashed line represents a non-cooperative system (*n* = 1).

To quantify cooperativity using equation 3, we determined the value of $\log(\alpha/(1-\alpha))$ from compiled experiments consisting of normalized $E_{2\omega}$ vs pH (Figure 2). The slope equal to *n* was measured for the linear region of the trace (where $1 \geq \log[\alpha/(1-\alpha)] \geq -1$).[55] The values of *n* for the MA and LA sites are listed in Table 1 and increase in the order *n*(NaCl) < *n*(NaBr) < *n*(NaI). For the more acidic silanol groups deprotonated below pH 7, we observed no cooperativity in the presence of NaCl (*n* ≈ 1), while the presence of NaBr and NaI led to cooperative numbers of ~ 2 and 3, respectively (Table 1). For the experiments performed at higher pH, NaI led to a cooperative number close to 1 (1.17(4)), yet NaBr and NaCl yielded *n* values of 0.62(1) and 0.55(1), respectively. Generally, these values indicated that the more acidic sites exhibited positive cooperativity (*n* > 1) and the less acidic sites exhibited negative cooperativity (*n* < 1).

The relationship between pK_a^{eff} and pK_a can be determined from n with the following phenomenological equation:[55]

$$pK_a^{eff} - pK_a = \Delta pK_a = \frac{\Delta G_{interaction}}{2.3RT}\left(1-\frac{1}{n}\right) = \pm 1.74\left(1-\frac{1}{n}\right). \qquad (3.4)$$

Here $\Delta G_{interaction}$ stems from interactions between neighboring sites and is usually on the order of 4RT.[55] Consequently, we can determine the intrinsic pK_a of the different sites according to:

$$pK_a = pK_a^{eff} - \Delta pK . \qquad (3.5)$$

Using equation 3.5, this intrinsic pK_a was calculated for the two types of acidic silanol groups (Table 3.1). For the more acidic silanol groups, the pK_a values were very similar yielding an average value of 4.2, ranging in value from 4.0 - 4.3, which indicated that the difference in the $pH_{0.5}$ and pK_a^{eff} observed for the different sodium halide solutions was due primarily to differences in cooperativity. In contrast, the pK_a values were not consistent for the different sodium halide salts for the less acidic surface sites as indicated by the large range of pK_a values (10.0 − 11.4). This disagreement with the cooperative model indicated that the intrinsic acidity of these LA surface sites was influenced by other factors in addition to cooperativity.

Table 3.1 Parameters for the More Acidic (MA) and Less Acidic (LA) Sites Based on the Cooperative Equilibrium Model.

Salt	More Acidic (MA) Sites			Less Acidic (LA) Sites		
	pK_a^{eff}	*n*	pK_a	pK_a^{eff}	*n*	pK_a
NaCl	4.06(4)	0.94(3)	4.0	8.6(1)	0.55(1)	10.0
NaBr	3.4(2)	2.0(3)	4.3	10.3(2)	0.62(1)	11.4
NaI	3.2(1)	2.9(2)	4.3	11.3(1)	1.17(4)	11.0
KCl	4.9(3)	0.99(3)	4.9	10.2(2)	0.50(1)	11.9
KBr	4.1(2)	2.1(1)	5.0	11.1(2)	0.75(4)	11.7
KI	3.4(2)	2.9(3)	4.5	11.5(2)	1.10(6)	11.3

3.2.4 Acid-Base Equilibria in the Presence of Potassium Halides

To test whether the presence of sodium was critical to the observed halide behavior, we performed similar experiments using potassium halides (Figure 3.3). The potassium halides yielded very similar trends in both the cooperative unit and the trend in pK_a values. Indeed, the cooperative numbers were within error for both the sodium and potassium salts of the like halide (Table 3.1). This similarity suggested that it was the identity of the halide and not the alkali ion that influenced the cooperative behavior. Alternatively it is possible that the sodium and potassium halides have similar ion pair structures that contribute to cooperativity with the larger anions. The intrinsic pK_a values, however, varied for the sodium and potassium salts. Our previous work comparing the behavior of alkali chlorides on the acid-base behavior of silica indicated that the affinity of the cation for the siloxide determined its apparent pK_a.[21] Based on the theory of

matching water affinities[61] often used to interpret specific ion effects, we concluded that sodium interacted most strongly with the siloxide sites followed by lithium, potassium, and cesium. The same trend is observed herein, where all of the sodium salts led to lower pK_a values than the corresponding potassium salts, which we attribute to the stronger affinity of sodium for the siloxide surface.
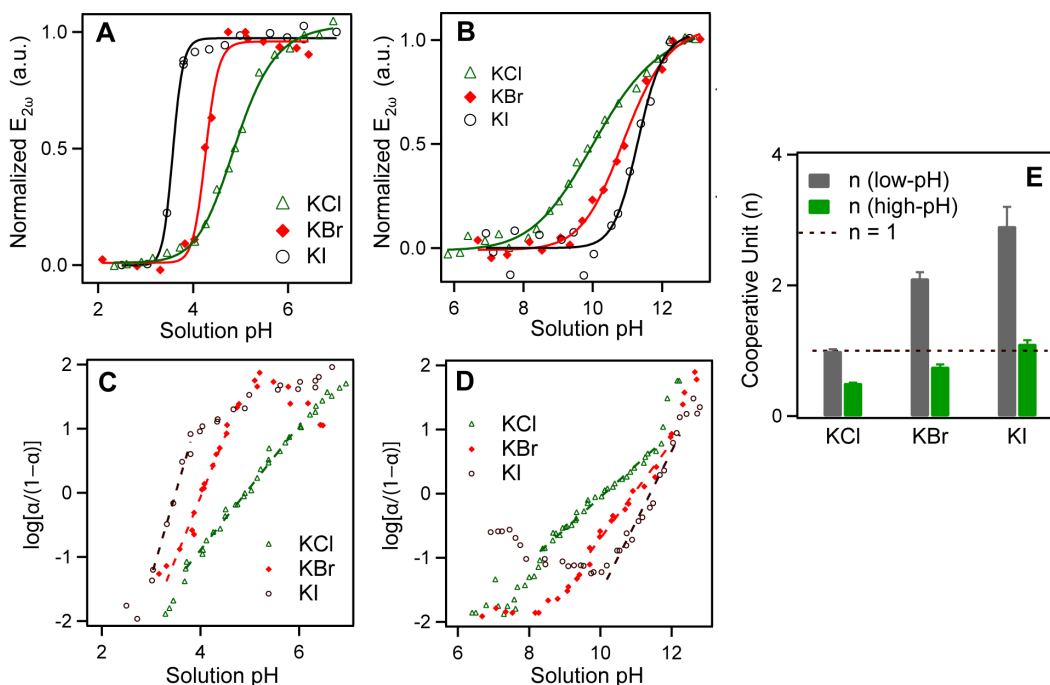
Figure 3.3 Representative titration curves for the (A) more acidic and (B) less acidic sites of the silica/water interface in the presence of different potassium halides. Log[α(1-α)] as a function of (C) low solution pH and (D) high solution pH for the silica/water interface with different potassium halide electrolytes. The dashed lines represent the fit to the linear portion of the trace (-1 < log[α(1-α)] < 1). (E) The n values for the more acidic and less acidic sites determined from the plots in C and D. The dashed line marks *n* = 1, which is the *n* value corresponding to a non-cooperative system.

3.2.5 Interpretation of the Trends in Cooperativity for the Silica/Halide

Electrolyte Interface

Both the potassium and sodium iodide systems exhibited positive cooperativity for the more acidic sites ($n = 0.94 – 2.9$) and negative cooperativity for the less acidic sites ($n = 0.55 – 1.17$) (Table 3.1). As shown in figure 3.4, the cooperative number for the MA sites is strongly correlated with both the size of the anion (based on the ionic area) and the free energy of hydration. The larger the anion and the smaller the energy of hydration, the more positively cooperative the system. This trend in n values suggests that the larger anions interacted with multiple silanol groups, which led to coupled acid-base behavior among neighbors (Scheme 3.2). This could in part be due to its larger ionic area that facilitated cooperative interactions (Figure 3.5A). Additionally, the ability of iodide in particular to become partially desolvated owing to its weak interactions with water makes it more favorable for it to partition to the interface, which has been used to explain its greater affinity for hydrophobic or neutral surfaces (Figure 3.5B).[37,41] At the negatively charged mineral oxide interface, we propose that a cooperative compact layer forms consisting of stabilizing clusters of siloxide-alkali complexes that are then capped with a iodide layer that favors surface interactions more so than those with bulk water (Scheme 2). The position of the water molecules in this compact layer is not known, although our previous work indicated that sodium and potassium may form a partially dehydrated ion pair with siloxide sites.[21]
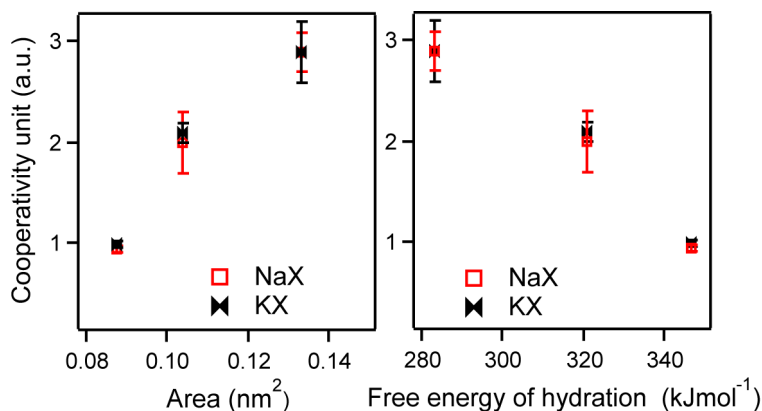
Figure 3.4 Cooperativity as a function of ionic area and free energy of hydration of the respective anions.

Scheme 3.2 Role of Ions in Positively and Negatively Cooperative Dissociation of More Acidic and Less Acidic Sites, Respectively.
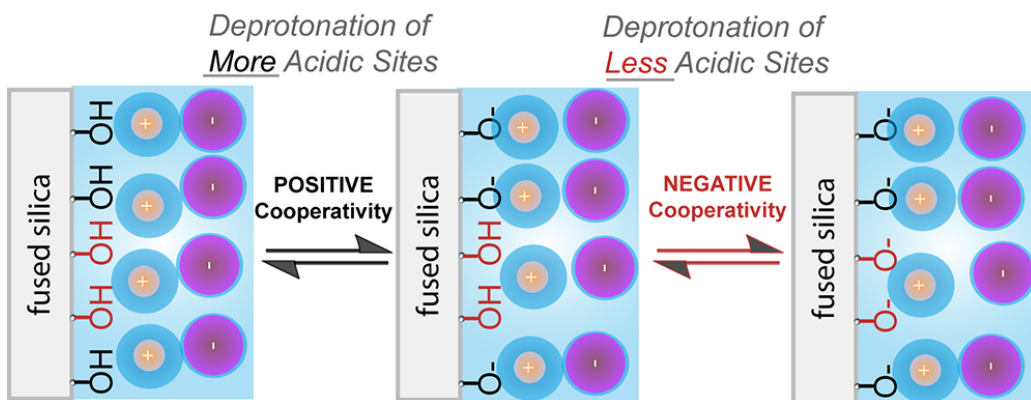
3.2.6 Effects of Halides on the Relative Population of the Two Acidic Silanol Sites

Thus far we have considered the behavior of the two different sites independently. As previously discussed, the different acidities of the sites have been correlated with different hydrogen bonding environments of the silanol groups. For example, one recent MD-DFT study indicated that the more acidic

96

sites donated hydrogen bonds to water, whereas the less acidic sites donated hydrogen bonds to neighboring silanols.[23] We reasoned that the presence of different ions could change the hydrogen bonding of the silanols and that of interfacial water, which in turn could influence the bimodal distribution of more and less acidic sites. The relative distribution of the two sites can be calculated from the normalized interfacial potential using the relative change in $E_{2\omega}$ at low and high pH as described in chapter 2. Thus, experiments at low and high pH were performed separately to avoid hysteresis in these systems and were combined by relating $E_{2\omega}$ to the average value at neutral pH (pH ~ 7) according to:

$$rE_{2\omega} = \frac{E_{2\omega}}{E_{2\omega}(pH\ 7)}.$$

(3.6)

The normalized interfacial potential (N-Φ_0) was then determined by compiling multiple high and low-pH experiments according to:

$$\text{N-}\Phi_0 = \frac{rE_{2\omega} - rE_{2\omega}(pH\ 2)}{rE_{2\omega}(pH\ 12) - rE_{2\omega}(pH\ 2)}.$$

(3.7)

The compiled data consisting of all possible combinations of low and high pH data sets were smoothed and then used to determine N-Φ_0 as a function of pH as depicted in figure 3.5A and B (5 point box smoothing function). To ensure that our method for combining the low and high pH data was reasonable, we compared the N-Φ_0 values with the $E_{2\omega}$ of the electrolyte interface at neutral pH referenced to that of Millipore water, which represented a common starting point for every experiment. There is a general correlation between the $E_{2\omega}$ referenced to water and the trend in N-Φ_0 values, indicating that the presence of the ions does lead to

97

a different extent of deprotonation at neutral pH, and accordingly a change in bimodal distribution (Figure 3.5).

Figure 3.5 illustrates the change in interfacial potential over the entire pH range studied. If we once again consider the constant capacitance model, then the normalized interfacial potential (N-Φ_0) should directly reflect the fraction deprotonated of the surface as a function of pH. Consequently, the percent deprotonated at neutral pH (%$_{pH7}$), or N-Φ_0 x 100%, is equivalent to the percentage of more acidic sites (MA%), as this pH lies between the two deprotonation equilibria. For the silica/water interface in the presence of the NaCl electrolyte, the corresponding MA% was 20(2)% (Figure 3.6A). In contrast, for the interface in the presence of NaBr electrolyte the MA% increased to 63(6)%. The trend continued, with the NaI system exhibiting the greatest percentage of more acidic sites of 86(1)%. A very similar trend was observed for the potassium halides as well (Figure 3.5B). Consequently, we infer that the silica surface at neutral pH can possess drastically different surface charge densities depending on the halide present. Significant differences in MA% were also observed for the various alkali chlorides (from 20-60%),[21] but the trends for the halide series were even more substantial. Additionally, for the alkali chloride series the MA% values increased with a decrease in the free energy of cation hydration with the exception of lithium.[21] Similarly, we observe that MA% increased as the free energy of hydration decreased for the halides (Figure 3.5). This observation supports that the ions that do not favor strong interactions with water are able to

influence the hydrogen-bonding structure at the interface in a way that prefers the

formation of MA over LA sites.
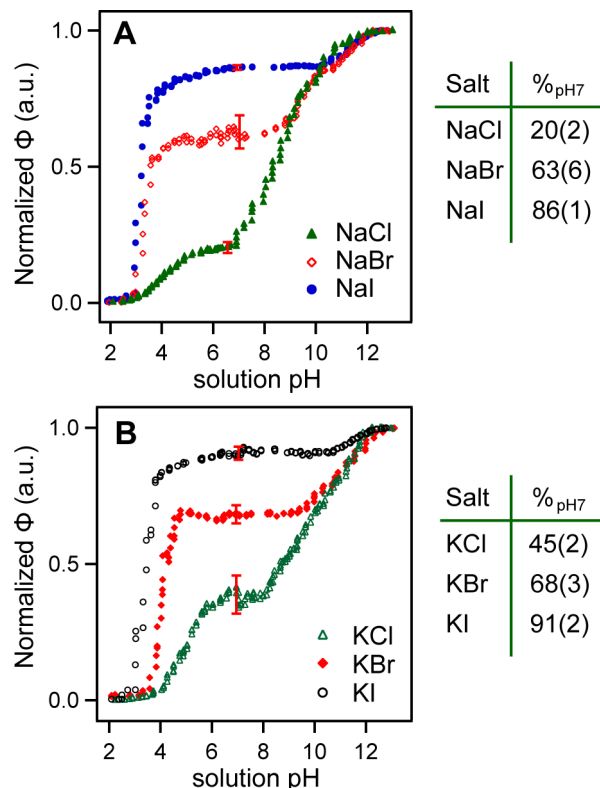
Figure 3.5 Normalized Φ, which is proportional to the relative surface charge density, as a function of pH in the presence of (A) sodium halides and (B) potassium halides. The tables represent the relative distribution of the two acidic sites at these silica/halide interfaces as the percent deprotonated at pH 7 (%$_{pH7}$), which is equivalent to the percentage of more acidic sites.

The differences in N-Φ_0 values for the different electrolytes also shed light

on why the cooperative model failed to account for the intrinsic differences in

surface acidity of the LA sites shown by the pK_a values (Table 3.1). Now we see

that the pK_a^{eff} values for the less acidic sites are directly correlated with how

charged the surface is at pH 7, when essentially all of the LA sites are still

protonated. For example, in the presence of NaCl electrolyte only 20% of the surface sites were deprotonated at pH 7.   Consequently, the pK_a^{eff} of the remaining LA sites was the lowest (8.6(1)), meaning they were the most acidic, or easily deprotonated. For the NaBr, the amount of surface charges was 63(6)% at pH 7, leading to a pK_a^{eff} for the remaining LA sites of 10.3(2). The NaI exhibited both the greatest amount of surface charges at neutral pH (86(1)%) and the highest pK_a^{eff} value (11.3(1)).   These results reveal that the greater the initial charge of the interface, the more difficult the deprotonation of the remaining LA sites owing to charge repulsion with the high density of siloxides already present.

The different extent of surface charging at neutral pH also accounts for the trend in n values for the LA sites. For the interface in the presence of NaCl, the remaining LA sites represented 80% of the surface sites. Consequently, there were many LA sites that neighbored one another. The close arrangement of the protonated sites led to negative cooperativity ($n = 0.52$), where the deprotonation of one site increased the energetic penalty for deprotonation of the neighbor. Similarly, the NaBr electrolyte/silica interface exhibited negative cooperativity for the LA sites that made up 40% of the surface, but to a lesser extent than the NaCl system, given the lower density of LA sites. For the NaI electrolyte interface, however, the density of LA sites was so low that there were essentially no neighboring LA sites. Therefore, the deprotonation of these LA sites occurred in a non-cooperative manner with no nearest neighbor interactions ($n \sim 1$). We reason that these sites exhibit charge repulsion unlike the MA sites because of the

structure of the compact Stern layer that can not further compensate for the increase in lateral repulsion with increasing surface deprotonation.

3.2.7 Relative SHG E-field from Silica/Water and Silica/Halide Electrolyte Interfaces

The difference in percent of deprotonation at pH 7 values suggested that the presence of bromide or iodide ions makes the silica/electrolyte interface more acidic leading to a more charged surface at neutral pH by promoting surface deprotonation. To test this we compared the percent deprotonated values of the different silica/electrolyte interfaces at neutral pH ($\%_{pH7}$), determined from the normalized interfacial potential (N-Φ_0), with the $E_{2\omega}$ values at neutral pH referenced to $E_{2\omega}$ from the silica/Millipore water interface that was measured prior to the addition of electrolyte. This referencing method represents a common starting point for all experiments, as the first step is always alignment of the sample on Millipore water. Specifically, this referenced $E_{2\omega}$ was determined from:

$$\text{Referenced } E_{2\omega} = \frac{E_{2\omega}(0.5\text{-M Electrolyte})_{pH7}}{E_{2\omega}(\text{Millipore Water})}$$

$$(3.8)$$

Figure 3.7 shows that the $E_{2\omega}$ increased when we replaced water with bromide and iodide solutions and decreased when replaced with chloride salt. These observations yet again support that the presence of bromide and iodide salts increased the population of acidic silanol sites on silica and thus increased the surface charge density at neutral pH.
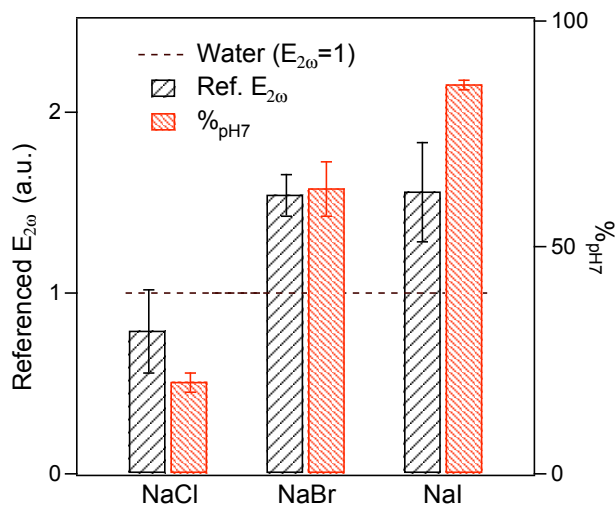
Figure 3.6 $E_{2\omega}$ referenced to the SH E-field of water and the % deprotonation at neutral pH ($\%_{pH7}$) as a function of sodium halide. The values in the bar graph represent the average of at least four measurements and the errors represent the standard deviation.

3.2.8 Interfacial Potential as a Function of Surface pH

As discussed in 3.2.3 we considered the change in SHG E-field or the change in interfacial potential as a function of the solution pH instead of the surface pH to calculate the intrinsic pK_a, and other thermodynamic parameters. As the surface pH depends on the absolute interfacial potential many models, however, utilize the surface pH rather than the solution pH to calculate pK_a values. The relation between the surface hydronium concentration, $[H_3O^+]_s$, and the bulk hydronium concentration, $[H_3O^+]_b$, can be expressed by the following equation:

$$[H_3O^+]_s = [H_3O^+]_b \exp[-e\Phi(0)/kT] \tag{3.9}$$

102

where $\Phi(0)$ is the interfacial potential at a particular pH, k is the Boltzman constant and T is the temperature in Kelvin. After taking the logarithm and multiplying by -1, the equation yields:

$$pH_s = pH_b + \frac{e\Phi(0)}{2.303kT}$$
(3.10)

Accordingly if we know the interfacial potential at a particular bulk pH, we can calculate the corresponding pH of the silica/water interface. The maximum interfacial potential at high pH values (pH $\geq$ 12.5), $\Phi(0)_{max}$, was reported to be 140 mV for silica/0.5-M NaCl$_{(aq)}$ interface as measured by Eisenthal and coworkers.[1] To measure the interfacial potential at all other pH values, we used the relationship:

$$\Phi(0) = (N\text{-}\Phi_0) \times \Phi(0)_{max}$$
(3.11)

where N-Φ_0 is the normalized interfacial potential determined from combining experiments at both low and high pH as described in the section 3.2.6.

The calculated Φ_0 values were used to determine the surface pH. A comparison of Φ_0 vs. the surface and solution pH is shown in Figure 3.7. As shown the sharp increase in potential leads to a deviation from sigmoidicity for the Φ_0 vs. solution pH trace, which prevents us from using it to find the pH$_{0.5}$ or pK$_a$.
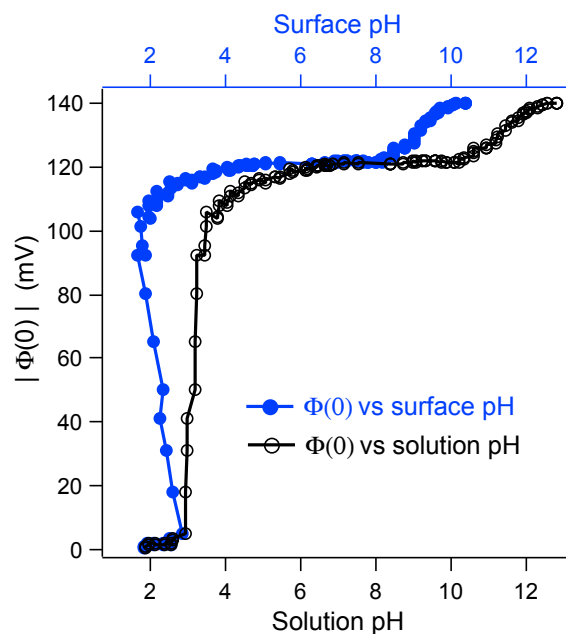
Figure 3.7 Interfacial potential, $\Phi(0)$, as a function of solution pH (black trace) and surface pH (blue trace).

3.2.9 Effect of Anion Concentration on Acid-Base Equilibria

The concentration of cations in the aqueous phase was found to be an important factor as described in chapter 2 of this thesis. For cations we observed that lowering the concentration of alkali ions from 0.5 M to 0.1 M basically reduced the specific ion effects on the acid-base behavior of the silica/water interface. To test the influence of concentration on the specific halide effects, we performed acid-base titrations of the silica/electrolyte interface in the presence of 0.1-M chloride and iodide electrolytes and compared the observed thermodynamic parameters with those from the 0.5-M experiments (Figure 3.1). As shown in Figures 3.9, the pK_a^{eff} values and cooperative numbers, *n,* remained essentially unchanged for the NaI electrolyte system at 0.5 M and 0.1 M. These observations importantly indicate that 0.1 M iodide was adequate to induce cooperative acid-

base equilibria at the silica/water interface (Figure 3.9, Table 3.2). This finding was also true for the concentration effect of KI on the titration of more acidic sites, for which yet again the pK_a^{eff} and n values were independent of KI concentration (Figure 3.10, Table 3.2). However, both the pK_a^{eff} and n values were found responsive to the KI concentration for the LA silanol groups on silica.

Lowering the electrolyte concentration from 0.5 M to 0.1 M decreased the pK_a^{eff} value from 11.5(2) to 10.3(4), and n value from 1.10(6) to 0.66(4) for the titrations of the LA sites of silica/KI$_{(aq)}$ interface. We attributed this trend in n values for the LA sites to the extent of surface charging at neutral pH as explained in section 3.2.7 of this chapter. According to our cooperativity model, at lower surface charge density the closure proximity of the silanol sites disfavor the deprotonation process, leading to negative cooperativity. The percentage of deprotonated sites at silica/KI$_{(aq)}$ interfaces decreases from 91(2)% to 77(7)% (Inset Table of Figure 3.10) (i.e., greater amount of protonated silanol groups at lower KI electrolyte concentration) with the decrease of concentration resulting in lower cooperative number.
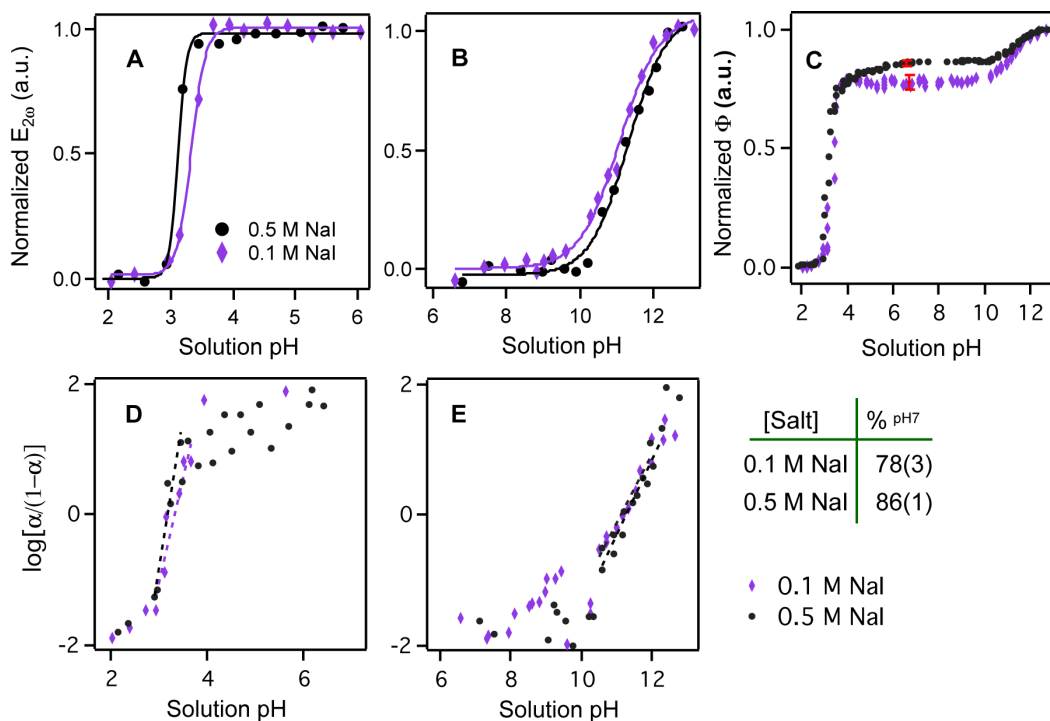
Figure 3.8 Representative titration curves for the (A) more acidic and (B) less acidic sites of the silica/water interface in the presence of 0.1 M and 0.5 M NaI. The solid lines represent the sigmoid fitting to the titration data. (C) Normalized Φ (proportional to the relative surface charge density) as a function of pH in the presence of sodium halides. The table represents the relative distribution of the two acidic sites at these silica/halide interfaces, as the percent deprotonated at pH 7 ($\%_{pH7}$) is equivalent to the percentage of more acidic sites. Log[α(1-α)] as a function of (D) low solution pH and (E) high solution pH for the silica/water interface with different concentration of NaI electrolytes. The dashed lines represent the fit to the linear portion of the trace ($-1 < \log[\alpha(1-\alpha)] < 1$).
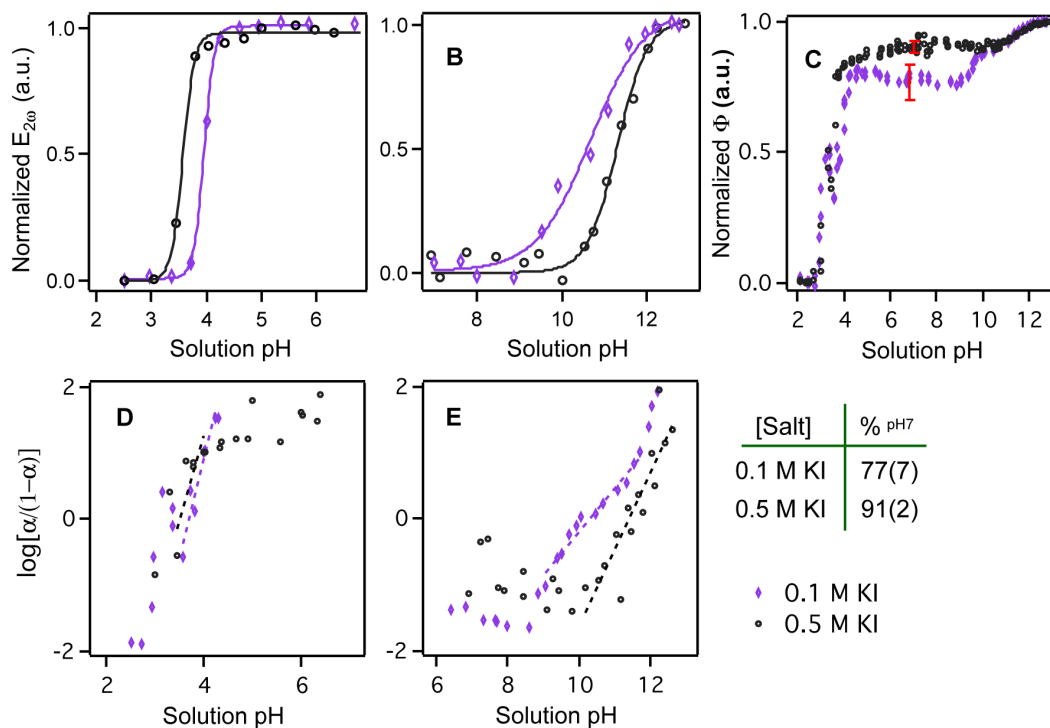
Figure 3.9 Representative titration curves for the (A) more acidic and (B) less acidic sites of the silica/water interface in the presence of 0.1 M and 0.5 M KI. The solid lines represent the sigmoid fit to the titration data. (C) Normalized Φ as a function of solution pH in the presence of potassium halides. The table represents the percent deprotonated at pH 7 (%$_{pH7}$), which is equivalent to the percentage of more acidic sites. Log[α(1-α)] as a function of (D) low solution pH and (E) high solution pH for the silica/water interface with variable concentration of KI electrolytes. The dashed lines represent the fit to the linear portion of the trace (-1 < log[α(1-α)] < 1).

Interestingly, decreasing the iodide concentration changed the cooperative number, *n*, in such a way that the value of the intrinsic pK$_a$ remained unchanged within ±0.1 (Table 3.2), which provides for the evidence that the cooperative model accurately describes these processes. Our calculation of pK$_a$ for both MA and LA sites from equation 3.4 and 3.5 using *n* values gave very small range of pK$_a$ (4.3 − 4.8 for MA and 11.0 − 11.9 for LA sites) for all different salts except

NaCl that gave pK_a 3.9 – 4.0 and 10.0 – 10.1 for MA and LA, respectively, representing NaCl salt as the outlier of the series.

Table 3.2 Parameters for the More Acidic (MA) and Less Acidic (LA) Sites at Different Concentration of Salts Based on the Cooperative Equilibrium Model.

Salt	Conc. (M)	More Acidic (MA) Sites			Less Acidic (LA) Sites		
		pK_a^{eff}	n	pK_a	pK_a^{eff}	n	pK_a
NaCl	0.1	4.5(3)	0.75(3)	3.9	9.6(1)	0.76(5)	10.1
	0.5	4.06(4)	0.94(3)	4.0	8.6(1)	0.55(1)	10.0
NaI	0.1	3.36(3)	3.2(6)	4.5	11.2(1)	1.11(8)	11.0
	0.5	3.2(1)	2.9(2)	4.3	11.3(1)	1.17(4)	11.0
KCl	0.1	4.9(1)	1.06(2)	4.8	8.9(3)	0.44(2)	11.1
	0.5	4.9(3)	0.99(3)	4.9	10.2(2)	0.50(1)	11.9
KI	0.1	3.6(4)	3.0(5)	4.8	10.3(4)	0.66(4)	11.2
	0.5	3.4(2)	2.9(3)	4.5	11.5(2)	1.10(6)	11.3

3.2.10 Vibrational Sum Frequency Generation Spectra of Water at The Interface

Vibrational sum frequency generation (SFG) is a complementary nonlinear optical technique that can be used to directly probe changes in the amount of ordered water at the interface. Regarding the silica/electrolyte interface, the groups of Shen[13] and Hore[16,17] have found that adding sodium chloride electrolytes to the silica/water interface systematically decreased the SFG signal intensity. This decrease was attributed to screening of interfacial charges in the diffuse and compact double layer, which led to a decrease in the amount of

ordered water molecules. Specifically, Hore and colleagues found that the SFG intensity decreased by a factor of ~3 for the silica/ 0.5-M NaCl interface compared with the silica/water interface, when both were at neutral pH.[17] In related studies, Chou and co-workers[18] and Cremer and co-workers[62] explored how the identity of the alkali ion influenced the resulting water structure and found that the amount of ordered water did vary slightly depending on the nature of the cation at low salt concentrations (0.1 mM for pH 10[62] and 1 mM for neutral pH).[18]   More recently, specific anion effects were investigated at the silica/electrolyte interface at pH 10 with very low electrolyte concentrations (0.1 mM). The addition of salt led to a slight decrease in signal. The NaBr did, however, exhibit slightly more signal at this pH and concentration than NaCl, which they attributed to bromide partitioning to the interface, which added to the negative interfacial potential of the charged silica surface.[39] In contrast, the addition of 1.0 M sodium iodide or bromide to a neutral Langmuir-Blodgett film of polyacrylamide at the air interface led to a significant increase in SFG intensity indicative of more ordered water.[37] The authors concluded that the ability of the larger halides to bind to these neutral interfaces led to an increase in the interfacial charge density, which accordingly led to an increase in the amount of aligned water. A significant increase was also observed upon adding 2.0 M sodium iodide to the air/water interface.[63]

To determine whether the addition of 0.5-M iodide led to a decrease or increase in ordered water at the negatively charged silica/water interface, we monitored the resonantly enhanced vibrational sum frequency generation (SFG)

signal in the absence and presence of NaI electrolyte. In these experiments, two

electric fields were incident on the interface, one in the visible and the other in the

infrared (Figure 3.11A). When the IR frequency is in resonance with vibrational

modes associated with ordered molecules at the interface, the second-order

susceptibility $\chi^{(2)}$ becomes large, leading to an increase in the electric field at the

sum of the two incident frequencies (E_{SF}). As in SHG, within the electric dipole

approximation the second-order susceptibility $\chi^{(2)}$ is only non-zero for

noncentrosymmetric environments. Consequently, only ordered water molecules

contribute to the resonantly enhanced part of the $\chi^{(2)}$ term:

$$E_{SF} \propto P_{SF} = \chi^{(2)}E_{Vis}E_{IR} + \chi^{(3)}E_{Vis}E_{IR}\Phi_0 \qquad (3.12)$$

In these SFG experiments, we utilized an fs IR pulse that is broad in the

frequency domain and a ps visible pulse that is narrow in the frequency domain.

This common strategy for broadband SFG allows multiple resonant frequencies to

be probed simultaneously, decreasing the amount of time required to capture a

SFG spectrum.[64]

Figure 3.10B illustrates the SFG spectra of the silica/water interface at

neutral pH in the presence and absence of 0.5 M NaI. The addition of sodium

iodide led to a substantial decrease in SFG signal (~40 fold), much more so than

that observed for sodium chloride (~3 fold) although in those studies a different

polarization combination was used than for our experiments (ssp), so the changes

in signal can not be directly compared. The observed 40-fold decrease in SFG

signal upon adding sodium iodide was also in stark contrast to the SHG

experiments, where we saw on average a 2.5-fold *increase* in SHG intensity upon

changing the aqueous solution from Millipore water to 0.5-M NaI at neutral pH. This difference in signal suggests that non-resonant SHG and resonantly enhanced SFG are sensitive to different properties of the interface, which will be discussed in greater detail below. Finally, the significant decrease in the amount of ordered water in the presence of iodide at the negatively charged interface is very different than the trends observed for iodide interacting with the air/water[63] and neutral air/polymer[37] and protein interfaces.[36] For these neutral interfaces, it is reasoned that iodide partitioning leads to an increase in interfacial potential and consequently the amount of ordered water.[37] In our experiments, sodium iodide decreased the signal through a combination of screening and the displacement or disordering of interfacial water, which is consistent with the formation of a compact cooperative Stern layer that has less ordered water molecules.

Regarding the different observations for the SFG and SHG experiments, in the case of resonantly enhanced SFG at high electrolyte concentrations (> 0.1 M), the resonant $\chi^{(2)}$ term associated with the aligned, oriented water in the compact Stern layer contributes more to the signal than the $\chi^{(3)}\Phi_0$ term, which is diminished by the short Debye length and corresponding decrease in penetration depth of the static electric field arising from the charged surface.[17] To determine whether the amount of aligned, oriented water molecules in the compact Stern layer was affected by pH at these high NaI concentrations, we varied the pH from neutral to high pH and from neutral to low pH while maintaining the same electrolyte concentration as was done in the SHG titration experiments. The
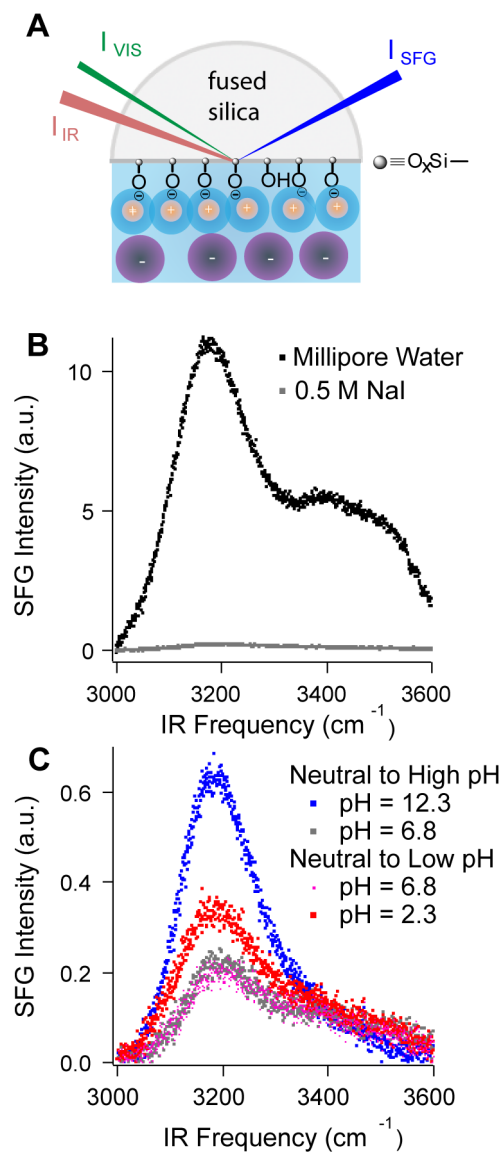
Figure 3.10 (A) Schematic illustrating sum frequency generation at the silica/aqueous interface. I_{VIS} and I_{IR} are the incident visible and infrared light intensities from the tunable laser assembly. I_{SFG} is the intensity of the sum frequency signal. (B) Vibrational SFG spectra of the silica/Millipore water interface (black trace) and the silica/0.5-M NaI electrolyte interface (gray trace) at neutral pH. (C) Vibrational SFG spectra of the silica/0.5-M NaI electrolyte interface at different pH. The spectrum at neutral pH was measured on a fresh sample (gray and pink traces) before adjusting the electrolyte to high or low pH (blue and red, respectively). The ppp-polarization combination was used to monitor the amount of ordered water.[65]

from neutral to high pH, for the SFG spectra the signal intensity increased at both high *and low* pH compared with that at neutral pH. These results indicated that the amount (or net orientation) of ordered interfacial water within the compact Stern layer did vary with pH. As discussed previously, the presence of NaI led to the formation of a cooperative structure between the surface, cations, and anions that stabilized the dissociated MA sites and the protonated LA sites (Scheme 3.2). We reason that this cooperative structure present at neutral pH displaced more interfacial water molecules than the Stern layer present at low or high pH. Consequently, the SFG intensity, which is proportional to the amount of aligned water, was lowest at neutral pH.

We also note that the peak in the SFG spectra at ~3200 cm^{-1} associated with high-coordinate water dominated at all pH conditions and was particularly enhanced at high pH. A very similar trend in the shape of the SFG spectra was observed for the silica/electrolyte interface under different pH conditions in the presence of 0.1-0.5 M NaCl.[13] The small contribution of signal at 3400 cm^{-1}, which is associated with low-coordinate water, suggested that high salt concentrations particularly perturb the weakly coordinated water. Interestingly lower alkali chloride salt concentrations have been found to diminish the peak at 3200 cm^{-1} more so than that at 3400 cm^{-1}.[18] Future work will examine the affect of lower iodide salt concentrations on the SFG spectrum at the silica/electrolyte interface.

Finally, the very different trends in signal intensity for resonantly enhanced SFG, where $\chi^{(2)}$ dominates, and non-resonant SHG, where $\chi^{(3)}\Phi_0$ should

results are shown in Figure 3.10C. Unlike the trend observed by SHG, where the

SHG signal exhibited a large decrease from neutral to low pH and a small increase

dominate, support that the changes in signal observed by SHG indeed stem from

the $\chi^{(3)}\Phi_0$ term. This is important for our analysis as it allows us to relate all

changes in signal to Φ_0. Moreover, it lends further support to the first reports on

the $\chi^{(3)}$ technique, which indicated that the non-resonant $\chi^{(2)}$ represented in

equation 2, which also stems from the ordered, oriented water molecules, is much

smaller than $\chi^{(3)}\Phi_0$, and therefore can be considered to remain invariant with

changing pH. One question that might arise is whether iodide directly contributes

to the interfacial potential instead of increasing the magnitude of the potential by

facilitating deprotonation of the surface. Previous work has indicated that iodide

interacts more strongly with neutral rather than charged interfaces, which should

lead to the greatest amount of iodide binding near the point of zero charge (pH 2).

Yet, upon adding sodium iodide to the interface at low pH near the point of zero

charge, we did not observe signal enhancement (data not shown).   In contrast

adding sodium iodide to the silica/water interface at neutral pH led to a ~2.5-fold

signal increase (or an increase in $E_{2\omega}$ of ~1.6 (Figure 3.6)), which is consistent

with our interpretation that iodide changes the interfacial potential by promoting

surface deprotonation rather than directly contributing to the amount of negative

charge at the interface.

3.3 Concluding Remarks

We have observed that sodium and potassium halides exhibit pronounced specific ion effects on the acid-base chemistry of the mineral oxide interface. The large influence of the halide is remarkable given the net negative charge on silica at all pH values explored in this study (point of zero charge = 2-3). This work suggests that the larger halides formed structures at the interface that facilitated positive cooperativity between neighboring silanol groups for the more acidic sites. Moreover, the larger, more polarizable halides also led to a significant shift in the bimodal distribution of silanol sites, such that the more acidic sites dominated. Consequently, the interfacial potential (and the corresponding surface charge density) at neutral pH increased significantly as the halide was varied from chloride to bromide to iodide. Finally, these experiments indicate that the influence of the halide must also be considered over a wide pH range to accurately model the surface charge density of negatively charged surfaces, which has major ramifications for modeling pollutant transport, weathering and other environmental processes.[2,3]

3.4 Experimental Section

3.4.1 Laser System and SHG Assembly

A detailed description of the laser system used in these experiments can be found in chapter 2 of this thesis. Briefly, the system consists of a femtosecond Ti:Sapphire oscillator (Spectra Physics, Mai Tai, 80 MHz) and a Nd:YLF laser (Spectra Physics, Empower) used to seed and pump, respectively, a regeneratively amplified laser (Spitfire Pro, Spectra Physics, 1 kHz, 100 fs, 3.3

W). One third of the Spitfire output is used to pump an optical parametric amplifier (Spectra Physics OPA-800CF). The output from the OPA (tuned to 550 ± 2 nm) was then attenuated to 0.4 ± 0.1 mJ by a neutral-density filter (New Focus, cat. # 5215), and directed through a half-wave plate and polarizer for s-polarization selection. The polarized light was focused onto the fused silica/water interface at an angle of 62° from surface normal near total internal reflection. The reflected second harmonic light generated at the interface was then passed through a color glass filter (Thorlabs) to remove the reflected fundamental light and focused onto a monochromator (Optometrics Corp., Mini-Chrom MC1-02) tuned to the second harmonic wavelength (275 nm). SHG was detected by a photomultiplier tube (PMT, Hamamatsu Photonics), and the electric response from the PMT was then amplified and counted with a gated photon counter (Stanford Research Systems). Before performing each experiment, the quadratic power dependence and SHG wavelength dependence were verified to ensure no optical damage was occurring at the interface.[9]

For all SHG measurements a freshly cleaned fused silica hemisphere (ISP optics, 1 inch diameter, QU-HS-25, UV-grade SiO_2) was placed on a custom-built Teflon cell so that the flat surface of the hemisphere was in contact with the aqueous phase. The silica/water interface was perpendicular to the surface of the laser table, and the aqueous phase was exposed so the pH could be routinely changed and monitored from the top.[21]

3.4.2 Broadband Vibrational Sum Frequency Generation Experiments

Two-thirds of the output of the Spitfire Pro regeneratively amplified system described above (2.2 W) was also used to pump a TOPAS-C/NDFG optical parametric amplifier (Light Conversion). The resulting broadband infrared light was tuned from 3000-3600 cm^{-1} to probe resonances of the O-H stretch of water at the interface. Visible light from the Spitfire (100 fs, l = 800 nm) was broadened to a ps pulse using a Fabry-perot etalon (FWHM ~ 10 cm^{-1}). The p-polarized fs IR light (~10-12 mJ/pulse) and the p-polarized ps visible light (~10 mJ /pulse) were focused through a fused silica hemisphere (ISP optics, 1 inch diameter, IR-grade SiO_2), enclosed in the same type of sample cell holder as the SHG set-up, onto the silica/water interface at angles of 66° and 64°, respectively, from surface normal. After spatially and temporally aligning the two fields, the sum frequency light emanating from the sample was recollimated, filtered with a bandpass filter to remove residual 800-nm light (Chroma, HQ 617/70 M), passed through a polarizer to select the p-polarized SFG, and focused onto a spectrograph (Acton SP-2556 Imaging Spectrograph, grating: 1800 G/mm with 500-nm blaze wavelength) connected to a thermoelectrically cooled, back-illuminated, charge coupled device camera (Acton PIXIS 100B CCD digital camera system, 1340 x 100 pixels, 20 mm x 20 mm pixel size, Princeton Instruments). The ppp-polarization combination was selected as it is particularly sensitive to the amount of ordered interfacial water molecules.[65] Before performing an experiment, reference spectra were first collected using the same configuration with a gold-coated silica hemisphere with the IR centered at 3160 cm^{-1}, 3280 cm^{-1}, 3390 cm^{-1}

and 3500 cm^{-1}. Spectra at the same central wavelengths were measured for the silica/water interface. The spectra from the silica/water interface were normalized by summing the spectra and dividing this summed spectrum by the sum of the gold reference spectra following previous reports.[66]

3.4.3 Surface Preparation

The silica hemisphere was cleaned prior to use by sonicating it in Millipore water followed by methanol and then in water again. The flat surface of the hemisphere was covered with a few drops of freshly prepared commercial glass cleaner Nochromix (Godax Laboratories, 5% w/v solution in H_2SO_4) for 1 hour followed by copious rinsing in Millipore water. Next, the hemisphere was rinsed thoroughly with Millipore water followed by sonication in water (5 minutes × 2), in methanol (5 minutes) and then in water again (5 minutes). After the hemisphere was allowed to dry in an oven at 100 °C for 10 minutes, it was cooled down to room temperature and then plasma cleaned (Plasma cleaner, PDC-32G, Harrick Plasma) in air for 2-3 minutes.

3.4.4 Materials

Potassium bromide was purchased from Sigma-Aldrich. Sodium chloride (≥ 99%), and sodium hydroxide (≥ 97%) were purchased from EMD Chemicals Inc. Potassium chloride (≥ 99%) and potassium iodide (> 99%) were purchased from Analchemia Canada Inc. Sodium iodide (> 99.5%), potassium hydroxide (≥ 85%), sulfuric acid and hydrochloric acid were obtained from Caledon Laboratory

chemicals. Sodium bromide (> 99.5%) was purchased from Fisher Chemical. All compounds were used without further purification. Ultrapure deionized (18.2 MΩ·cm) water was used shortly after deionization by a MilliQ-Plus ultrapure water purification system (Millipore). The pH of all the solutions was measured with an Orion 2 star pH meter from Thermo Scientific using a double-junction Ag/AgCl electrode (Orion, 9107APMD). All experiments were performed with freshly prepared salt solutions.

3.4.5 SHG pH Variation Experiments

Prior to the start of an experiment, each sample was exposed to Milli-Q water until the SHG signal was optimized. As reported in our previously published paper,[21] separate experiments were performed for the lower and higher pH regions on different fresh samples to avoid any hysteresis.[51] Next, the water in the sample cell was completely replaced by ~10 mL of the salt solution of interest that had been pH adjusted to 7 for the low-pH experiments or not pH adjusted for the high pH experiments. This silica/electrolyte interface was allowed to equilibrate for 30 min while monitoring the SHG signal. After this equilibration time, aliquots of the corresponding acid or base solution with the same salt concentration (0.5 M) were added to adjust the pH by approximately 0.3 pH units. At each new pH, the system was allowed to stand for ~3 min to reach equilibrium, then SHG was collected for ~2 min. This step of changing the pH and measuring the corresponding SHG signal was repeated until the pH of the solution reached 12.5 for the high pH titrations and reached 2 for the low pH titrations. The

normalized $E_{2\omega}$ was determined from $I_{2\omega}$ as described in our previous work.[21] The plot of normalized $E_{2\omega}$ versus solution pH was then fit with a sigmoid function. The inflection point determined by the fit is the $pH_{0.5}$ value equivalent to the pK_a^{eff} according to the cooperative model. The listed pK_a^{eff} values and the error represent the average of values determined from two or more experiments and the measured range of values, respectively. The cooperative number n was determined by fitting *log[α(1-α)]* versus pH from $-1 <$ *log[α(1-α)]* < 1 with a line of best fit, where *log[α(1-α)]* $= n$pH $-n$pK$_a^{eff}$. All of the data for duplicate experiments were first compiled then plotted to find n. The reported value is from the fit of the compiled data and the error is the standard deviation reported from the fit.

3.4.6 SFG pH Variation Experiments

The SFG experiments were similarly conducted. First, SFG was measured for the silica/water interface without pH adjustment. The solution was then removed, and a 0.5 M NaI solution was added that had not been pH adjusted followed by monitoring of the SFG response. Next, a concentrated solution of NaOH (0.5 M NaI) was added dropwise to the aqueous phase until the desired basic pH was reached. SFG was once again measured. The low pH experiments were performed in a similar manner on a different sample beginning with Millipore water. To illustrate the reproducibility in signal shape and intensity, we included both of the spectra at neutral pH (0.5 M NaI) that corresponded to the experiments at high and low pH. Each experiment was performed in duplicate to

confirm the trends in SFG intensity change, and one representative set of data is

shown in Figure 3.10.

3.5 References

(1)   Sposito, G. *The Surface Chemistry of Soils*; Oxford University Press, 1984.

(2)   Stumm, W.; Morgan, J. J. *Aquatic Chemistry: Chemical Equilibria and Rates in Natural Waters; Third Edition*; Wiley, 1995.

(3)   Langmuir, D. *Aqueous Environmental Geochemistry*; Prentice Hall, 1997.

(4)   Iler, R. K. *Chemistry of Silica - Solubility, Polymerization, Colloid and Surface Properties and Biochemistry*; John Wiley & Sons, 1979.

(5)   Dove, P. M.; Rimstidt, J. D. In *Reviews in Mineralogy Series: The Silica Polymorphs*; Heaney, P., Prewitt, C., Gibbs, G., Eds.; Mineralogical Society of America: 1994; Vol. 29, p 259.

(6)   Sahai, N. *Environ. Sci. Technol* **2002**, *36*, 445.

(7)   Liu, D.; Ma, G.; Allen, H. C. *Environ. Sci. Technol.* **2005**, *39*, 2025.

(8)   Corn, R. M.; Higgins, D. A. *Chem. Rev.* **1994**, *94*, 107.

(9)   Eisenthal, K. B. *Chem. Rev.* **1996**, *96*, 1343.

(10)   Gopalakrishnan, S.; Liu, D.; Allen, H. C.; Kuo, M.; Shultz, M. J. *Chem. Rev.* **2006**, *106*, 1155.

(11)   Schr̈odle, S.; Richmond, G. L. *J. Phys. D: Appl. Phys.* **2008**, *41*.

(12)   Verreault, D.; Hua, W.; Allen, H. C. *J. Phys. Chem. Lett.* **2012**, *3*, 3012.

(13)   Du, Q.; Freysz, E.; Shen, Y. *Phys. Rev. Lett.* **1994**, *72*, 238.

(14)   Li, I.; Bandara, J.; Shultz, M. J. *Langmuir* **2004**, *20*, 10474.

(15)   Ostroverkhov, V.; Waychunas, G.; Shen, Y. *Phys. Rev. Lett.* **2005**, *94*.

(16)   Jena, K. C.; Hore, D. K. *J. Phys. Chem. C* **2009**, *113*, 15364.

(17) Jena, K. C.; Covert, P. A.; Hore, D. K. *J. Phys. Chem. Lett.* **2011**, *2*, 1056.

(18) Yang, Z.; Li, Q.; Chou, K. C. *J. Phys. Chem. C* **2009**, *113*, 8201.

(19) Ong, S.; Zhao, X.; Eisenthal, K. B. *Chem. Phys. Lett.* **1992**, *191*, 327.

(20) Zhao, X.; Ong, S.; Wang, H.; Eisenthal, K. B. *Chem. Phys. Lett.* **1993**, *214*, 203.

(21) Azam, M. S.; Weeraman, C. N.; Gibbs-Davis, J. M. *J. Phys. Chem. Lett.* **2012**, 1269.

(22) Leung, K.; Nielsen, I. M. B.; Criscenti, L. J. *J. Am. Chem. Soc.* **2009**, *131*, 18358.

(23) Sulpizi, M.; Gaigeot, M.-P.; Sprik, M. *J. Chem. Theory Comput.* **2012**, *8*, 1037−1047.

(24) Icenhower, J. P.; Dove, P. M. *Geochim. Cosmochim. Acta* **2000**, *64*, 4193.

(25) Campen, R. K.; Pymer, A. K.; Nihonyanagi, S.; Borguet, E. *J. Phys. Chem. C* **2010**, *114*, 8465.

(26) Sonnefeld, J. *Colloid Polymer Sci.* **1995**, *273*, 932.

(27) Dove, P. M. *Geochim. Cosmochim. Acta* **1999**, *63*, 3715.

(28) Karlsson, M.; Craven, C.; Dove, P. M.; Casey, W. H. *Aquat. Geochem.* **2001**, *7*, 13.

(29) Wallace, A. F.; Gibbs, G. V.; Dove, P. M. *J. Phys. Chem. A* **2010**, *114*, 2534.

(30) Lyklema, J. *Chem. Phys. Lett.* **2009**, *467*, 217.

(31) Parsons, D. F.; Bostrom, M.; Nostro, P. L.; Ninham, B. W. *Phys. Chem. Chem. Phys.* **2011**, *13*, 12352.

(32)   Salis, A.; Parsons, D. F.; Bostrom, M.; Medda, L.; Barse, B.; Ninham, B. W.; Monduzzi, M. *Langmuir* **2010**, *26*, 2484.

(33)   Dove, P. M.; Craven, C. M. *Geochim. Cosmochim. Acta* **2005**, *69*, 4963.

(34)   Jungwirth, P.; Tobias, D. J. *Chem. Rev.* **2006**, *106*, 1259.

(35)   Jungwirth, P.; Winter, B. *Annu. Rev. Phys. Chem.* **2008**, *59*, 343.

(36)   Chen, X.; Flores, S. C.; Lim, S.-M.; Zhang, Y.; Yang, T.; Kherb, J.; Cremer, P. S. *Langmuir* **2010**, *26*, 16447.

(37)   Chen, X.; Yang, T.; Kataoka, S.; Cremer, P. S. *J. Am. Chem. Soc.* **2007**, *129*, 12272.

(38)   Franks, G. V. *J. Coll. Interf. Sci.* **2002**, *249*, 44.

(39)   Flores, S. C.; Kherb, J.; Cremer, P. S. **2012**, *116*, 14408−14413.

(40)   Petersen, P. B.; Saykally, R. J. *Annu. Rev. Phys. Chem.* **2006**, *57*, 333.

(41)   Zhang, Y.; Cremer, P. *Curr. Opin. Chem. Biol.* **2006**, *10*, 658.

(42)   Yan, E. C. Y.; Liu, Y.; Eisenthal, K. B. *J. Phys. Chem. B* **1998**, *102*, 6331.

(43)   de Beer, A.; Campen, R.; Roke, S. *Phys. Rev. B* **2010**, *82*.

(44)   Hayes, P. L.; Malin, J. N.; Jordan, D. S.; Geiger, F. M. *Chem. Phys. Lett.* **2010**, *499*, 183.

(45)   Holland, J. G.; Malin, J. N.; Jordan, D. S.; Geiger, F. M. *J. Am. Chem. Soc.* **2011**, *133*, 2567.

(46)   Jordan, D. S.; Malin, J. N.; Geiger, F. M. *Environ. Sci. Technol.* **2010**, *44*, 5862.

(47)   Malin, J. N.; Geiger, F. M. *J Phys Chem A* **2010**, *114*, 1797.

(48)   Konek, C. T.; Musorrafiti, M. J.; Al-Abadleh, H. A.; Bertin, P. A.; Nguyen, S. T.; Geiger, F. M. *J. Am. Chem. Soc.* **2004**, *126*, 11754.

(49)   Wang, H.; Zhao, X.; Eisenthal, K. B. *J. Phys. Chem. B* **2000**, *104*, 8855.

(50)   Subir, M.; Liu, J.; Eisenthal, K. B. *J. Phys. Chem. C* **2008**, *112*, 15809.

(51)   Gibbs-Davis, J. M.; Kruk, J. J.; Konek, C. T.; Scheidt, K. A.; Geiger, F. M. *J. Am. Chem. Soc.* **2008**, *130*, 15444.

(52)   Davis, J. A.; James, R. O.; Leckie, J. O. *J. Coll. Interf. Sci.* **1978**, *63*, 480.

(53)   Goldberg, S. In *Chemical Equilibrium and Reaction Models*; Leoppert, R. H., Schwab, A. P., Goldberg, S., Eds.; Soil Science Society of America Special Publication: 1995; Vol. 42.

(54)   Lützenkirchen, J. *J. Coll. Interf. Sci.* **1999**, *217*, 8.

(55)   Urry, D. W. *What Sustains Life?: Consilient Mechanisms for Protein-Based Machines and Materials*; Springer: New York, NY, 2006.

(56)   Hiemstra, T.; Riemsdijk, W. H. V. *J. Coll. Interf. Sci.* **1996**, *179*, 488.

(57)   Sverjensky, D. A.; Sahai, N. *Geochim. Cosmochim. Acta* **1996**, 3773.

(58)   Lützenkirchen, J. *Environ. Sci. Technol.* **1998**, *32*, 3149.

(59)   Rahnemaie, R.; Hiemstra, T.; van Riemsdijk, W. H. *J. Coll. Interf. Sci.* **2006**, *293*, 312.

(60)   Sverjensky, D. A. *Geochim. Cosmochim. Acta* **2001**, *65*, 3643.

(61)   Collins, K. D.; Neilson, G. W.; Enderby, J. E. *Biophys. Chem.* **2007**, *128*, 95.

(62)   Flores, S. C.; Kherb, J.; Konelick, N.; Chen, X.; Cremer, P. S. *J. Phys. Chem. C* **2012**, *116*, 5730−5734.

(63)   Liu, D.; Ma, G.; Levering, L. M.; Allen, H. C. *J. Phys. Chem. B* **2004**, *108*, 2252.

(64)   Richter, L. J.; Petralli-Mallow, T. P.; Stephenson, J. C. *Optics Lett.* **1998**, *23*, 1594.

(65)   Yeganeh, M. S.; Dougal, S. M.; Pink, H. S. *Phys. Rev. Lett.* **1999**, *83*, 1180.

(66)   Ding, F.; Hu, Z.; Zhong, Q.; Manfred, K.; Gattass, R. R.; Brindza, M. R.; Fourkas, J. T.; Walker, R. A.; Weeks, J. D. *J. Phys. Chem. C* **2010**, *114*, 17651.

CHAPTER 4

Effects of Immobilization on DNA Recognition

Processes at the Silica/Water Interface

4.1 Introduction

The advent of strategies for immobilizing DNA onto simple glass microscope slides has revolutionized molecular biology and biodiagnostics.[1-4] By spatially controlling the presentation of different DNA sequences, microarrays can be used to sequence genomes or monitor the gene expression levels in diseased or healthy cells. Chip-based platforms are also widely used in fluorescent and colorimetric detection of oligonucleotide biomarkers associated with infectious diseases.[5] Numerous methods have been devised for immobilizing DNA to glass (silica) and other solid supports, and many of these strategies can be achieved using commercially available oligonucleotide strands and surface modifying molecules.[6] However, despite their widespread use, the effects of immobilization on the molecular recognition behavior of DNA bound to glass are not well known.

In contrast, the ability to monitor the thermodynamic and kinetic properties of immobilized DNA in real-time is straightforward when the substrate is a metal like gold. Electrochemical methods for monitoring redox active groups covalently or physically associated with DNA has allowed the thermal dissociation of DNA to be monitored in real time.[7] Other techniques like surface plasmon resonance (SPR) are also amenable to monitoring binding processes of immobilized DNA on gold substrates.[8,9] For insulating materials like silica, however, such electrochemical and SPR methods are not available. To achieve some amount of surface selectivity, total internal reflection techniques like total internal reflection fluorescence spectroscopy (TIRF) can be employed.[10] In

128

standard TIRF experiments, the surface selectivity is determined by the distance that the evanescent wave penetrates into the bulk, which is typically on the order of hundreds of nanometers. As a result, standard TIR methods cannot discriminate between fluorescent-labeled molecules bound to the interface or those present within the volume probed by the evanescent wave. For example, Krull and co-workers were able to monitor hybridization and thermal dissociation by TIRF utilizing silica fiber optics modified with oligonucleotides.[11] Significant corrections to the resulting fluorescent profiles were required to account for the presence of complementary fluorescein-labeled DNA that was not interacting with the surface but was present within the evanescent field.

4.2 Results and Discussion

4.2.1 Background Theory of Resonantly Enhance Second Harmonic Generation

Second harmonic generation (SHG)[12,13] has much greater surface selectivity than fluorescence or absorbance measurements that utilize total internal reflection configurations owing to the SHG selection rules, which require a break in inversion symmetry. For noncentrosymmetric materials like fused silica or water, inversion symmetry is only broken at the interface. Consequently any signal arising from the aqueous phase originates from molecular assemblies that possess some net orientation. The SHG intensity ($I_{2\omega}$) emanating from the interface is proportional to the square modulus of the second harmonic electric

field ($E_{2\omega}$), which depends on the incident electric field (E_ω) and the second-order susceptibility ($\chi^{(2)}$) according to:

$$I_{2\omega} = \left| E_{2\omega} \right|^2 \propto \left| \chi^{(2)} E_\omega E_\omega \right|^2 . \tag{4.1}$$

The second-order susceptibility $\chi^{(2)}$ is very small for most interfacial systems. Consequently intense lights sources like ultrafast pulsed laser assemblies are necessary for achieving high electric fields at ω that generate a measurable second harmonic response. $\chi^{(2)}$ can be decomposed into a resonant and non-resonant contribution as shown in equation 4.2:

$$\chi^{(2)} = \chi^{(2)}_{NR} + \chi^{(2)}_{Res} . \tag{4.2}$$

The resonant contribution can be related to the molecular hyperpolarizability of species present at the interface. Specifically $\chi^{(2)}$ depends linearly on the number density of molecules in resonance and the orientational average of their corresponding hyperpolarizability tensor $\beta^{(2)}$:

$$\chi^{(2)}_{Res} = N \left\langle \beta^{(2)} \right\rangle . \tag{4.3}$$

Owing to the dependence on the orientation average of the molecular hyperpolarizability, within the electric dipole approximation only oriented assemblies of achiral species contribute to $\chi^{(2)}$. Consequently, even if the species is present within the evanescent field generated by the incident laser field at ω, it will not contribute to $\chi^{(2)}$ if it is isotropically distributed within this volume. For chiral molecules there is some contribution from isotropic arrangements like those

in the bulk, but this contribution should be much smaller than those molecules with a net orientation.[14,15]

Equation 4.4 illustrates the resonant enhancement of the molecular hyperpolarizability $\beta^{(2)}$

$$\beta^{(2)} \propto \frac{A}{\omega_{ca} - 2\omega + i\Gamma} , \qquad (4.4)$$

where A is the oscillator strength, Γ is the dampening term and ω_{ca} is the resonant frequency of a particular electronic excitation. When 2ω approaches ω_{ca}, the molecular hyperpolarizability and consequently $\chi^{(2)}$ become large. This resonant enhancement allows one to monitor the presence and organization of particular molecules at the interface, which is another major advantage of second harmonic generation over techniques like SPR that do not report on the nature of the interfacial species.

DNA possesses electronic resonances in the ultraviolet region of the electromagnetic spectrum. Thus, resonantly enhanced second harmonic generation has been employed by Geiger and co-workers to monitor the association of DNA, without the addition of any labels.[16] These measurements, however, are complicated by the similar resonant wavelengths of both single-stranded and double-stranded DNA at 260 nm. Consequently, hybridization could only be discerned by comparing the signal intensities for different incident linear polarizations. The linear dichroic ratio based on these different signal intensities and the fraction of duplexes at the interface are not directly proportional, which

adds further complexity to determining the extent of hybridization from the signal changes.[17]

Scheme 4.1. Hybridization and Dissociation of SHG-Active 3-Nitropyrrole-Modified Complementary DNA.
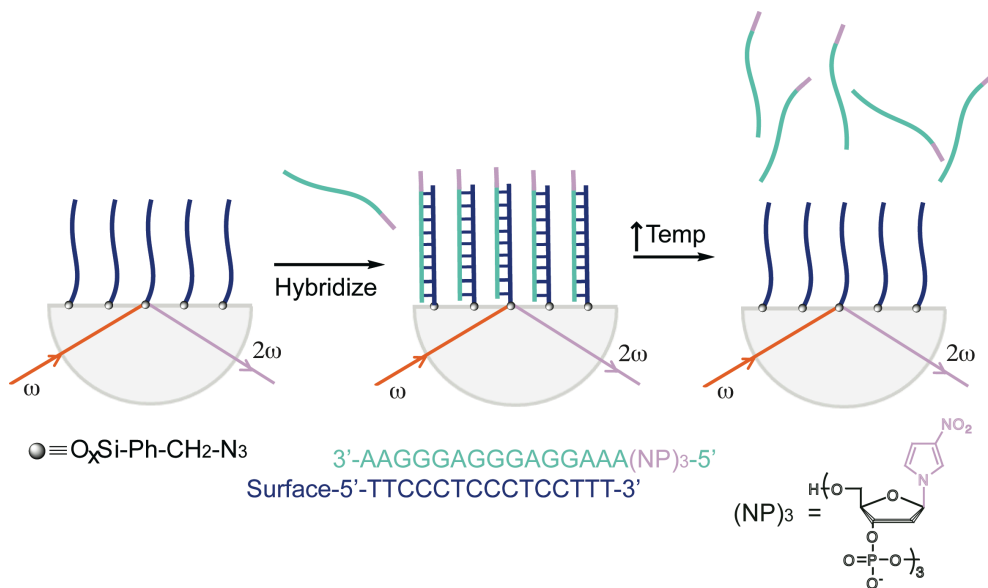
We were interested in developing a complementary SHG method for monitoring hybridization and dissociation utilizing a synthetic nucleotide that possessed a resonant frequency distinct from that of DNA. We selected the commercially available universal base 3-nitropyrrole deoxyribonucleotide as an SHG label. Although the 3-nitropyrrole is not a naturally occurring nucleobase, it forms stable interactions with all of the canonical bases. Moreover, it has a similar hydrophobicity and size to that of the pyrimidine bases. In acetonitrile, the phosphoramidite precursor of our 3-nitropyrrole nucleotide absorbs light in the UV, with a local maximum at 285 nm red-shifted from the natural nucleobases ($l_{max} \sim$ 260 nm). The presence of the lone pair on the nitrogen within the

132

heterocycle as well as the nitro withdrawing group at the 3-position suggested that 3-nitropyrrole might possess the push-pull electronic structure of classic SHG labels like 4-nitroanisole. Because the label is only present in the sequence complementary to the surface-bound strand, we could monitor hybridization and dissociation directly by monitoring changes in resonantly enhanced E_{2w} and correlating that with the surface density of the labeled strands according to equation 3 (Scheme 4.1).

4.2.2 Immobilization of DNA onto the Silica Surface

To immobilize the DNA to the silica surface, we selected the copper-catalyzed Huisgen-Meldal-Sharpless (3+2) cycloaddition, commonly referred to as a click reaction, which is a high yielding strategy for immobilizing biomolecules to a variety of substrates based on the reaction between an azide and a terminal alkyne.[18] Using our recently reported method for generating well-defined benzyl azide-functionalized monolayers on silica from a benzyl azido trimethoxysilane precursor, we performed the immobilization reaction between our monolayer and an alkyne-terminated strand using standard click conditions for biomolecules in aqueous solutions (Figure 4.1A).[19] To determine how much of the azide was converted to the DNA-immobilized triazole, we took advantage of the characteristic azide signature in the high-resolution X-ray photoelectron spectra. As shown in Figure 4.1B, the azide functional group resulted in two peaks in the N-region of the XPS spectra; as the azides were converted to triazoles

133

the peak at 401 eV grew in magnitude, while the peak at 405 eV disappeared. From the change in peak ratio, the surface conversion was determined according to our published method.[19] Specifically, upon reacting the alkyne-modified DNA overnight with our benzyl azido monolayer, the 401 eV: 405 eV ratio increased from 3.1(1) to 11(3), indicating that 15(4)% of the azides had been converted. Using an alternative method for monitoring surface conversion with XPS, we introduced a fluorine label into our alkyne-modified oligonucleotide and determined the conversion efficiency by the fluorine:nitrogen ratio in the low-resolution XPS spectra (4.1B). This analysis also yielded a conversion efficiency of 30(10)%. As a point of comparison, using phenyl azido monolayers results in the conversion of only 1% of the azides to triazole-linked DNA strands, which may correspond to differences in reactivity for phenyl vs benzyl azides. If we assume that our benzyl azide monolayer contained 3×10^{13} sites per cm^2, which is 1/3 the density of silanols on silica, then our modification method resulted in 6×10^{12} DNA strands per cm^2, or interstrand distances of 10 nm. As the polyanionic DNA strands repel one another, the density of DNA monolayers is expected to be much lower than monolayers composed of neutral small molecules, which is consistent with this fairly low density of DNA.
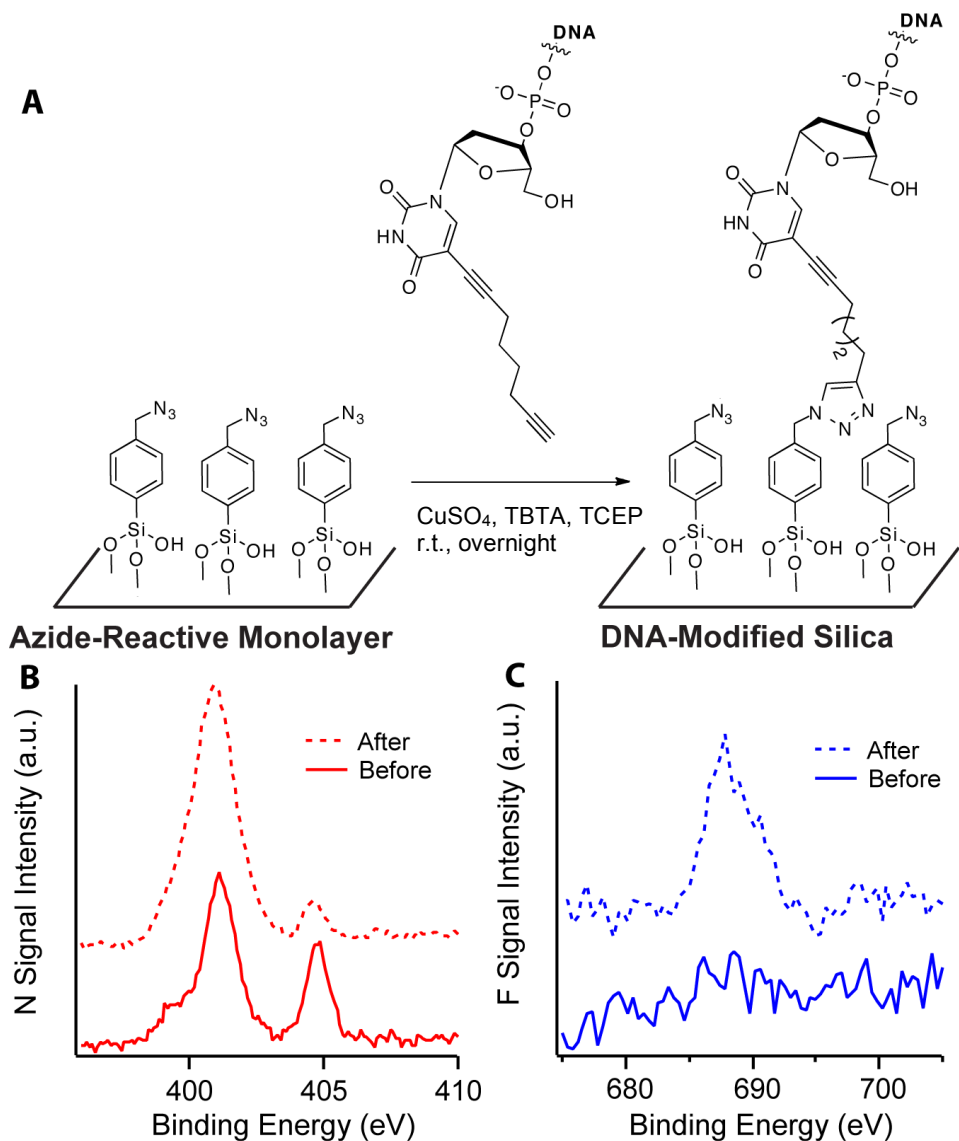
Figure 4.1 *Top*: Schematic illustration of the covalent attachment of DNA to the silica surface by reaction of a benzyl azido monolayer with alkyne-modified oligonucleotides. *Bottom*: X-ray photoelectron spectra of the benzyl azide monolayer before and after reaction with alkyne-terminated DNA. *Left plot*: The high-resolution nitrogen spectra before and after the reaction. The 401:405 eV peak ratio decreases after the reaction as a result of the conversion of azides to triazoles and the incorporation of the *N*-containing nucleotides. *Right plot*: The low-resolution fluorine spectra before and after the reaction using *F*-labeled alkyne-terminated DNA with 5-fluorodeoxyuradine in place of thymidine.

4.2.3 Hybridization of DNA Immobilized at the Silica/Buffer Interface

After verifying that DNA was immobilized at the surface by XPS, we performed similar immobilization chemistry on 1-inch diameter fused silica hemispheres. These DNA-modified hemispheres were placed into our custom-built Teflon cell (Figure 4.5), which allowed us to modulate the both the temperature and composition of the aqueous phase while simultaneously monitoring the SHG signal. Figure 4.2A illustrates the change in SHG signal at 291(1) nm upon adding 0.61 μM of the complementary oligonucleotide bearing the three terminal 3-nitropyrrole universal nucleotides, (NP)$_3$. The significant increase in signal indicated that the 3-nitropyrrole was responsible for the signal increase through resonant enhancement. Indeed, upon varying the SHG wavelength, we observed a maximum at 291.1(2) nm, which we attributed to the resonant wavelength for 3-nitropyrrole at the silica/aqueous interface (Figure 4.2B). We note that adding the same complementary strand lacking the (NP)$_3$ terminus did not lead to discernable changes in signal, consistent with previous reports indicating that both single-stranded and duplex DNA exhibit very similar SHG intensities when utilizing p-polarized incident light. After verifying that the presence of the nitropyrrole nucleotides resulted in resonant enhancement, the second harmonic electric field was directly correlated with the fraction hybridized according to equations 1-3. Although nitropyrolle is not chiral, it is directly attached to a stereogenic center at the 1'-position of ribose, and it is therefore possible that chiral tensor elements contribute to $\chi^{(2)}_{Res}$, which means that isotropic distributions of NP$_3$-DNA in the aqueous phase could contribute.[20] To

verify that the signal enhancement was due instead to NP_3-modified strands oriented at the surface, we monitored $I_{2\omega}$ when the same concentration of NP_3-DNA was added to bare silica. As shown in Figure 4.3B, the signal enhancement was very small compared to that observed for the complementary strand modified surface, which indicated that $\chi^{(2)}_{Res}$ was dominated by the anisotropic assembly of NP_3-DNA at the interface with minimum contribution from NP_3-DNA in the bulk.

Regarding the time required for hybridization, the profile of $E_{2\omega}$ versus time indicated that the complementary DNA had hybridized with the interface within 15 minutes (Figure 4.2A). Allowing the sample to hybridize for another 1 hour led to a small increase in signal (~10% intensity increase), which could suggest two possibilities. The first is that the duplexes reorganize at the interface over time, which leads to a subtle change in net orientation of the nitropyrrole groups and consequently the magnitude of $\chi^{(2)}$. To confirm this possibility requires determining the hyperpolarizability tensor of 3-nitropyrrole, which is currently unknown. The other possibility is that there are two kinetic processes occurring at the interface. We reason that the first event involves hybridization of DNA with the very accessible surface strands, which comprise most of the hybridization processes. Next, strands that more closely neighbor other immobilized strands hybridize with the DNA in solution. Because of the high charge density around these sites, the process is much slower owing to repulsive interactions. Still it is important that regarding either possibility, with this functionalization strategy we achieve rapid hybridization of most (or all) of the accessible immobilized DNA. Typical hybridization protocols using DNA-

137

functionalized chips wait hours to allow for complete hybridization. Our result indicates that only minutes are required to capture the DNA. Future work will examine the influence of DNA density on the kinetics of hybridization to determine whether higher density strategies actually lead to slow hybridization kinetics.
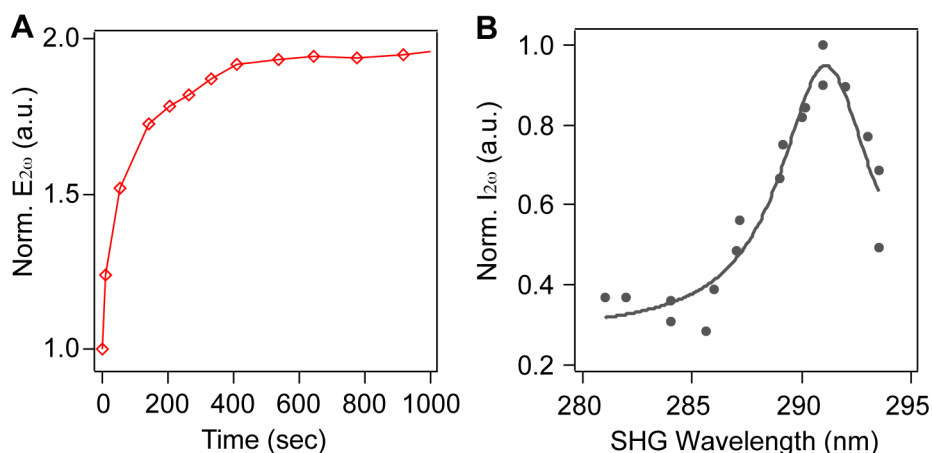
Figure 4.2 A) Change in $E_{2\omega}$ with time upon adding nitropyrolle-labeled complementary DNA to the DNA-functionalized surface. The signal levels off in approximately 500 seconds indicating that hybridization is complete. B) (B) Resonant enhancement of the SHG signal by the nitropyrrole nucleotides was verified by varying the wavelength of the incident laser field and monitoring the corresponding signal intensity at the second harmonic wavelength ($I2\omega$). A Lorentzian fit to the data is shown, which yielded a λmax value of 291.1(2) nm and a half-width half-maximum (HWHM) value of 4(1) nm. The nitropyrrole resonant peak is more narrow than that of single and double-stranded DNA at the silica/water interface (HWHM = 6(1) nm),[16] which suggests that the 3-nitropyrrole has a shorter excited state lifetime than the standard nucleobases.

As previously mentioned, the influence of immobilization on the kinetics of DNA has been extensively explored on gold surfaces utilizing primarily electrochemical methods.[7,21] These studies have found that hybridization occurs on the minute times scale, which is consistent with our observations on silica. In

contrast, the hybridization of free DNA in solution requires milliseconds, while hybridization of DNA-modified materials that form 3-dimension assemblies requires hours.[22] This comparison indicates that the restricted degrees of freedom of the immobilized strand significantly impact the rate of hybridization, but that the "2-dimensional" environment of the interface is not as constrained as that of materials forming 3-dimensional aggregates through DNA hybridization.

4.2.4 Thermal Dissociation of DNA Hybridized at the Silica/Buffer Interface

The thermodynamics of hybridization at surfaces is often determined from measuring the isotherm of the fraction surface coverage, proportional to normalized $E_{2\omega}$, versus the concentration of complementary DNA in solution. The Langmuir model is often used to determine the binding constant from such isotherm data, however, the model only holds for reversible interactions. As shown in Figure 4.3, the hybridization of DNA at this buried interface does not appear to be reversible. Specifically, removing the aqueous solution that contains 0.61 μM complementary DNA and replacing it with the same aqueous solution that lacks any DNA led to a decrease in the signal. Yet even after several minutes this signal was much greater than that of the original DNA-modified surface before the introduction of complementary $(NP)_3$-labeled DNA. The presence of irreversibly bound DNA is consistent with previous temperature-jump experiments at the buried silica-water interface, which also found that hybridization was far from reversible at this interface. Moreover, it helps

rationalize the harsh treatments used to generate microarrays, which involve boiling the microarray in water to remove any hybridized DNA.[23]
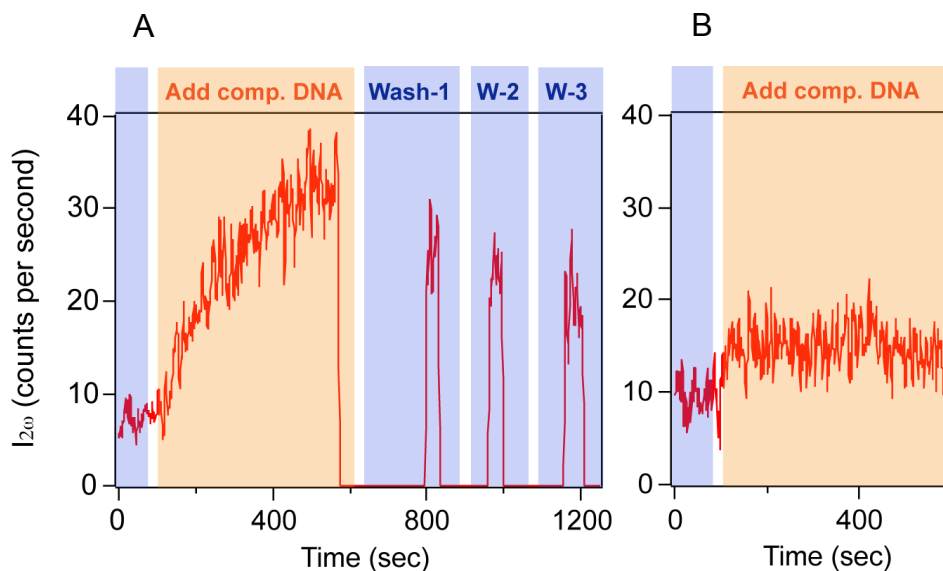
Figure 4.3 A) Illustration of the irreversibility of the DNA hybridization at the silica/water interface. The SHG signal increased approximately four-fold within five minutes upon adding the complementary DNA strand to the interface. The SHG signal did not decrease to the original intensity even after several washings with Millipore water and buffer solution indicating that the hybridization of DNA at the interface is not completely reversible. B) A very small signal enhancement was observed when the same concentration of NP_3-DNA was added to bare silica. The incident beam had to be more tightly focused to observe this resonant enhancement on bare silica, which indicates that only a small amount of NP3-DNA binds to silica or contributes via an isotropic chiral contribution to $\chi_{Res}^{(2)}$.

Another method for quantifying the affinity of DNA duplexes in solution or at surfaces involves monitoring the fraction hybridized as a function of temperature. These thermal dissociation or melting curves can be utilized to determine the temperature where half the duplexes have dissociated. Using SHG,

we measured such melting curves from the changes in resonantly enhanced $E_{2\omega}$ for DNA duplexes formed at the silica/water interface by incorporating temperature control in to our experimental set-up (Figure 4.5). The dissociation, or melting, temperature (T_m) corresponds to a normalized $E_{2\omega}$ value of 0.5, which was determined from a sigmoidal fit to the data (vide infra). For the 15mer sequence utilized in this investigation, we observed a T_m of 48(2) °C for the immobilized system in the presence of 0.3 M NaCl. In contrast, the solution-phase experiment performed with 0.61 μM of each complementary strand yielded a T_m of 60.4(1) °C. This melting analysis revealed that immobilizing one of the strands onto the surface decreased the melting temperature by approximately 12 degrees. This suppression of the T_m upon immobilization is larger than that observed for DNA immobilized at the gold/water interface as monitored by electrochemical methods.[24,25] This difference between the effect of the two interfaces indicates that immobilization on silica has a more detrimental influence on the stability of the DNA duplex than that of gold. Accordingly, when designing oligonucleotides for microarrays it is important to account for this significant depression in melting temperature.
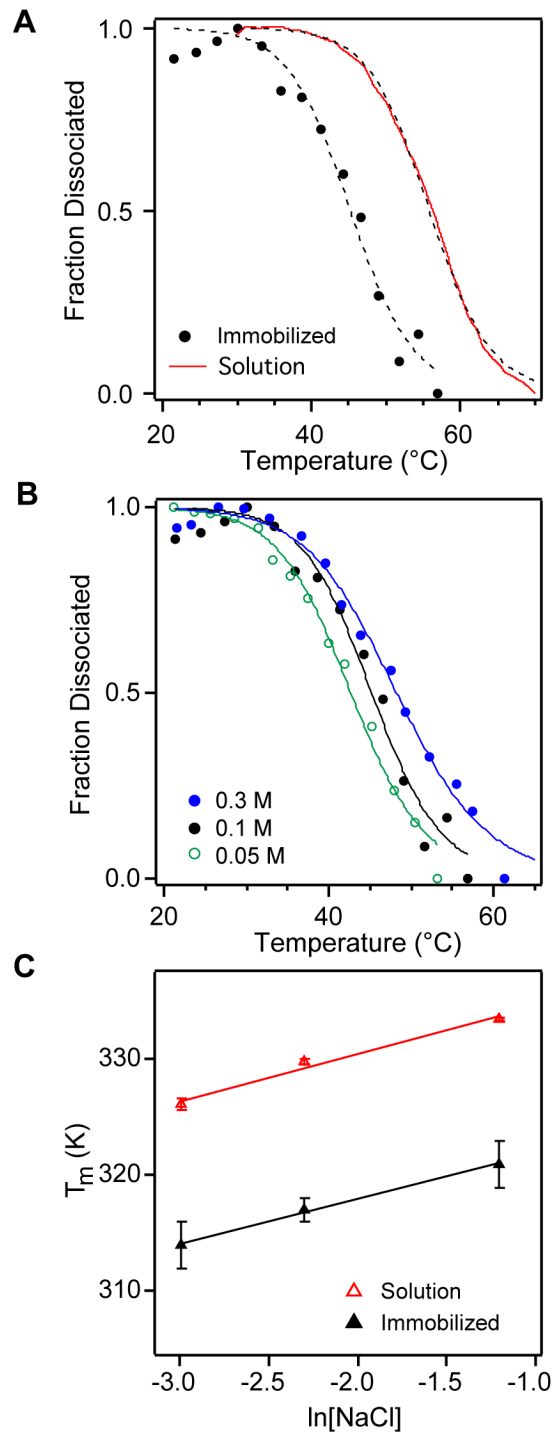
Figure 4.4 A) A comparison of the melting curves between solution and immobilized DNA in presence of a PBS buffer solution containing 0.1 M NaCl. The dashed lines are the sigmoid fits to the experimental data points from where melting points are obtained. The melting points of immobilized DNA are about 12 °C lower than that of the solution-phase DNA. B) Melting curves for the

immobilized DNA at the silica/buffer interfaces containing 0.05 M, 0.1 M, and 0.3 M NaCl. C) Variation of T_m as a function of the natural logarithm of the electrolyte strength. Black line represents the linear dependence that corresponds to the immobilized DNA at the interface and red line to the corresponding DNA in solution. The surface T_m varies linearly with ln[NaCl] resulting the same slope as that obtained in solution but shifted by about 12 °C.

To quantify the thermodynamic parameters associated with these melting events and gain insight into the reason behind the destabilizing effect of silica, we utilized the following sigmoidal function that relates the fraction dissociated to the temperature according to:

$$\text{Fraction Dissociated} = \frac{1}{1 + \exp\left(\frac{-\Delta H}{R}\left(\frac{1}{T + 273.14} - \frac{1}{T_m + 273.14}\right)\right)} \qquad (4.5)$$

where T_m is the melting temperature in Celsius, ΔH is the dissociation enthalpy and R is the ideal gas constant. The values listed in Table 1 represent the average of values determined from two or more independent measurements and the reported error represents the standard deviation. We compared the melting behavior of solution and surface-bound duplexes for three different salt concentrations. For both systems the melting temperature increased with increasing salt concentration, which stems from the decrease in charge repulsion between the hybridizing strands with greater concentrations of NaCl. According to condensed cation theory,[26] the T_m versus ln[salt] should be linear, which we indeed observed for both the solution and surface systems (Figure 4.4C). The slope of both lines is very similar revealing that both the solution and the surface

143

systems exhibit similar salt dependence, which has also been observed at other solid/aqueous interface.[24,27]

The trends in ΔH, however, vary between the surface and solution phase systems. For the solution phase system, we found that the ΔH of dissociation increased with increasing salt concentration, which is predicted by Manning theory owing to the stabilizing effect of salt on the duplex. In contrast, the ΔH for the surface-bound DNA appears to remain unchanged with increasing salt concentration, although the significant error in the ΔH values makes the trend inconclusive. We note that Krull and co-workers observed that the ΔH of dissociation decreased with increasing salt concentration in their TIRF measurements utilizing DNA-immobilized on silica fiber optics.[27] They attributed this to the screening of the negative charge by the salts that might have reduced the repulsive force between the single stranded DNA with the neighboring strands or any ionized surface silanol groups. However, another effect of increasing salt concentration that may influence the ΔH of DNA dissociation is the increased ionization of surface silanol sites. Many silica studies have found that increasing the NaCl concentration led to deprotonation of the surface, and therefore, an increase in the number of negatively charged sites.[28,29] In their TIRF investigation, Krull and coworkers capped the unreacted silanol groups with chlorotrimethoxysilane prior to DNA assembly on the surface, so the surface deprotonation of silanol sites may have played less of role. However, Kopelman and co-workers observed that deprotonation can occur even with monolayers present due to incomplete condensation between the monolayer and the surface

silanols.[30] For our systems, the two opposing effects of increasing salt concentration, minimizing the repulsion of the hybrid duplex and ion-induced ionization of the silanol groups, led to a lack of trend in ΔH.

Table 4.1 Melting temperatures and thermodynamic parameters (enthalpy changes) measured for the surface and solution phase melting processes.

System	[NaCl] (M)	ΔH (kcal/mol)	T_m (°C)
Immobilized	0.05	45.0(9)	41(2)
	0.1	49(5)	44(1)
	0.3	42(8)	48(2)
Solution	0.05	47.9(2)	53.0(5)
	0.1	52.75(5)	56.7(3)
	0.3	54.3(3)	60.4(1)

4.3 Concluding Remarks

In conclusion, we utilized second harmonic generation (SHG) as an inherently surface specific technique to observe processes at the DNA-immobilized silica/water interface. Using a universal 3-nitropyrolle nucleotide as an SHG-active label, we monitored the hybridization rate and thermal dissociation of a 15-mer of DNA immobilized at the silica/aqueous interface. The immobilized DNA exhibited hybridization rates on the minute timescale, which is much slower than hybridization kinetics in solution, but on par with hybridization observed at electrochemical interfaces. Additionally, the thermal dissociation temperature of the DNA immobilized on silica was on average 12 °C lower than

the analogous duplex in solution. This decrease in melting temperature is more significant than that observed on other surfaces like gold. We attributed the destabilizing affect of silica to its negatively charged surface at neutral pH that repels the hybridizing complementary DNA.

4.4 Experimental Section

4.4.1 Materials and Instruments

The DNA was synthesized on an Applied Biosystems Model 392 DNA/RNA Synthesizer. Standard phosphoramidite and synthesis reagents from Glen Research were used including the alkyne-modified thymine (T_{alkyne}, Glen Research, catalog # 10-1540-95), the fluorine modified cytodine (C_F, Glen Research, catalog # 10-3415-02) and the nitropyrolle modified nucleotide phosphoramidite (**NP**, Glen Research, catalog # 10-1043-90). DNA purification was performed using the DMT-On method with Glen-Pak cartridges also from Glen Research. All other reagents were purchased from Aldrich Chemicals, Alfa Aesar, Fisher Scientific or VWR and used without further purification. Melting analyses of DNA-containing materials were performed using an HP 8453 diode-array spectrophotometer equipped with a HP 89090A Peltier temperature controller.

Table 4.2 DNA Sequences that are Used in this Study.

Strand	Sequence	Experiments
I	3'-AAGGGAGGGAGGAAA(NP)$_3$-5'	Surface and solution thermal dissociation
II	3'TTTCCTCCCTCCCTTT$_{alkyne}$-5'	Surface and solution thermal dissociation
III	3'AAAAAAAAAAAAAAAT$_{alkyne}$-5'	Surface thermal dissociation (control)
IV	3'TTTC$_F$C$_F$TC$_F$C$_F$C$_F$TC$_F$C$_F$C$_F$TTT$_{alkyne}$-5'	XPS functionalization

4.4.2 Laser System and SHG Assembly

The laser system used in these experiments consists of a femtosecond Ti:Sapphire oscillator (Spectra Physics, Mai Tai, 80 MHz) and a Nd:YLF laser (Spectra Physics, Empower) used to seed and pump, respectively, a regeneratively amplified laser (Spitfire Pro, Spectra Physics, 1 kHz, 100 fs, 3.3 w). One third of the Spitfire output is used to pump an optical parametric amplifier (Spectra Physics OPA-800CF). The output from the OPA was tunable from 550 – 595 nm. It was attenuated to 0.33 ± 0.03 mJ by a neutral-density filter (New Focus, cat. # 5215), and directed through a half-wave plate and polarizer for p-polarization selection. The polarized light was focused onto the fused silica/water interface at an angle of 62° from surface normal near total internal reflection. The reflected second harmonic light generated at the interface was then passed through a color glass filter (Thorlabs) to remove the reflected fundamental light and focused onto a monochromator (Optometrics Corp., Mini-Chrom MC1-02) tuned to the second harmonic wavelength. SHG was detected by a photomultiplier tube (PMT,

147

Hamamatsu Photonics), and the electric response from the PMT was then amplified and counted with a gated photon counter (Stanford Research Systems). Before performing each experiment, the quadratic power dependence and SHG wavelength dependence were verified to ensure no optical damage was occurring at the interface.

4.4.3 Preparation of Immobilized DNA Samples

Silicon wafers containing a native oxide layer were used as substrates for XPS measurements and quartz hemispheres were used for SHG experiments. Both substrates were cleaned prior to use by sonicating it in Millipore water followed by methanol and then in water again. The clean substrates were then reacted with freshly prepared *piranha* solution (3:1 mixture of concentrated H_2SO_4 and 30% H_2O_2) at about 100 °C temperature to make sure any old organic layer is completely removed, specifically from the quartz hemisphere that are repeatedly used for surface modification. After 1 hour the substrates were copiously rinsed in Millipore water followed by sonication in water (5 minutes × 2), in methanol (5 minutes) and then in water again (5 minutes). After the substrates were allowed to dry in an oven at 100 °C for 10 minutes, it was cooled down to room temperature and then plasma cleaned (Plasma cleaner, PDC-32G, Harrick Plasma) in air for 2-3 minutes. Cleaned samples were rinsed with a stream of methanol (15 mL), a mixture of methanol and toluene (1:1 v/v, 15 mL), and finally a stream of toluene (15 mL), and then reacted with a 5 mM solution of the benzyl azido trimethoxysilane in dry toluene with 0.1 % water (v/v) for 5 hours. After the 5-

148

hour reaction time, the samples were rinsed thoroughly with toluene (15 mL), sonicated for one minute each in toluene (15 mL), toluene/methanol (15 mL) and methanol (15 mL) and then blown dry with a stream of nitrogen gas. The azido-modified substrates were then placed in oven at 100 °C for 30 minutes and then cooled down before they were further used in the reaction with alkyne-terminated DNA.

The following procedure for immobilizing DNA to silica via [3+2] cycloaddition reaction of alkyne-terminated DNA with benzyl azido surface was modified from a procedure described by Sun and coworkers.[31] A catalyst mixture of CuSO$_4$–TBTA–TCEP (1:1:1 mole ratio) was prepared: *tris*-(benzyltriazolylmethyl)amine (TBTA) (20 nmols, 1.1 mg) was weighed in a 1-mL vial and added to 3:1 mixture of DMSO/t-BuOH (50 µL). Additional DMSO (100 µL) was added to the TBTA to dissolve it completely and then a solution of CuSO$_4$ (20 nmols CuSO$_4$ in 50 µL of 0.3 M NaCl) was slowly added to the TBTA solution. Tris(carboxyethyl)phosphine (TCEP) solution (20 nmols (0.6 mg) TCEP in 100 µL of 0.3 M NaCl) was prepared in another 1-mL vial and then slowly mixed with TBTA solution. A greenish yellow clear solution was appeared at this stage (total volume should be 300 µL). Alkyne-terminated DNA (30 nmols) was dissolved in PBS buffer (100 µL, 0.3 M NaCl, pH 7.0) and DMSO (100 µL) in a 0.6-mL centrifuge tube. The catalyst mixture (300 µL) was then slowly added to the centrifuge tube containing the alkyne-DNA and the tube was mixed with the help of a vortex to obtain a clear solution. The DNA solution with the catalyst-ligand complex obtained at this point was placed on top of the reactive surface of

hemispheres or silicon wafers modified with azido SAMs. The substrates were placed in a petri dish with some water in it (function of water in the petri dish is to provide with a humid environment inside the petri dish thus avoiding evaporation of the reacting solution from the top of the surface), which was then capped, covered with foil, and allowed to react overnight. The reacted azido SAMs were then taken out of the petri dish and rinsed with water (10 mL), ethanol (10 mL), DMSO (15 mL), ethanol (15 mL) again and water (15 mL) again at the end to completely remove any unreacted DNA. Finally, the samples were blown dry with a stream of nitrogen and either immediately used for SHG experiments or stored under vacuum for XPS measurements performed within 2 – 5 days.

4.4.4 XPS Analysis

XPS measurements were performed using the AXIS ULTRA spectrometer (Kratos Analytical) on silicon wafers with a native oxide layer that had been functionalized with single-stranded DNA (Sequence IV, Table 1) within the last four days. The base pressure in the analytical chamber was lower than 3 x 10^{-8} Pa. The monochromatic Al Kα source (hν = 1486.6 eV) was used at a power of 210 W. The photoelectron exit angle was 90 degrees and the incident angle was 35.3 degree from the plane of the surface. The analysis spot was 400 x 700 μm. The resolution of the instrument was 0.55 eV for Ag 3d and 0.70 eV for Au 4f peaks. Survey scans were collected for binding energies from 1100 eV to 0 eV with an analyzer pass energy of 160 eV and a step of 0.35 eV. The high-resolution spectra were run with a pass-energy of 20 eV and a step of 0.1 eV. Relative sensitivity

factors (RSF) for different elements were as follows: 1 for F (1s), 0.477 for N (1s), 0.955 for Br (3d). Experiments were performed on three different samples and the average N:F ratio and standard deviation were used to determine the conversion efficiency of the reaction and the error according to:

$$\% yield = \frac{\# DNA}{\# Azide} \times 100\% = \frac{\dfrac{F}{8}}{\left(\dfrac{N - \dfrac{40F}{8}}{3}\right)} \times 100\% \qquad (4.6)$$

Similarly, the average ratio at 401 eV and 405 eV from the high-resolution spectrum were utilized to determine the conversion efficiency using the method described in our previous work. Because the DNA contained multiple nitrogen atoms per nucleotide the conversion efficiency was determined from:

$$Yield = \frac{\# DNA}{\# Azide} \times 100\% = \frac{\dfrac{N_{401eV} - 3.1N_{405eV}}{43}}{\dfrac{N_{401eV} - 3.1N_{405eV}}{43} + \dfrac{3.1N_{405eV}}{3}} \times 100\% \qquad (4.7)$$

4.4.5 SHG Hybridization and Melting Experiments

Prior to the start of an experiment, each sample was exposed to buffer solution until the SHG signal was optimized. All experiments were performed with freshly prepared DNA surface. DNA modified hemisphere was placed first in a custom made steel sample cell, which was connected to a heater and temperature controller as shown in Figure 4.6. The sample cell was then filled up with a buffer solution (1.2 mL) that covered the flat surface of the hemisphere.

After optimizing the SHG signal generated from the buried interface a solution of the complementary DNA (20.7 µM, 36 µL) was added while collecting SHG signal simultaneously. After watching the hybridization for about 15 minutes the beam was blocked to avoid any chance of burning the sample. One hour later the heater with temperature controller attached the sample cell was turned on and SHG signal was collected for 1 minute at every 1 to 2 °C intervals after 1-minute hold time at each temperature. $\chi^{(2)}_{Res}$ was measured by subtracting the nonresonant SHG signal (after melting) from the absolute SHG signal followed by taking the square root (equation 4.8), assuming that the phase difference between the resonant and nonresonant second-order susceptibilities is 90°.[32] The fraction of the DNA duplex dissociated was then directly measured by normalizing the $\chi^{(2)}_{Res}$ data plotted against temperature by the maximum $\chi^{(2)}_{Res}$ value to construct the melting curves.

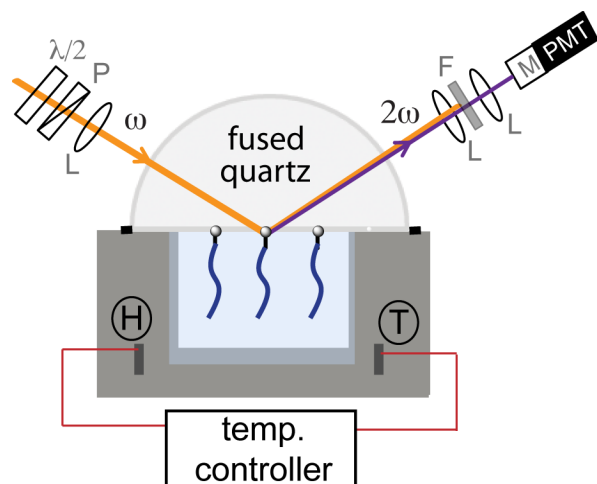$$\chi^{(2)}_{Res} = \sqrt{I_{2\omega} - I_{2\omega,NR}} \qquad (4.8)$$

Figure 4.5 Bird's eye view of the SHG the stainless steel sample cell with temperature control. $\lambda/2$ represents a half-wave plate, P a polarizer, L a lens for focusing or recollimating the beam, F an optical filter for removing the reflected fundamental light at ω and M is a monochromator connected to a photomultipler tube (PMT) for performing single photon counting. H and T are the heating element and thermometer, respectively.

4.4.6 Solution-Phase Melting Experiments

We combined 0.61 nmol of each DNA sequence in PBS buffer (1.0 mL, 10 mM PBS, pH 7.0). The mixture was allowed to equilibrate for at least 30 minutes in the fridge. Using UV-Vis ChemStation Software, we programmed the temperature profile, so that absorbance readings at 260 nm were taken from 30 to 70 °C at 1 °C intervals, with one minute hold time at each temperature. The samples were stirred at 100 rpm during the temperature-variation experiment. The resulting profiles were baseline corrected by subtracting the absorbance at 400 nm.

4.5 References

(1)   Borisov, S. M.; Wolfbeis, O. S. *Chem. Rev.* **2008**, *108*, 423.

(2)   Taton, T. A.; Mirkin, C. A.; Letsinger, R. L. *Science* **2000**, *289*, 1757.

(3)   Wang, J. *Nucleic Acids Res.* **2000**, *28*, 3011.

(4)   Beaucage, S. L. *Curr. Med. Chem.* **2001**, *8*, 1213.

(5)   Tallury, P.; Malhotra, A.; Byrne, L. M.; Santra, S. *Adv. Drug Deliv. Rev.* **2010**, *62*, 424.

(6)   Heise, C.; Bier, F. F. *Top Curr. Chem.* **2006**, *261*, 1.

(7)   Fan, C.; Plaxco, K. W.; Heeger, A. J. *Proc. Natl. Acad. Sci. USA* **2003**, *100*, 9134.

(8)   Jordan, C. E.; Frutos, A. G.; Thiel, A. J.; Corn, R. M. *Anal. Chem.* **1997**, *69*, 4939.

(9)   Gao, Y.; Wolf, L. K.; Georgiadis, R. M. *Nucleic Acids Res.* **2006**, *34*, 3370.

(10)   Groves, J. T.; Parthasarathy, R.; Forstner, M. B. *Annu. Rev. Biomed. Eng.* **2008**, *10*, 311.

(11)   Erickson, D.; Li, D.; Krull, U. J. *Anal. Biochem.* **2003**, *317*, 186.

(12)   Eisenthal, K. B. *Accounts Chem. Res.* **1993**, *26*, 636.

(13)   Eisenthal, K. B. *Chem. Rev.* **1996**, *96*, 1343.

(14)   Kissick, D. J.; Wanapun, D.; Simpson, G. J. *Annu. Rev. Anal. Chem.* **2011**, *4*, 419.

(15)   Fischer, P. In *Comprehensive Chiroptical Spectroscopy*; John Wiley & Sons, Inc.: 2012, p 347.

(16)   Boman, F. C.; Gibbs-Davis, J. M.; Heckman, L. M.; Stepp, B. R.; Nguyen, S. T.; Geiger, F. M. *J. Am. Chem. Soc.* **2008**, *131*, 844.

(17)   Burke, B. J.; Moad, A. J.; Polizzi, M. A.; Simpson, G. J. *J. Am. Chem. Soc.* **2003**, *125*, 9111.

(18)   Hein, J. E.; Fokin, V. V. *Chem. Soc. Rev.* **2010**, *39*, 1302.

(19)   Azam, M. S.; Fenwick, S. L.; Gibbs-Davis, J. M. *Langmuir* **2010**, *27*, 741.

(20)   Ji, N.; Shen, Y.-R. *J. Am. Chem. Soc.* **2005**, *127*, 12933.

(21)   Herne, T. M.; Tarlov, M. J. *J. Am. Chem. Soc.* **1997**, *119*, 8916.

(22)   Rogers, P. H.; Michel, E.; Bauer, C. A.; Vanderet, S.; Hansen, D.; Roberts, B. K.; Calvez, A.; Crews, J. B.; Lau, K. O.; Wood, A.; Pine, D. J.; Schwartz, P. V. *Langmuir* **2005**, *21*, 5562.

(23)   Cheung, V. G.; Morley, M.; Aguilar, F.; Massimi, A.; Kucherlapati, R.; Childs, G. *Nat. Genet*. **1999**, *21*, 15.

(24)   Meunier-Prest, R.; Raveau, S.; Finot, E.; Legay, G.; Cherkaoui-Malki, M.; Latruffe, N. *Nucleic Acids Research* **2003**, *31*, e150.

(25)   Surkus, A.-E.; Flechsig, G.-U. *Electroanalysis* **2009**, *21*, 1119.

(26)   Perkins, D. V. *Manning theory and the person-environment model of behavior: an empirical evaluation*; Indiana University., 1978.

(27)   Piunno, P. A. E.; Watterson, J.; Wust, C. C.; Krull, U. J. *Anal. Chim. Acta* **1999**, *400*, 73.

(28)   Campen, R. K.; Pymer, A. K.; Nihonyanagi, S.; Borguet, E. *J. Phys. Chem. C* **2010**, *114*, 8465.

(29)   Stumm, W.; Morgan, J. J. *Aquatic Chemistry: Chemical Equilibria and Rates in Natural Waters; Third Edition*; Wiley, 1995.

(30)   Zhao, X.; Kopelman, R. *J. Phys. Chem.* **1996**, *100*, 11014.

(31)   Qing, G.; Xiong, H.; Seela, F.; Sun, T. *J. Am. Chem. Soc.* **2010**, *132*, 15228.

(32)   Mifflin, A. L.; Musorrafiti, M. J.; Konek, C. T.; Geiger, F. M. *J. Phys. Chem. B* **2005**, *109*, 24386.

CHAPTER 5

Increasing Complexity at the Silica/Liquid Interface Using Orthogonally Reactive Azide-Amine Mixed Monolayers

Azam, M. S.; Fenwick, S. L.; Gibbs-Davis, J. M. "Orthogonally Reactive
SAMs as a General Platform for Bifunctional Silica Surfaces," *Langmuir*,
2011, 27, 741-750.

5.1 Introduction

With advances in materials and polymer chemistry, multifunctional materials are becoming increasingly accessible.[1] Such materials that combine targeting, imaging, and therapeutic functions onto one scaffold have the potential to revolutionize the treatment of disease.[2] In addition to materials,[3] controlling the combination of specific functional groups in self-assembled monolayers (SAMs) is desirable for research requiring well-defined surfaces[4] such as biodiagnostics,[5-7] cell biology,[8,9] and mechanistic studies of immobilized catalysts.[10,11] With multifunctional monolayers, synergistic and cooperative effects can be explored between neighboring immobilized functional groups.[12-14] For example, mixed adlayers containing two types of catalysts have been synthesized on silica where each immobilized catalyst activates a different reactant in the catalytic cycle.[10] Such cooperative catalysts have garnered much attention because they can increase the scope and efficiency of catalytic transformations.[15] In this and other cooperative interfacial systems, the distance between the two immobilized groups must be on molecular length scales.[10,13] Unlike nanometer-scale surface patterns that can be fabricated from lithographic techniques, to immobilize pairs of functional groups within sub-nanometer distances, the groups must be mixed within the monolayer.[11,16,17]

Such mixed monolayers are typically synthesized by introducing the surface to a mixture of two surface-reactive molecules.[16] In many examples, one molecule with a functional group of interest is diluted in the mixed monolayer by another molecule that does not have any specific function.[4,11,18] For example,

158

receptor molecules in a monolayer are often spaced out from one another with an excess of ethyleneglycol-terminated surface reactive groups.[16,18] This "dilution" molecule can minimize nonspecific interactions with the monolayer. Alkyl terminated surface reactive groups are also often used to vary the surface density in mixed monolayers.[16] To quantify the surface density in such mixed monolayers, Collman, Chidsey and coworkers used cyclic voltammetry to measure the absolute surface coverage of an electrochemically active group diluted in an alkyl monolayer.[19] The ratio of the electrochemically active molecule and the dilution molecule was inferred from IR measurements but could not be directly measured because the dilution molecule lacked any electrochemical or IR signature. Indeed, it is often difficult to find unique spectroscopic or electrochemical signatures for each component in a mixed monolayer. As a result, the solution ratio of the two components is often used as a guide for the surface ratio.[9]

Other groups have characterized the composition of bifunctional monolayers where the two head groups have distinguishable signatures in IR absorbance or X-ray photoelectron spectroscopy (XPS). These experiments explored the influence of the head group, the alkyl chain length, and the solvent polarity on the ratio of the two components in the resulting monolayer.[20,21] Significantly, it was found that the surface ratio could vary drastically from the solution ratio depending on the experimental conditions. Consequently, this early work in the field of self-assembly led by the Whitesides group established that surface ratio determination in mixed monolayers requires quantitative surface

159

characterization methods.[20]

Combining multiple functions into a monolayer will be critical for understanding cooperative effects in biological and materials systems.[12] The difficulty in characterizing and controlling the distribution and ratio of various functional groups, however, has slowed the development of well-defined and structurally complex bifunctional surfaces. Therefore, the development of general methods for making controlled multifunctional monolayers is needed to accelerate progress in this area.[17] In the following, we outline a general strategy for accessing different combinations of functions on silica based on a mixed SAM containing two orthogonally reactive groups. By characterizing and controlling their surface ratio, the ratio of virtually any mixture of surface-bound molecules can be controlled (Scheme 5.1). Additionally, by combining self-assembly with orthogonal reactivity, bifunctional mixed monolayers become available that are not easily accessed through direct self-assembly methods. Hudalla and Murphy employed this concept in a trifunctional mixed monolayer on gold consisting of a small percentage of azides and carboxylic acid-terminated thiols mixed within an ethylene glycol-terminated monolayer. The azide and an activated form of the acid could then be reacted with two peptides containing alkynyl and nucleophilic groups, respectively. Although the amount of azide and acid was varied, the absolute ratio of these two orthogonal groups was not determined.[14] Moreover, the acid and azide represented only a small fraction of the monolayer, which is not ideal for applications requiring a high density of surface reactive sites like cooperative catalysis. Therefore, to develop densely functionalized orthogonally

reactive surfaces of controlled ratios, a new system must be developed. Herein, we demonstrate a quantitative approach to control the ratio of functional groups in monolayers post-SAM formation, starting from a well-defined azide-amine mixed monolayer.

**Scheme 5.1** Generating Bifunctional Surfaces from Orthogonally Reactive SAMs
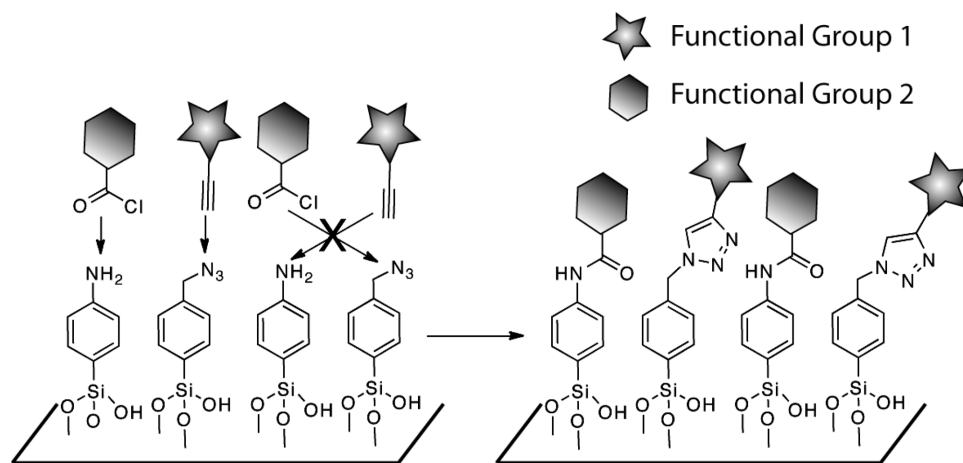
5.2 Results and Discussion

5.2.1 Our Strategy and Synthesis of Monolayer Precursors

Our strategy requires the selection of two reactive groups that exhibit orthogonal reactivity; in other words, they should not react with one another or the other's reactive partner (Scheme 5.1). One obvious choice of reaction is the Cu-mediated cycloaddition of surface-bound azides with terminal alkynes owing to the functional group tolerance, specificity, and high reactivity associated with this click reaction.[1,19,26-29] As a complementary reaction, amine-terminated monolayers have been used to introduce substituted electrophiles onto surfaces and other

materials.[4] Commercially available p-aminophenyl trimethoxysilane was selected because it is known to make uniform reactive SAMs.[25] For the azide monolayer, most azido SAMs on silica are synthesized post-self- assembly by reaction of an alkyl halide SAM with sodium azide.[26,30] Because alkyl halides and amines react with one another, we had to develop a method for the direct assembly of azido SAMs to generate mixed monolayers with amino silanes. Therefore, we synthesized two azido trimethoxysilanes from the reaction of sodium azide with p-(trimethoxysilyl)benzylchloride and n-(trimethoxysilyl)propylchloride (Scheme 5.2). With the corresponding benzyl and propyl azido silanes in hand, we were able to explore the influence of the azide structure on monolayer self-assembly. Additionally, by directly incorporating the azide into the monolayer, we prevented the incorporation of unreacted alkyl halides, which is a potential problem in post-self-assembly modification strategies.[30]

Scheme 5.2 Synthesis of Azido Trimethoxysilane
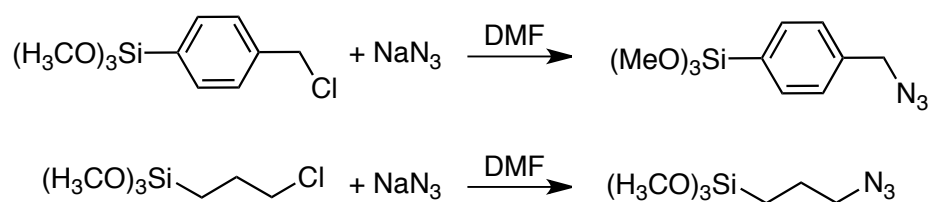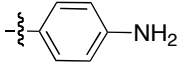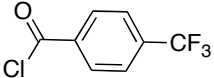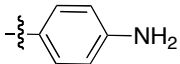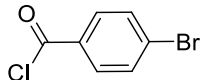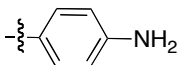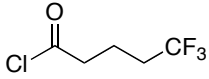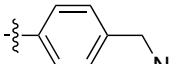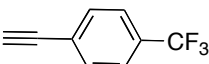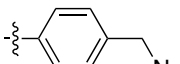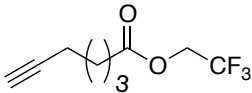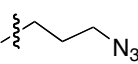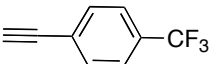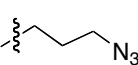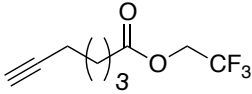
5.2.2 Synthesis and Reactivity of Monofunctional SAMs

The synthesis and reactivity of the monofunctional SAMs were first explored by exposing silica surfaces to 3.0 mM solutions of the corresponding trimethoxysilane in toluene (0.1% water v/v) for 4 h. The presence of the amine and azide functional groups was confirmed by AFM and water contact angle

162

measurements (vide infra). To quantify the extent of reaction between the amino or azido SAM with their solution-phase reactive partners, we elected to use XPS and CF_3-labeled acid chlorides and alkynes, respectively. From the XPS spectra, the percent completion can easily be determined, where 100% surface conversion of the amines leads to a F/N ratio of three, and conversion of all azides leads to a F/N ratio of one. Quantification of the XPS F1s and N1s signal intensities indicated that exposing the aminophenyl SAM overnight to CF_3-substituted benzoyl chloride led to quantitative formation of the amide (Table 5.1, entry 1; Figure 5.1A). To determine the amino SAM reactivity with aliphatic acid chlorides, we performed the same experiment with CF_3-butanoyl chloride (Table 5.1, entry 3). High yields were also observed for this reactant, which supports previous reports indicating that different substituted acid chlorides can be attached to these aminophenyl monolayers.[31] Next, we examined the reactivity of the propyl azido SAM and benzyl azido SAM in the overnight reaction between the azido monolayers and p-(trifluoromethyl)phenyl acetylene. We were pleased to note that quantitative conversion to the triazole occurred with azido SAMs directly assembled on silica (Table 5.1, entries 4 and 6; Figure 5.1B,C). High conversions were also observed with an aliphatic alkyne, indicating that our new azido SAMs have broad reactivity (Table 5.1, entries 5 and 7). The ability of all of our SAMs to react with aromatic and aliphatic reactants is important because it indicates that a wide variety of substituted alkynes and acid chlorides can be attached using these monolayers, which supports the generality of our strategy.

Table 5.1 XPS Data and Percent Conversions for the Amine and Azide Monofunctional SAMs Before and After Reaction with Various Reactants[a]

	Surface	Reactant	F:N (Br:N)	% Conversion
1	—phenyl—NH₂	4-(trifluoromethyl)benzoyl chloride	3.0 ± 0.3	100 ± 10
2	—phenyl—NH₂	4-bromobenzoyl chloride	(0.87 ± 0.02)	87 ± 2
3	—phenyl—NH₂	4,4,4-trifluorobutanoyl chloride	2.68 ± 0.05	89 ± 2
4	—phenyl—CH₂—N₃	1-ethynyl-4-(trifluoromethyl)benzene	1.06 ± 0.04	106 ± 4
5	—phenyl—CH₂—N₃	2,2,2-trifluoroethyl hept-6-ynoate	0.9 ± 0.1	90 ± 10
6	—propyl—N₃	1-ethynyl-4-(trifluoromethyl)benzene	1.2 ± 0.2	120 ± 20
7	—propyl—N₃	2,2,2-trifluoroethyl hept-6-ynoate	0.9 ± 0.2	90 ± 20

[a]Data represent the average of at least two samples made from separate batches. The error indicates the range of measured values.
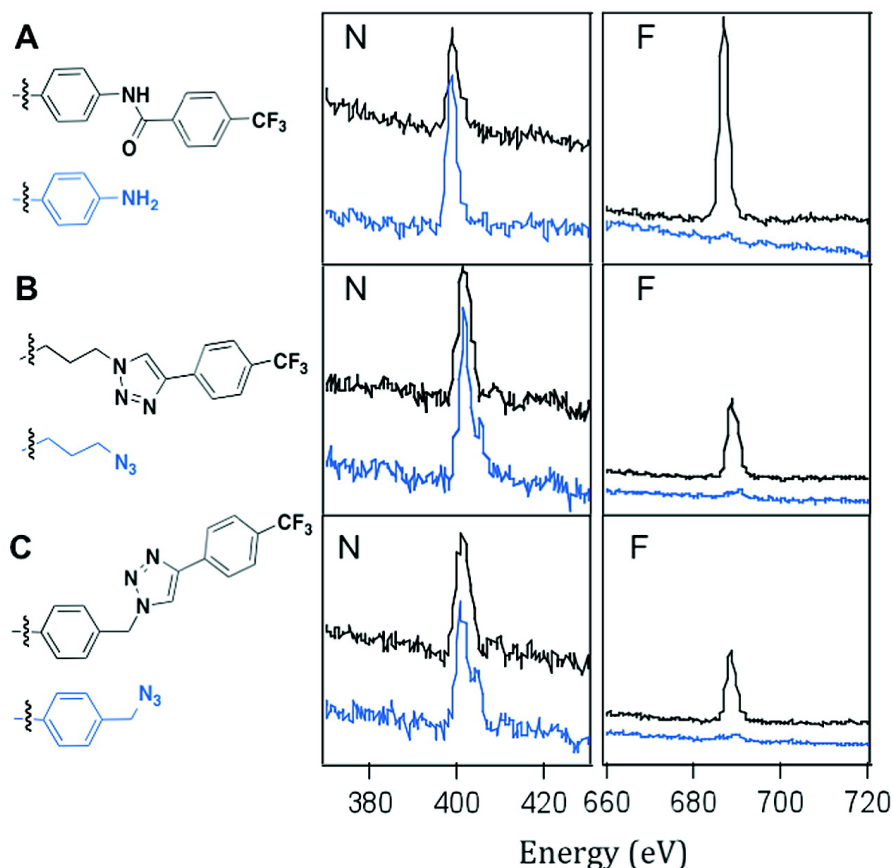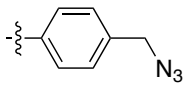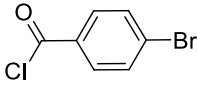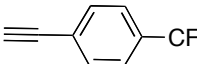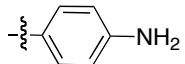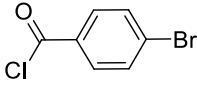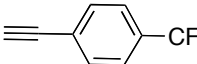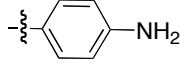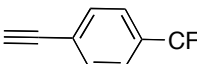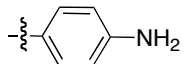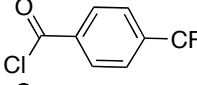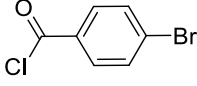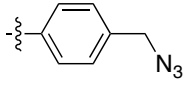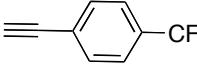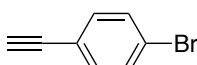
Figure 5.1 N1s and F1s XPS data for the monofunctional A) amino B) propyl azido and C) benzyl azido SAMs before and after reaction with their corresponding CF_3-labeled reactive partner. The intensity of the N1s XPS signal has been multiplied by 3.5 to allow comparison with the stronger fluorine signal.

Finally, control experiments were performed that indicated that neither the azido SAMs nor the amino SAM exhibited cross reactivity with acid chlorides and alkynes, respectively, under appropriate reaction conditions. For the benzyl azido SAM very little 4-bromobenzoyl chloride adsorbed (Entry 1, Table 5.2). Similarly very little or no 4-(trifluoromethyl)phenyl ethyne was found on the amide- (Entry 2, Table 5.2) or the amine- (Entry 3, Table 5.2) modified surfaces. On the other hand, the reaction of monofunctional benzyl azido SAM with a 1:1 mixture of 4-bromophenyl ethyne and 4-(trifluoromethyl)phenyl ethyne resulted

165

in a very different F/Br ratio than the solution ratio (Entry 4, Table 5.2; solution F/Br ratio is 3). Similarly, different F/Br ratio was obtained after the reaction of the monofunctional amino SAM with 1:1 mixture of 4-bromobenzoyl chloride and 4-(trifluoromethyl)benzoyl chloride (Entry 5, Table 5.2; solution F/Br ratio is 3). These experiments illustrate that the ratio of bromine and fluorine in mixed monolayers can not simply be controlled by reacting monofunctional SAMs with mixtures of acid chlorides or substituted alkynes.

Table 5.2 XPS Data for Control Experiments

	Surface	Reactant	Br/N	F/N	F/Br
1		i. ii.	0.004	1.03	258
2		i. ii	0.89	0	0
3			-	0.09 ± 0.03	9.5
4[a]			2.3	0.24	9.5
5[b]			0.12	0.82	7.0

[a]1:1 molar ratio of the two acid chlorides [b]1:1 molar ratio of the two alkynes

To confirm the structural changes of the azides and amines after undergoing their respective reactions, infrared absorbance experiments were performed on powdered silica using the reactants shown in Table 5.1 in a similar manner as the silica-coated wafers used in the XPS experiments. In all IR absorbance spectra, a broad absorption was observed from 2800 to 3700 cm^{-1} attributed to water and H-bonded silanol.[32,33] For the benzyl azide- and propyl azide-modified powdered silica, the intense absorption peak at 2107 cm^{-1}, characteristic of the azide stretch, confirmed the attachment of the azides (Figure 5.2A, blue traces). In general, this peak disappeared after reaction with alkynes, indicating quantitative conversion to the triazole product. The one exception was the reaction of the aliphatic alkyne, 2,2,2-trifluoroethyl heptynoate with propyl azide-modified silica (Figure 5.2A (ii), black trace), where the azide peak was diminished but still observable. However, for both azide samples, a new peak appeared at 1740 cm^{-1} after reaction with this ester-substituted alkyne, confirming the presence of the carbonyl (C=O stretch, Figure 5.2A, black traces). Similarly new peaks were visible in the IR after reaction with the aromatic alkyne, p-trifluoromethylphenyl acetylene. Specifically, a new peak appeared at 1328 cm^{-1} attributed to the CF_3 anti-symmetric stretching vibration mode of the aromatic 1,4-isomer (Figure 5.2A, red traces).[34]

The reactivity of amine-modified silica with acid chlorides was similarly explored using changes in the IR absorbance spectra. After reaction of the amino silica and either the aliphatic or aromatic acid chloride, a new band at 1653 cm^{-1} appeared (corresponding to the C=O), confirming the formation of amide groups
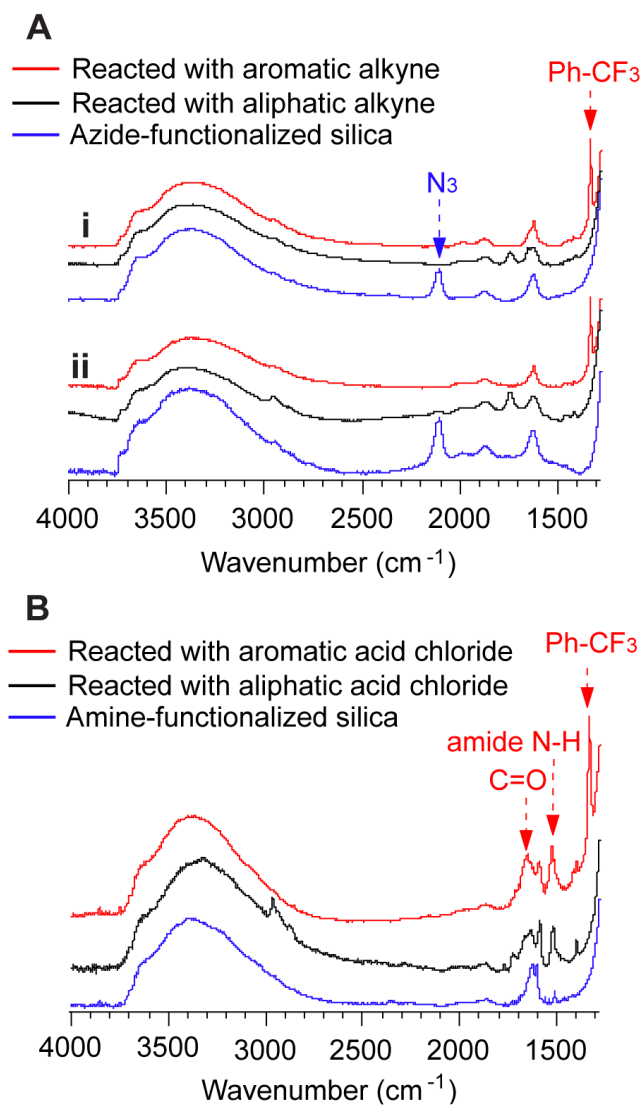
Figure 5.2 IR absorption spectra of powdered silica modified with: A) (i) propyl azido silane and (ii) benzyl azido silane, before (blue) and after reaction with an aromatic alkyne (red) or an aliphatic alkyne (black). B) phenylamino silane before (blue) and after reaction with an aromatic acid chloride (red) and an aliphatic acid chloride (black).

(Figure 5.2B, red trace). This band overlapped with the band at ~1630 cm^{-1} present for both the amine- and amide-modified silica that is attributed to the vibration of the adsorbed water on silica.[35] The peak at 1329 cm^{-1} corresponding

168

to the aromatic CF_3 on the substituted benzoyl chloride was also visible after amide formation.[34] In addition to confirming the structural changes associated with forming and reacting these SAMS, the high reactivity observed for the modified silica powder suggested that our strategy is amenable to functionalizing porous materials, with potential uses in multicomponent catalyst[10] or therapeutic[2] applications requiring high surface area materials.

5.2.3 Synthesis and Reactivity of Bifunctional SAMs

We next synthesized mixed monolayers from mixtures of azido and amino trimethoxysilanes with solution mole ratios of 1:1 and 5:1, respectively. For the benzyl azide system, the resulting mixed monolayers exhibited contact angles with water of 55 ± 1° for the 1:1 mixture and 58 ± 1° for the 5:1 mixture, in between the values for the corresponding monofunctional SAMs (Figure 5.3, table; see Figure 5.4 for characterization of propyl azide-amine SAMs). To verify that the surface azide/amine ratio increased with increasing amounts of azide trimethoxysilane in solution, we reacted the azide in these mixed monolayers with alkyne-substituted triethyleneglycol (TEG). The resulting AFM images are shown in Figure 5.3. The surface roughness exhibited by the root mean square (RMS) roughness values for the mixed monolayers after reaction with TEG increased from 1.07 nm to 1.53 nm with increasing amounts of azide in solution. This increase in roughness can be explained by the reaction of the long-chain alkyne with the surface-bound azides (Figure 5.3 A-D). Additionally, the correlation between surface roughness and the solution fraction of azido trimethoxysilane is

consistent with an increase in the amount of azide in the monolayer. Differences in hydrophilicity of the SAMs were also used to characterize the mixed monolayers. The water contact angle of the benzyl azide SAM decreased markedly from 60.7 ± 0.9° to 36 ± 2° upon incorporating the hydrophilic TEG chain. For the mixed monolayer, the trend in contact angle also confirmed that increasing the azide content led to greater incorporation of the hydrophilic TEG group (Figure 5.3, table). After establishing that we had successfully synthesized mixed monolayers with varying azide ratios, one question that remained was how closely the azide/amine surface ratio matched the ratio of azide and amine trimethoxysilanes in solution. To correlate the solution and surface composition, we took advantage of the signature double peak in the N-1s region of the XPS spectrum that corresponds to the azide (Figure 5.1B and C).[36] The distinctive two peaks and the unique position of the smaller peak at 405 eV provide a handle for characterizing the amount of azide in our mixed monolayers. Fitting the high-resolution N1s scan to two Gaussian peaks resulted in a large peak centered at 401 eV and a smaller peak centered at 405 eV for both azido SAMs. Interestingly, the peak area ratios differed for the two azido SAMs; the benzyl azido SAM exhibited a peak ratio of 3.07 ± 0.07 and the propyl azido SAM, a ratio of 4.1 ± 1. The different ratios for the two substituted azides suggest that the oxidation state of the azide nitrogen atoms depends on azide substitution, which is consistent with different resonant contributions for the propyl and benzyl azides.

Before TEG

A Benzyl Azide (BnAz)

RMS Roughness: 119 pm

B Amine (Am)

RMS Roughness: 130 pm

SAM *solution ratio	Water Contact Angle (°)	
	Before TEG	After TEG
Am	52±2	-
BnAz	60.7±0.9	36±2
5:1* BnAz:Am	58±1	42±2
1:1* BnAz:Am	55±1	50±2

After TEG

C BnAz

RMS Roughness: 1.53 nm

D 5:1 BnAz:Am

RMS Roughness: 1.21 nm

E 1:1 BnAz:Am

RMS Roughness: 1.07 nm

Figure 5.3 Tapping-mode atomic force microscopy images of SAMs before and after reaction with alkyne-substituted triethyleneglycol (TEG). A) Benzyl azido SAM. B) Amino SAM. C) Benzyl azido SAM reacted with TEG. D) Mixed monolayer synthesized from a 5:1 molar mixture of benzyl azido and amino trimethoxysilanes after reaction with TEG. E) Mixed monolayer synthesized from a 1:1 molar mixture of benzyl azido and amino trimethoxysilanes after reaction with TEG. Table: Contact angles of water droplets on SAMs. The contact angle decreases with increasing hydrophilicity of the monolayer.

171

SAM *solution ratio	Water Contact Angle (°)	
	Before TEG	After TEG
Am	52 ± 2	-
PrAz	62 ± 3	33.5 ± 0.9
5:1* PrAz:Am	56.6 ± 0.7	43 ± 2
1:1* PrAz:Am	55 ± 2	51 ± 1

A Propyl Azide (PrAz)
Before TEG
RMS Roughness: 113 pm

B Amine (Am)
RMS Roughness: 130 pm

C PrAz
After TEG
RMS Roughness: 1.82 nm

D 5:1 PrAz:Am
RMS Roughness: 1.58 nm

E 1:1 PrAz:Am
RMS Roughness: 1.25 nm
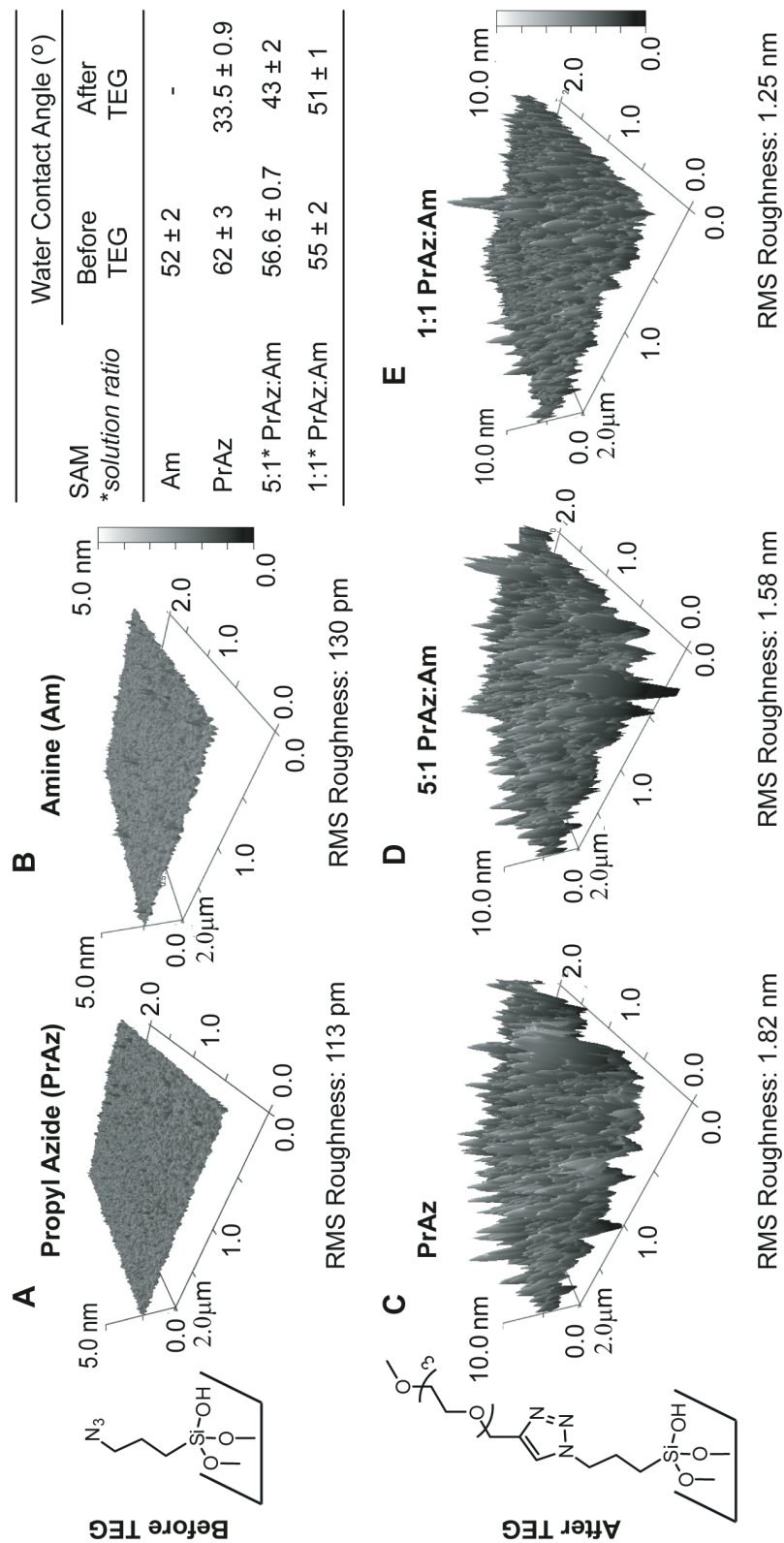
Figure 5.4 AFM images taken in taping mode for SAMs before (A-B) and after (C-E) reaction with triethylene glycol alkyne (TEG). A) Amino SAM. B) Propyl azido SAM. C) Propyl azido SAM reacted with TEG. E) Mixed monolayer synthesized from a 1:1 molar ratio of propyl azido and amino SAMs (the error indicates the standard deviation of measured values) before and after reaction with the hydrophilic TEG.
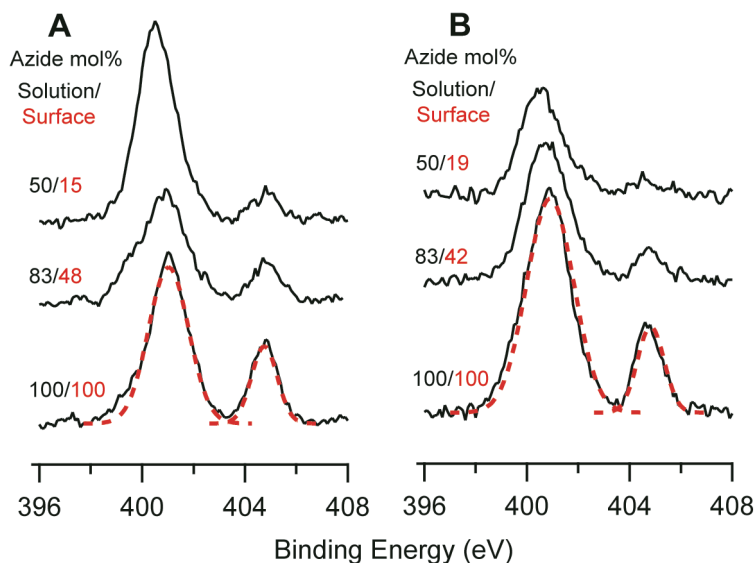
Figure 5.5 N1s high-resolution scans of **A)** benzyl azide-amine and **B)** propyl azide-amine mixed monolayers synthesized from solutions with varying mol% azide (total [trimethoxysilane] = 3.0 mM). By fitting each spectrum to two Gaussian peaks (red dashed lines) and comparing the peak ratios of the mixed and monofunctional azido SAMs, the mole percent of azide in each mixed monolayer was determined.

We next synthesized mixed monolayers from mixtures of azido and amino trimethoxysilanes with solution mole ratios of 1:1 and 5:1, respectively. For the benzyl azide system, the resulting mixed monolayers exhibited contact angles with water of 55 ± 1° for the 1:1 mixture and 58 ± 1° for the 5:1 mixture, in between the values for the corresponding monofunctional SAMs (Figure 5.3, table; see Figure 5.4 for characterization of propyl azide-amine SAMs). To verify that the surface azide/amine ratio increased with increasing amounts of azide trimethoxysilane in solution, we reacted the azide in these mixed monolayers with alkyne-substituted triethyleneglycol (TEG). The resulting AFM images are shown in Figure 5.3. The surface roughness exhibited by the root mean square (RMS)

roughness values for the mixed monolayers after reaction with TEG increased from 1.07 nm to 1.53 nm with increasing amounts of azide in solution. This increase in roughness can be explained by the reaction of the long-chain alkyne with the surface-bound azides (Figure 5.3 A-D). Additionally, the correlation between surface roughness and the solution fraction of azido trimethoxysilane is consistent with an increase in the amount of azide in the monolayer. Differences in hydrophilicity of the SAMs were also used to characterize the mixed monolayers. The water contact angle of the benzyl azide SAM decreased markedly from 60.7 ± 0.9° to 36 ± 2° upon incorporating the hydrophilic TEG chain. For the mixed monolayer, the trend in contact angle also confirmed that increasing the azide content led to greater incorporation of the hydrophilic TEG group (Figure 5.3, table).

5.2.4 Controlling the Ratio of the Functional Groups on SAMs

After establishing that we had successfully synthesized mixed monolayers with varying azide ratios, one question that remained was how closely the azide/amine surface ratio matched the ratio of azide and amine trimethoxysilanes in solution. To correlate the solution and surface composition, we took advantage of the signature double peak in the N-1s region of the XPS spectrum that corresponds to the azide (Figure 5.1B and C).[36] The distinctive two peaks and the unique position of the smaller peak at 405 eV provide a handle for characterizing the amount of azide in our mixed monolayers. Fitting the high-resolution N1s scan to two Gaussian peaks resulted in a large peak centered at 401 eV and a

smaller peak centered at 405 eV for both azido SAMs. Interestingly, the peak area ratios differed for the two azido SAMs; the benzyl azido SAM exhibited a peak ratio of 3.07 ± 0.07 and the propyl azido SAM, a ratio of 4.1 ± 1. The different ratios for the two substituted azides suggest that the oxidation state of the azide nitrogen atoms depends on azide substitution, which is consistent with different resonant contributions for the propyl and benzyl azides.
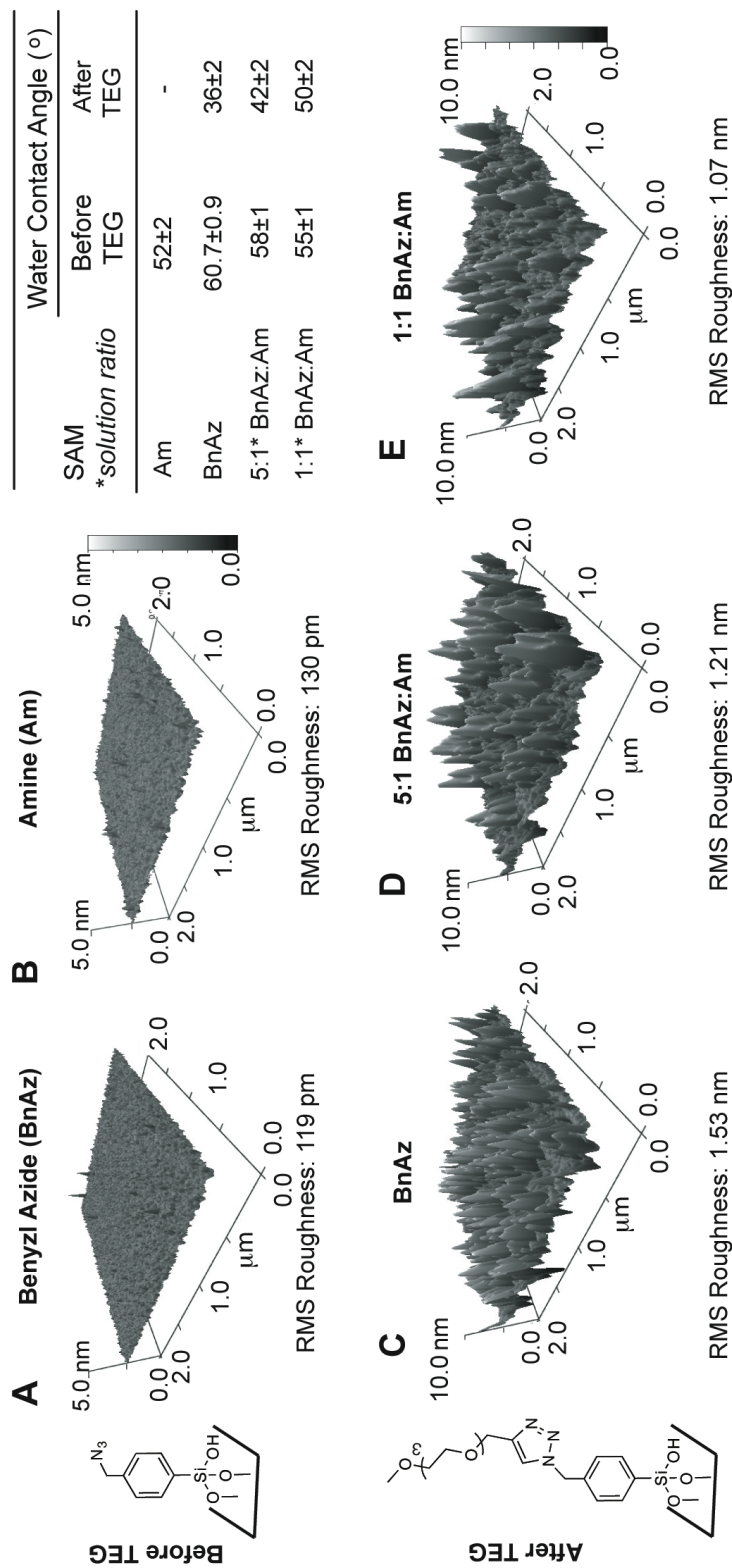
Next, we measured the ratio of the peak areas from the higher solution XPS data of monolayers synthesized from 1:1 molar mixtures of the azido and amino trimethoxysilanes. As expected, the 401 to 405 eV peak ratios were much greater than that of the monofunctional azido SAMs, owing to overlap of the amine and azide signals at 401 eV. Specifically, peak area ratios of 13 ± 2 and 12 ± 1 were observed for the benzyl azide-amine and the propyl azide-amine SAMs, respectively. Using these values, the area of the peak at 405 eV, and the peak ratio for the corresponding monofunctional azido SAM, the relative amount of azide was determined for each mixed monolayer. To illustrate, the following equation was used to determine the azide/amine ratio for the benzyl azide-amine mixed monolayers

$$\frac{\text{benzyl azide}}{\text{amine}} = \frac{(1+3.07)\text{peak area}_{405eV}}{3} \times \frac{1}{\text{peak area}_{401eV} - (\text{peak area}_{405eV} \times 3.07)}$$

We also attempted a three-peak fit of the XPS data to resolve the amine and azide contributions at 401 eV, but the similarities in the peak positions (400.8, 400.9, and 401.2 eV for the amine, propyl azide, and benzyl azide, respectively) led to azide/amine values that were inconsistent with the peak area at 405 eV.

Table 5.3 The Azide/Amine Surface Ratio for Mixed Monolayers Assembled in Different Solvents

Solution Azide Mol%	Toluene		Hexane	
	N1s XPS Ratio[a]	Surface Azide Mol%	N1s XPS Ratio[a]	Surface Azide Mol%
83% BnAz	4.3±0.2	52±6	4.5 ± 0.3	48 ± 4
50% BnAz	13.3 ± 0.3	12±3	23 ± 11	9 ± 5
83% PrAz	6.3 ± 0.2	44±2	5.1 ± 0.1	63 ± 2
50% PrAz	12.2 ± 0.9	18±2	10.0 ± 0.9	23 ± 3

[a]Ratio represents the XPS peak areas for signals centered at 401 eV and 405 eV, respectively.

The peak ratios reveal that only 12 ± 3 mol% azide has been incorporated into the monolayer for a 1:1 molar mixture of benzyl azido and amino trimethoxysilane (50 mol% benzyl azide in solution) (Figure 5.5A, Table 5.3). Similarly, the propyl azide-amine mixed monolayer exhibited a much smaller amount of azide on the surface compared with the solution composition (18 ± 2 vs 50 mol%, respectively, Figure 5.5B). From these results, we conclude that the solution ratio differs substantially from the surface ratio. To achieve 52 mol % of azide in the benzyl azide-amine mixed monolayer, benzyl azido trimethoxysilane must be five times more concentrated than aminophenyl trimethoxysilane in solution (i.e., 83 mol% azide). For the propyl azide-amine mixed SAM, a solution azide/amine ratio of 8 was needed to achieve 53 mol% of the propyl azide in the mixed monolayer. (Figure 5.6) These results reveal that the composition of azide-amine mixed monolayers varies significantly from the ratio of silanes in solution. Although it has long been recognized that surface reactivity and solubility[37] can influence surface ratios in mixed monolayer systems[20] because of the difficulty in

176

quantifying surface ratios, the solution ratio is often used to interpret the structure and behavior of the mixed monolayer.[7,14] In our mixed monolayer system, such an assumption would introduce significant error to the interpretation because of the disproportionate amount of amine groups versus azides.
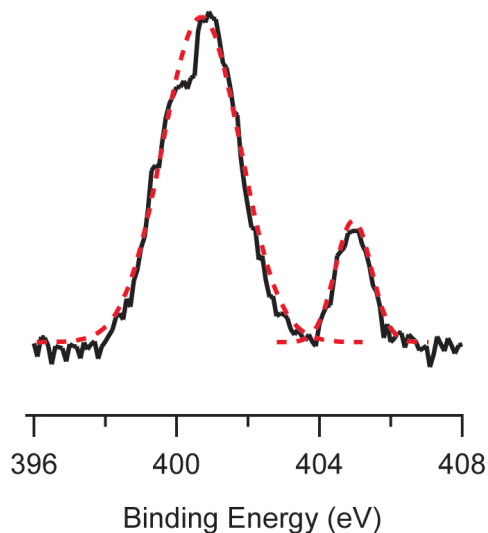
Figure 5.6 N1s high resolution XPS scan of the propyl azide-amine mixed monolayer synthesized from an 8:1 azide/amine trimethoxysilane solution (total concentration of trimethoxysilanes = 3 mM). Red dashed lines represent the peak fitting of the two N peaks at 401 eV and 405 eV. Based on the analysis of the peak ratio described in the main text, the azide/amine ratio was determined to be 1.1.

5.2.5 Effects of Solvent on Surface Ratio

One explanation for the larger amount of aminophenyl groups in our mixed monolayers is the ability of aminophenyl silanes to interact with the silica surface through hydrogen bonding and self-associate via pi stacking.[25] The former should enhance their presence at the interface and has been observed in flexible aminosilanes as the first step prior to surface reaction.[38] The latter has been

inferred from the well-ordered monolayers that result from phenylamino silanes.[25] Additionally, the ability of amines to act as base catalysts capable of cross-linking trimethoxysilanes or condensing them with surface silanol groups could also increase the incorporation of aminosilanes into the monolayer, particularly if they are self-associating.[38,39] In our mixed monolayers, the azide/amine surface ratio was similar regardless of the azide structure, which is consistent with the proposed surface concentration enhancement of the amines due to hydrogen bonding. Moreover, the similarity suggested that neither azide interacted strongly with the phenylamine, which was surprising for the benzylazido silane. We reasoned that toluene might minimize any pi-stacking interactions between the benzyl azides and phenylamines, thereby impacting their surface ratio. Therefore, we repeated the mixed monolayer experiments in hexane. Interestingly, changing the solvent from toluene to hexane had no effect on the benzyl azide/amine surface ratio, suggesting that pi stacking of the solvent did not play a substantial role. To see whether the same held true for the propylazide-amine mixed monolayer, we also measured the role of solvent on its azide/amine surface ratio. For this system, a greater amount of the propyl azide was observed for monolayers prepared in hexane rather than toluene (63 ± 2 vs 44 ± 2 mol% azide, respectively). We expected hydrogen bonding between the aminosilane and the silica to be enhanced by the hexane; instead the decrease in amine content indicated either enhanced reactivity of propylazide in hexane or a change in monolayer stability. Kang and colleagues observed that the more polar of two surface reactive species tended to make up a larger component in the mixed

178

monolayer, despite the solution ratio. Yet the difference between the surface and solution ratios systematically decreased with decreasing solvent polarity.[21] The resulting decrease in polar content of the propyl azide-amine monolayerwas thus attributed to a change in monolayer stability with solvent polarity. For our benzyl azide-amine mixed monolayer, the polarity of the benzyl azides should be closer to that of the phenylamines, minimizing the effect of solvent polarity on surface ratio. Future work will address how the solvent influences the spatial distribution of the azides and amines,[4] which might provide more clues as to the origin of monolayer stability for these mixed SAMs.

5.2.6 Functionalization of Orthogonally Reactive SAMs

A key aspect of the orthogonally reactive-SAM strategy is that the ratio of azides to amines will determine the ratio of functional groups that are subsequently attached. To characterize the ratio of the triazole and amide groups that result from reacting the azides and amines, respectively, we once again turned to XPS. Figure 5.7A illustrates the functionalization of benzyl azide-amine SAMs with p-bromobenzoyl chloride, followed by the fluorine-labeled alkyne used in previous experiments. As a reference, the Br/N ratio for the monofunctional amino SAM after reaction with p-bromobenzoyl chloride yielded a ratio of 0.87 ± 0.02, indicating that the maximum conversion was only $87 \pm 2\%$ with this reactant (Table 5.1, entry 2). Taking this slightly lower yield into consideration, the high resolution N1s scan before functionalization (Figure 5.7B). More importantly, the
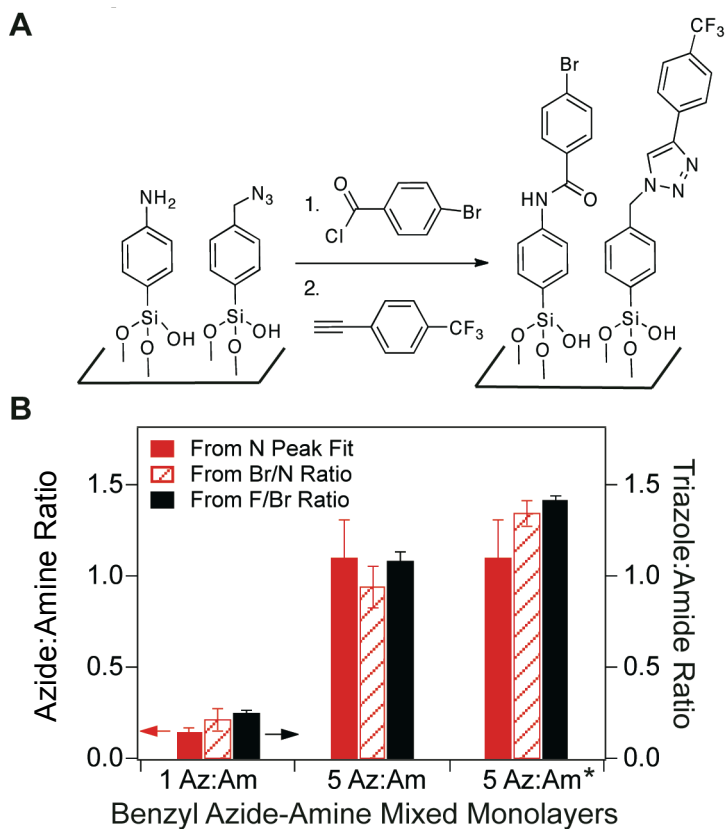
Figure 5.7 A) Functionalization of orthogonally reactive SAMs with (1) Br-labeled acid chloride followed by (2) CF$_3$-labeled alkyne. B) Surface ratios determined from the XPS data of mixed monolayers prepared from 1:1 or 5:1 molar mixtures of azido and amino trimethoxysilane (*1 BnAz:Am* and *5 BnAz:Am*, respectively). The azide/amine ratio was determined from the Br/N ratio (*Br/N Ratio*) and the N peak ratio prior to functionalization *(N Peak Fit)*. The triazole:amide product ratios were determined from the F/Br ratio (*F/Br Ratio*). *Denotes reversal of reaction sequence, i.e., the mixed monolayer was reacted first with the alkyne and then the acid chloride.

ratio of the triazole and amide products determined from the F/Br ratio was very consistent with the azide/amine surface ratios, indicating that the ratio of orthogonally reactive groups dictated the amount of surface products. In contrast, efforts to synthesize 1:1 CF$_3$ and Br mixed monolayers from monofunctional SAMs led to CF$_3$/Br surface ratios much greater than one. Specifically, when a

1:1 mixture of CF$_3$- and Br-labeled acid chlorides was reacted with an amino SAM, the resulting CF$_3$/Br surface ratio was 3.2 (Figure 5.8A). Similarly, a 1:1 mixture of CF$_3$- and Br-labeled alkynes reacted with a benzyl azido SAM led to CF$_3$/Br ratios of 2.3 (Figure 5.8B). The substantial difference between the observed ratios and the desired ratio of one emphasizes the difficulty in controlling surface ratios with post-SAM modification strategies using monofunctional SAMs. Once again, these experiments highlight the utility of orthogonally reactive SAMs in controlling surface ratios.
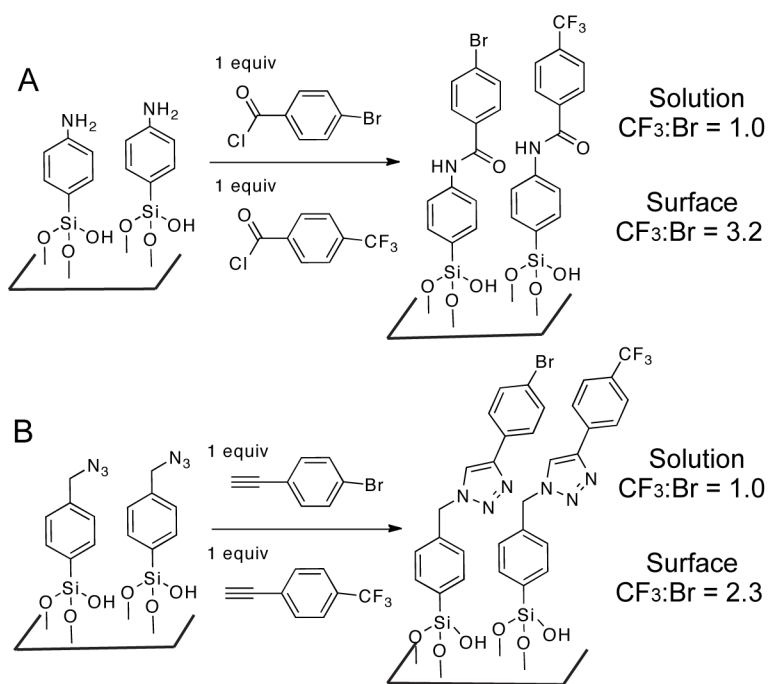
Figure 5.8 A) A monofunctional amino SAM reacted with a 1:1 molar mixture of 4-trifluoromethyl- and 4-bromo-benzoyl chloride. The resulting CF$_3$:Br surface ratio was more than three times higher than the solution ratio. B) A monofunctional benzyl azido SAM reacted with a 1:1 molar mixture of 4-trifluoromethyl- and 4-bromo-phenylethyne. The resulting CF$_3$:Br surface ratio was more than twice the solution ratio. These experiments indicate that generating mixed monolayers post SAM formation does not improve the correlation between the solution and surface ratio.

We did, however, observe some sensitivity in our orthogonally reactive SAM strategy to the sequence of functionalization steps. When we performed the cycloaddition reaction first and the acylation second, the amount of surface bromine, quantifying the efficiency of amide formation, decreased (Br/N of 0.17 ± 0.01 vs 0.23 ± 0.02 for samples acylated second and first, respectively). The smaller Br/N ratio led to a larger calculated azide/amine ratio (Figure 5.7B, Br/N ratio: 5Az:Am*). Instead, the lack of bromine is most likely due to lower conversion of the amines to the bromine labeled amides. This lower conversion suggests that amide formation is sensitive to the local environment around the amine. The formation of the triazoles might sterically block the amine groups, preventing them from reacting with the p-bromobenzoyl chloride. In contrast, the amount of fluorine-labeled alkyne was similar whether the click reaction happened first or second (F/N of 0.79 ± 0.04 vs 0.78 ± 0.05, respectively). These results suggest that the alkyne-azide click reaction is not affected by changes in the local environment around the azide. This similarity in conversion indicates that the high reactivity of the azido monolayer with this alkyne can compensate for difficulty in accessing the surface sites. Future work will explore other reactions orthogonal to the click reaction that are more tolerant of reaction sequence than acylation by acid chlorides. For example, the reaction of thiols with maleimides or other olefinic electrophiles should be orthogonally reactive to the cycloaddition reaction and perhaps less sensitive to the order of reaction.[1]

5.3 Concluding Remarks

Mixed monolayers represent an important avenue for combining functions in materials and in model systems.[4,16] In the field of self-assembly, many early reports on SAMs demonstrated that solvent and interactions among assembling molecules could influence the resulting mixed monolayer composition.[20,37] As a result, the surface ratios do not often reflect the composition of the assembly solution. Despite this long-held wisdom in SAM formation, the difference in surface versus solution composition is often overlooked in bifunctional monolayer systems because of the difficulty in characterizing the functional group ratio. The challenge in identifying surface ratios underscores the need for general strategies, like orthogonally reactive SAMs, that provide a well-defined starting point for making complex mixed monolayers of controlled composition.

We have synthesized two azide-substituted trimethoxysilanes that can be directly assembled with aminophenyl trimethoxysilane to yield azide-amine mixed monolayers. Using XPS, we have demonstrated how to quantify the amount of orthogonally reactive azides and amines in our monolayers and tune their surface ratio. Through subsequent cycloaddition and acylation reactions, this azide-amine mixed monolayer can be used to anchor combinations of functional groups to silica that are not necessarily amenable to silane chemistry. Moreover, by controlling the amine/azide ratio in the SAM, the ratio of subsequent groups reacted with the azides and amines can be controlled independently of their surface reactivities. The many examples of surface functionalization reactions based on click chemistry or amine modification indicate that there are many

combinations of molecules available for forming mixed monolayers with this strategy.[16] The high reactivity observed for the azide and amine groups with different substituted reactive partners suggests that this platform should be general for attaching a wide variety of molecules. Furthermore, this strategy of making mixed monolayers on silica containing orthogonally reactive groups should work with other reactive pairs besides azides and amines; for example, azides or alkynes should be orthogonally reactive with other nucleophiles besides amines like thiols or other electrophilic groups besides acid chlorides like maleimides, epoxides and N-hydroxysuccinimidyl esters.[1] Finally, our strategy for characterizing orthogonally reactive mixed monolayers containing azides should be accessible to other substrates besides silica as well as other reactive group pairings besides azides and amines.[14]

5.4 Experimental

5.4.1 Materials

3-{2-[2-(2-Methoxy-ethoxy)-ethoxy]-ethoxy}-propyne[22] was synthesized following a literature procedure, as was 4-(trifluoromethyl)phenyl acetylene, which was synthesized from the commercially available trimethylsilyl-protected analog.[23] All other reagents or solvents were purchased from Aldrich, VWR, Fisher, or Gelest and used without further purification. Silica gel (70-230 mesh, 100 Å) was purchased from Sigma-Aldrich, and silicon (100) wafers (prime grade, 0.5 mm thickness) were purchased from Fluoroware.

5.4.2 General Procedure for Preparing Azide-Substituted Trimethoxysilanes

The following procedure was modified from a procedure noted in a patent application for synthesizing propyl azido trimethoxysilane (Scheme 5.2).[24] NaN_3 (1.34 g, 20.7 mmol) was weighed in a 50 mL Schlenk flask containing a magnetic stir bar. The flask was placed under nitrogen, followed by the addition of dimethylformamide (DMF) (6 mL). After stirring for 15 min, chloride-substituted benzyl or propyl trimethoxysilane (10.2 mmol) was added to the suspension via syringe. The reaction flask was then equipped with a water condenser and allowed to stir for 48 h at 70º C under N_2. After the reaction was cooled to room temperature, dry hexane (10 mL) was cannula-transferred to the reaction mixture. This biphasic mixture was stirred for 2 h, then allowed to settle for 1 h. At this point, the upper hexane layer was decanted via cannula to another 25 mL Schlenk flask under N_2, and the hexane was removed under reduced pressure on a Schlenk line to yield the desired product as a colorless liquid. Because of the possible explosive nature of the hydrolyzed silyl azides, dry toluene (3-5 mL) was immediately transferred to the product, which was thereafter kept as a solution under nitrogen. The concentration and yield were calculated from the ^{1}H NMR data for a sample made of 50 μL of the reaction mixture using 10 μL of ethyl acetate in acetone-d_6 as an internal standard. No chloride starting material was visible in the ^{1}H NMR.

a) 4-(Trimethoxysilyl)benzyl Azide

Final concentration in toluene: 0.54-0.96 M. Yield: 48.2%. ^{1}H NMR (acetone-d$_6$): δ 3.60 (s, 9H, CH_3-OSi), 4.48 (s, 2H, CH_2-N$_3$), 7.56 (dd, 4H,Ar-H).

IR cm^{-1}: 2944.4, 2842.1, 2099.7, 1464.6, 1414.2, 1345.0, 1277.9, 1242.9, 1193.1, 1089.0.

b) 3-(Trimethoxysilyl)propyl Azide

Final concentration in toluene: 0.96-1.83M.Yield 73.1%. ^{1}H NMR (acetone-d$_6$): δ 0.69 (t, 2H,-CH_2-CH2-CH$_2$-N$_3$), 1.68 (m, 2H, -CH_2-CH$_2$-N$_3$), 3.28 (t, 2H, -CH_2-N$_3$), 3.55 (s, 9H, CH_3-OSi). IR cm^{-1}: 2944.4, 2842.5, 2100.9, 1605.5, 1455.3, 1399.7, 1342.2, 1277.4, 1248.6, 193.0, 1124.4, 1085.9.

5.4.3 Synthesis of 4-Bromobenzoyl Chloride

4-Bromobenzoic acid (2.02 g, 10.1 mmol) and thionyl chloride (5.0 mL, 69 mmol) were combined in a 25mL round-bottomed flask equipped with a stir bar and a water condenser, at which point the mixture was refluxed for 5 h. After cooling to room temperature, the thionyl chloride was removed under reduced pressure, and the crude product was purified by vacuum distillation (50-52 ºC, 100 mTorr) to yield a white solid (1.66 g, 7.06 mmol, 70%). mp 38.8-40.3 ºC (matched with manufacturer (TCI America) data). ^{1}H NMR (CDCl$_3$): δ 7.67 (d, 2H, Ar-H), 7.98 (d, 2H, Ar-H). ^{13}C NMR (CDCl$_3$): δ 131.31 (s, ArC-COCl), 132.27 (s, ArC-Br), 132.54 (s, ArC), 132.76 (s, ArC), 167.79 (s, -COCl). High-resolution EI-MS (M$^{+\bullet}$): 219.91139.

5.4.4 Synthesis of 4,4,4-Trifluorobutanoyl Chloride

4,4,4-Trifluorobutanoic acid (6.88 g, 4.85 mmol) was taken in a 25 mL round-bottomed flask and dissolved in the minimum volume of dichloromethane (DCM) (~3.0 mL). A solution of oxalyl chloride in DCM (2.0 M, 3.0 mL, 6.0

mmol) was added slowly via syringe; then, the reaction mixture was placed in an ice bath. A catalytic amount of DMF (1 drop) was added, and the reaction was stirred for 15 min. It was then allowed to come to room temperature and stirred for an additional 6 h. DCM and excess oxalyl chloride were removed slowly under moderately reduced pressure to avoid evaporation of the product. We then purified the by collecting the acid chloride (colorless liquid) in a liquid-nitrogen cooled trap under reduced pressure (0.459 g, 2.86 mmol, 59%). ^{1}H NMR (CDCl$_3$): δ 2.54 (m, 2H, -CH_2CF$_3$), 3.19 (t, 2H, -CH_2COCl). ^{13}C NMR (CDCl$_3$): δ 29.37 (q, -CH$_2$-CF$_3$), 39.59 (q, -CH$_2$-COCl), 125.78 (q, -CF3), 171.75 (s, -COCl). IR cm^{-1}: 2917.4, 2849.1, 1829.7, 1446.3, 1424.3, 127.9, 1232.3, 1143.5, 1114.5, 1063.5, 1008.1, 985.1.

5.4.5 Synthesis of 2,2,2-Trifluoroethyl Hept-6-ynoate

Hept-6-ynoic acid (0.996 g, 7.89 mmol) was weighed into a 25-mL round bottom flask and dissolved in the minimum volume of DCM (4.0 mL). An oxalyl chloride solution in DCM (2.0 M, 5.0 mL, 10.0 mmol) was added slowly via syringe and then the reaction mixture was placed in an ice bath. After cooling the reaction mixture to 0 ºC, DMF (1 drop) was added and immediate effervescence of gas was observed. After stirring the reaction mixture in an ice bath for 15 minutes, it was allowed to come to room temperature and stirred for 2 hours. DCM and excess oxalyl chloride were then rotovaped off, and the reddish brown crude product was used in the next step. ^{1}H NMR (CDCl$_3$): δ 1.55-1.63 (m, 2H, CH≡C-CH$_2$-CH_2-), 1.81-1.88 (m, 2H, CH≡C-CH$_2$-CH$_2$-CH_2-), 1.97 (t, 1H,

HC≡C*H*₂C-), 2.21-2.25 (d of t, 2H, HC≡C-C*H*₂-), 2.93 (t, 2H, C*H*₂-CO).

Hept-6-ynoyl chloride was taken into a 25-mL flask and dissolved in DCM (4 mL). 2,2,2-Trifluoroethanol (0.7 mL, 9.1 mmol) and triethylamine (TEA, 0.9 mL, 9.0 mmol) were dissolved in DCM (3 mL) and added to the flask containing the acid chloride. The resulting mixture was stirred for 4 hours at room temperature. The reaction mixture was then diluted with DCM (5 mL), washed with water (5 × 3 mL), dried over Na₂SO₄, and filtered into a 25-mL round bottom flask. The solvent and any remaining trifluoroethanol starting material were removed from the filtrate by rotary evaporation. The crude product was purified by vacuum distillation (65-70 ℃, 48 mTorr) to yield a clear oil (1.17 g, 5.55 mmol; overall yield in two steps 70.3%). ^{1}H NMR (CDCl₃): δ 1.56-1.58 (m, 2H, CH≡C-CH₂-C*H*₂-), 1.76-1.79 (m, 2H, CH≡C-CH₂-CH₂-C*H*₂-), 1.95 (t, 1H, C*H*≡CCH₂-), 2.20-2.23 (d of t, 2H, CH≡C-C*H*₂-), 2.44 (t, 2H, C*H*₂-CO), 4.44-4.47 (q, 2H, O-C*H*₂CF₃). ^{13}C NMR (CDCl₃): δ 18.06 (s, 1C, CH≡C-*C*H₂-), 23.69 (s, 1C, CH≡C-CH₂-*C*H₂-), 27.62 (s, 1C, CH≡C-CH₂-CH₂-*C*H₂-), 33.07 (s, 1C, CH≡C-CH₂-CH₂-CH₂-*C*H₂-), 59.89-60.52 (q, 1C, *C*F₃-CH₂-), 68.78 (s, 1C, *C*H≡C-), 83.65 (s, 1C, CH≡*C*-), 120.65-125.37 (q, 1C, *C*F₃-CH₂-), 171.72 (s, 1C, *C*=O). IR cm^{-1}: 3311.1, 2928.6, 2869.9, 2119.3, 1760.9, 1414.6, 1283.1, 1171.3, 1141.5, 1083.3, 978.4.

5.4.6 Substrate Cleaning Procedure

Silicon wafers containing a native oxide layer were used as the substrates for the XPS and AFM measurements. Glass slides (Fisher, Microscope Slides)

were used for the contact angle measurements. Prior to surface functionalization, both types of samples were cleaned with methanol (~15 mL) followed by drying in an oven for 10 min at 90 ± 5 °C. The cleaned wafers were reacted with "piranha solution" (3:1 mixture of sulfuric acid and 30% hydrogen peroxide) in a glass beaker to make the surface rich with hydroxyl groups.[25] (Caution: Piranha solution reacts explosively with organic materials, so it should not be combined with any organic compounds or solvents. Use caution.) The beaker containing the samples was rinsed copiously with deionized water (5 x 100 mL), the individual samples were then each rinsed with a stream of millipore water (100 mL), sonicated in milipore water (100 mL) for 10 minutes, and blown dry with a stream of nitrogen gas. The substrates thus obtained were placed in an oven for 30 min (90 ± 5 °C). In some cases the silicon wafers were next cleaned using a reactive ion etcher (μEtch RIE, Plasma Lab) with oxygen as reactive gas in a radio frequency (RF)-induced plasma to remove residual fluorine from the packing material. Process pressure was 500 mTorr and process time was 1 min for plasma cleaning.

5.4.7 Self-Assembled Monolayer Formation on Silica Surfaces

Cleaned samples were rinsed with a stream of methanol (15 mL), a mixture of methanol and toluene (1:1 v/v, 15 mL), and finally a stream of toluene (15 mL), and then immersed in 3 mM solution of the trimethoxysilane in dry toluene with 0.1 % water (v/v) for 4 h. The same protocol was used for SAM formation in hexane, with hexane substituted for toluene in the above steps. To

make the orthogonally reactive self-assembled monolayers, different proportions of amino and azido trimethoxysilanes were combined to reach a total concentration of 3 mM trimethoxysilane. After the 4 h of reaction time, the samples were rinsed thoroughly with toluene (15 mL), sonicated for one minute each in toluene (15 mL), toluene/methanol (15 mL) and methanol (15 mL) and then blown dry with a stream of nitrogen gas. The samples were either used immediately in a subsequent reaction or stored under vacuum.

5.4.8 Modification of Powdered Silica for the IR Absorbance Experiments

SiO_2 powder (0.5 g, 70-230 mesh, 100Å) was added to a 25-mL flask containing a solution of the respective trimethoxysilane in toluene (5 mL, 50 mM). This slurry was stirred for 4 hours at room temperature. The higher concentration of trimethoxysilane was used because of the high surface area of the silica gel (surface area = 300 m^2/g). After reaction, the functionalized silica powder was filtered in a Buchner funnel to remove the filtrate. The powder was then washed with toluene (4 x 15 mL) and methanol (4 x 15 mL). Finally, the powder was annealed for 30 minutes in an oven at 90 ± 5 ºC. The subsequent acylation or [3+2] cycloaddition reaction was performed on the functionalized powder using the same procedure as the silica surfaces with 0.1 g powdered silica samples.

5.4.9 General Method for Acylation of Amino SAMs

The acid chloride (0.5 mmol) was dissolved in a 20 mL vial in acetonitrile

(ACN) (5 mL), followed by the addition of triethylamine (0.05 mL, 0.36 mmol). Freshly prepared amino SAMs were immersed in the vial containing the reaction mixture, which was then capped and allowed to react overnight. The acylated amino SAMs were then taken out of the vial and rinsed with ACN (10 mL) and toluene (10 mL), followed by 1 min sonication in toluene (10 mL) and methanol (10 mL) each and then blown dry with a stream of nitrogen gas.

5.4.10 General Method for [3 + 2] Cycloaddition Reaction of Alkynes with Azido SAMs

The following procedure was used for all of the alkynes except for the reaction of benzyl azido SAM with propargyl substituted triethyleneglycol monomethyl ether (TEG-alkyne). Copper sulfate (6.2 mg, 0.025 mmol) and ascorbic acid (8.8 mg, 0.050 mmol) were transferred into a 20-mL vial and dissolved in DMF (5 mL) by sonication. The alkyne (0.25 mmol) was dissolved in that solution at which point freshly prepared azido

SAMs were immediately immersed into the vial, which was then capped, wrapped in foil, and allowed to react overnight. The reacted azido SAMs were then taken out of the vial and rinsed with DMF (10 mL) and toluene (10 mL) followed by sonication for 1 minute each in toluene (10 mL) and methanol (10 mL). Finally, the samples were blown dry with a stream of nitrogen and stored under vacuum.

5.4.11 [3+2] Cycloaddition of the Benzyl Azido SAM with TEG-Alkyne

AFM analysis suggested that different cycloaddition conditions were

required for the benzyl azido SAM with TEG-alkyne. Therefore, copper (I) iodide (9.5 mg, 0.050 mmol) and triethylamine (0.1 mL, 0.7 mmol) were transferred into a 20-mL vial containing water (2.5 mL) and methanol (2.5 mL). TEG-alkyne (0.05 g, 0.25 mmol) was dissolved in that solution and freshly prepared benzyl azido SAMs were immersed in the vial, which was then capped. The SAM sample was taken out of the vial after overnight reaction and rinsed with water (10 mL), methanol (10 mL), toluene (10 mL), and methanol (10 mL), followed by sonication in methanol (10 mL) for 1 minute. The samples were blown dry with nitrogen and stored under vacuum.

5.4.12 Bifunctional Modification of Orthogonally Reactive SAMs

The orthogonally reactive-SAMs were reacted via acylation and cycloaddition, sequentially, following the same modification procedures detailed above.

5.4.13 XPS Analysis

XPS measurements were performed on samples that had been prepared within the last four days using the AXIS ULTRA spectrometer (Kratos Analytical). The base pressure in the analytical chamber was lower than 3×10^{-8} Pa. The monochromatic Al Kα source (hν = 1486.6 eV) was used at a power of 210 W. The photoelectron exit angle was 90º and the incident angle was 35.3º from the plane of the surface. The analysis spot was 400 x 700 μm. The resolution of the instrument was 0.55 eV for Ag 3d and 0.70 eV for Au 4f peaks. Survey

scans were collected for binding energies from 1100 eV to 0 eV with an analyzer pass energy of 160 eV and a step of 0.35 eV. The high-resolution spectra were run with a pass-energy of 20 eV and a step of 0.1 eV. Relative sensitivity factors (RSF) for different elements were as follows: 1 for F (1s), 0.477 for N (1s), 0.955 for Br (3d). Only one set of XPS scans were performed on a given sample, therefore XPS analysis before and after surface reactions were performed on different samples.

5.4.14 AFM Measurements

AFM experiments were performed on samples no more than 2 days old using a MFP-3D (Asylum) operated in tapping mode with commercially available Si cantilevers (Olympus, 300 kHz frequency). The force constant of the cantilevers was 42 N/m. The oscillation frequency used for tapping mode was 310 ± 5 kHz.

5.4.15 Contact Angle

Contact angles of water were measured on samples that had been prepared within the last two days using a FTA200 (First Ten Angstroms) system for contact angle and drop shape analysis fitted with manufacturer software. Contact angles were determined from sessile water drops of 8.0-μL volume. For each type of surface characterized, the average of at least six contact angle measurements was determined from, at minimum, two separately prepared slide samples.

5.4.16 Calculation of Azide/Amine Ratio from N-Peak Fitting

The high-resolution N (1s) scan for the monofunctional azide and azide-amine mixed monolayers were analyzed using the multipeak fitting program in Igor Pro 6.05. Two Gaussian peaks, one centered at 401 eV and another at 405 eV resulted after fitting the N (1s) region of the high-resolution XPS spectrum. The peak areas were determined from the following equation:

$$\text{peak area} = \sqrt{\pi}\,(\text{amplitude} \times \text{width})$$

The calculated ratio of the 401/405 eV peak areas for the benzyl azido SAM was 3.07(7), while the corresponding peak ratio for the propyl azido SAM was found to be 4.1(1). Substituting these values and the peak areas calculated for the mixed monolayers, the azide:amine ratio was determined from the corresponding equation:

$$\frac{\text{benzyl azide}}{\text{amine}} = \frac{(1+3.07)\text{peak area}_{405eV}}{3} \times \frac{1}{\text{peak area}_{401eV} - (\text{peak area}_{405eV} \times 3.07)}$$

$$\frac{\text{propyl azide}}{\text{amine}} = \frac{(1+4.1)\text{peak area}_{405eV}}{3} \times \frac{1}{\text{peak area}_{401eV} - (\text{peak area}_{405eV} \times 4.1)}$$

For peak fitting, the peak center, width, and amplitude values were allowed to vary with the exception of the 1:1 propyl azide-amine sample. For this spectrum, the small peak at 405 eV was difficult to fit without holding any parameters. Therefore, a peak width of 0.74 eV was held for the smaller peak at 405 eV, because this value was generated for the peak at 405 eV from fitting both the monofunctional propyl azido SAM and the 5:1 propyl azide-amine SAM spectra.

5.4.17 Calculation of the Azide/Amine and Triazole/Amide Ratios

Atomic compositions of the surfaces were calculated from the elemental peak areas in the XPS spectra of the amine-azide mixed monolayers adjusted with their corresponding relative sensitivity factors (RSF). Specifically, the measured Br/N, and F/Br ratios were substituted into the following equations to determine the azide/amine and triazole/amide surface ratios.

$$\text{From Br/N ratio} \left(\text{assuming } 87\% \text{ conversion}\right): \frac{\text{azide}}{\text{amine}} = \frac{1 - (\text{Br/N})/0.87}{3 \times (\text{Br/N})/0.87}$$

$$\text{From F/Br ratio:} \frac{\text{azide}}{\text{amine}} = \frac{\text{F/Br}}{3}$$

5.5 References

(1)   Iha, R. K.; Wooley, K. L.; Nystrm, A. M.; Burke, D. J.; Kade, M. J.; Hawker, C. *J. Chem. Rev.* **2009**, 109, 5620–5686.

(2)   Ferrari, M. *Nat. Rev. Cancer* **2005**, 5, 161–171.

(3)   Kessler, D.; Nilles, K.; Theato, P. *J. Mater. Chem.* **2009**, 19, 8184–8189.

(4)   Onclin, S.; Ravoo, B. J.; Reinhoudt, D. N. *Angew. Chem., Int. Ed.* **2005**, 44, 6282–6304.

(5)   Mrksich, M.; Whitesides, G. M. *Trends in Biotechnol.* **1995**, 13, 228–235.

(6)   Patrie, S. M.; Mrksich, M. *Anal. Chem.* **2007**, 79, 5878–5887.

(7)   Frisk, M. L.; Tepp, W. H.; Johnson, E. A.; Beebe, D. J. *Anal. Chem.* **2009**, 81, 2760–2767.

(8)   Min, D.-H.; Su, J.; Mrksich, M. *Angew. Chem., Int. Ed.* **2004**, 43, 5973–5977.

(9)   Derda, R.; Musah, S.; Orner, B. P.; Klim, J. R.; Li, L.; Kiessling, L. L. *J. Am. Chem. Soc.* **2010**, 132, 1289–1295.

(10)   Huh, S.; Chen, H.-T.; Wiench, J. W.; Pruski, M.; Lin, V. S.-Y. *Angew. Chem.*, Int. Ed. **2005**, 44, 1826–1830.

(11)   Banet, P.; Marcotte, N.; Lerner, D. A.; Brunel, D. *Langmuir* **2008**, 24, 9030–9037.

(12)   Huskens, J. *Curr. Opin. Chem. Biol.* **2006**, 10, 537–543.

(13)   Mouawia, R.; Mehdi, A.; Reye, C.; Corriu, R. J. P. *J. Mater. Chem.* **2008**, 18, 4193–4203.

(14)   Hudalla, G. A.; Murphy, W. L. *Langmuir* **2010**, 26, 6449–6456.

(15)   Jacoby, M. *Chem. Eng. News* **2007**, 40–42.

(16)   Love, J. C.; Estroff, L. A.; Kriebel, J. K.; Nuzzo, R. G.; Whitesides, G. M. *Chem. Rev.* **2005**, 105, 1103–1169.

(17)   Bass, J. D.; Katz, A. *Chem. Mater.* **2006**, 18, 1611–1620.

(18)   Hudalla, G. A.; Murphy, W. L. *Langmuir* **2009**, 25, 5737–5746.

(19)   Collman, J. P.; Devaraj, N. K.; Eberspacher, T. P. A.; Chidsey, C. E. D. *Langmuir* **2006**, 22, 2457–2464.

(20)   Bain, C. D.; Whitesides, G. M. *J. Am. Chem. Soc.* **1988**, 110, 6560–6561.

(21)   Kang, J. F.; Liao, S.; Jordan, R.; Ulman, A. *J. Am. Chem. Soc.* **1998**, 120, 9662–9667.

(22)   Scates, B. A.; Lashbrook, B. L.; Chastain, B. C.; Tominaga, K.; Elliott, B. T.; Theising, N. J.; Baker, T. A.; Fitch, R. W. *Bioorg. Med. Chem.* **2008**, 16, 10295–10300.

(23)   Bruner, E. L.; Span, A. R.; Bernasek, S. L.; Schwartz, J. *Langmuir* **2001**, 17, 5696–5702.

(24)   Verkade, J. G.; Lin, V. S.-Y.; Arunkanti, S. Immobilized Iminophosphatranes Useful For Trans-esterification, US 2005/0176978 A1, Aug. 11, **2005**.

(25)   Zhang, F.; Srinivasan, M. P. *Langmuir* **2004**, 20, 2309–2314.

(26)   Lummerstorfer, T.; Hoffmann, H. *J. Phys. Chem. B* **2004**, 108, 3963–3966.

(27)   Collman, J. P.; Devaraj, N. K.; Chidsey, C. E. D. *Langmuir* **2004**, 20, 1051– 1053.

(28)   Fleming, D. A.; Thode, C. J.; Williams, M. E. *Chem. Mater.* **2006**, 18, 2327–2334.

(29)   Devaraj, N. K.; Collman, J. P. *QSAR Comb. Sci.* **2007**, 26, 1253–1260.

(30)   Heise, A.; Stamm, M.; Rauscherc, M.; Duschnerc, H.; Menzel, H. *Thin Solid Films* **1998**, 327-329, 199–203.

(31)   Stokes, G. Y.; Buchbinder, A. M.; Gibbs-Davis, J. M.; Scheidt, K. A.; Geiger, F. M. J. Phys. Chem. A 2008, 112, 11688–11698.

(32)   Mondragon, M. A.; Casta~no, V. M.; Garcia, M. J.; T_ellez, S. C. A. *Vib. Spectrosc*. **1995**, 9, 293–304.

(33)   Costa, C. A. R.; Leite, C. A. P.; Galembeck, F. *J. Phys. Chem. B* **2003**, 107, 4747–4755.

(34)   Nomarua, K.; Gorelika, S. R.; Kurodaa, H.; Nakaia, K. *Nucl. Instrum. Methods Phys. Res., Sect. A* **2004**, 528, 619–622.

(35)   Anderson, M. W.; Klinowski, J. *J. Chem. Soc., Faraday Trans. 1* **1986**, 82, 1449–1469.

(36)   Wollman, E. W.; Kang, D.; Frisbie, C. D.; Lorkovic, I. M.; Wrighton, M. S. *J. Am. Chem. Soc.* **1994**, 116, 4395–4404.

(37)   Oyerokun, F. T.; Vaia, R. A.; Maguire, J. F.; Farmer, B. L. *Langmuir* **2010**, 26, 11991–11997.

(38)   Vrancken, K. C.; Possemiers, K.; Voort, P. V. D.; Vansant, E. F. *Colloids Surf., A* **1995**, 98, 235–241.

(39)   Vrancken, K. C.; Van Der Voort, P.; Gillis-D'Hamers, I.; Vansant, E. F.; Grobet, P. *J. Chem. Soc., Faraday Trans*. **1992**, 88, 3197–3200.

CHAPTER 6

General Conclusions

6.1 General Conclusions

The goal of this thesis was to gain insights into interfacial molecular recognition processes using surface specific spectroscopic techniques such as second harmonic generation (SHG), sum frequency generation (SFG) and X-ray photoelectron spectroscopy (XPS). Exploiting the capability of SHG to probe the interfacial potential, we have addressed some outstanding questions regarding the extent of surface charging of the silica/water interface, which is critical in many geochemical, environmental and industrial applications.[1] Specifically, we explored the effects of cations and anions on the bimodal acid-base behavior of the planar silica/water interface over a broad pH range. Silica is also very commonly used as a support material in many applications ranging from catalysis to diagnostics, where the monolayer on the solid surface acts as the molecular recognition sites. Keeping in mind the importance of molecular recognition properties of DNA in biochip and microarrays, we investigated the hybridization kinetics and thermal dissociation of immobilized DNA at the silica/aqueous phase interface utilizing the molecular specificity of resonantly enhanced SHG spectroscopy. Future work in our group is aimed at studying the behavior of even more complex multifunctional surfaces. To this end we developed a strategy for synthesizing orthogonally reactive self assembled monolayers (SAMs) that represent a general starting point for generating many bifunctional surfaces. The experimental results for all these projects have been discussed in chapters 2 to 5. In the following, the significant results of this thesis that could contribute to the

better understanding of molecular recognition processes at the confined environment of the interface are summarized.

Using nonresonant SHG, we monitored the change in surface charge density of the silica/aqueous phase interface over a broad pH range in the presence of different cations and anions. Previous studies had shown that planar silica possesses more and less acidic sites with pK_a values of ~4 and ~9, respectively, which were attributed to two different hydrogen-bonding environments of the surface silanol groups. We observed that the alkali chlorides play a substantial role in determining the acidity of the surface sites, especially for the less acidic sites, which we attribute to the variable affinities of the cations for the siloxides surface. For instance, the effective pK_a of less acidic silanol groups increased by 2.5 pH units when simply NaCl was replaced with CsCl in the aqueous phase, indicating that the silica/$CsCl_{aq}$ interface was significant less acidic. Moreover, the relative populations of the two acidic sites were found to be very sensitive to the cation identity at the interface as the percentage of more acidic silanol groups varied form 20% to 60% for different silica/aqueous phase interfaces. We explained that this change in bimodal distribution of the acidic sites was because of the different extent of influence of the cations on the hydrogen-bonding structure of the interfacial water molecules. By examining the shifts in effective pK_a values while varying the concentration of the salts we proposed two different mechanisms that are plausible depending on the identity of the cations. These results indicated that the acid-base equilibria and the bimodal distribution of the acidic sites at the silica/water interface are strongly ion specific.

201

Therefore, the surface charge density, that strongly controls the binding behavior of silica, can vary widely at the same pH depending on the alkali present in the aqueous phase. These observations could be vital in accurate modeling of numerous geochemical and environmental processes such as surface dissolution[2] and pollutant transport.[3]

Despite the fact that the anions are not expected to have electrostatic interactions directly with the negatively charged silica surface, our SHG and SFG investigations on the acid-base behavior of the silica/water interface discovered that the behavior of this interface is highly specific to the anions. Specifically, we observed that both types of acidic silanols were very sensitive to the size or polarizability of the halides present at the interface. As we varied the halide from chloride to iodide, the pH at which half the acidic sites dissociated ($pH_{0.5}$) shifted to lower pH for the more acidic sites, whereas it shifted to higher pH for the less acidic sites. We also observed a major increase in sharpness of the titration curves as the halide size increased, which is a consequence of positive cooperativity. By applying a simple cooperative model we quantified the cooperative unit for the dissociation of the more acidic surface sites, which were ~1, 2 and 3 for the sodium chloride, bromide and iodide electrolytes, respectively. These results suggested that the larger halides formed structures at the interface that facilitated positive cooperativity between neighboring silanol groups for the more acidic sites. We also observed that the fraction of these more acidic sites increased dramatically from 20% to 86% as the sodium halide was varied from chloride to iodide. We reasoned this observed change in relative population of silanol groups

202

by stating that the larger halides with lower free energy of hydration were capable of influencing the hydrogen-bonding structure at the interface in such a way that preferred the creation of more acidic sites over less acidic sites. Finally, these experiments provided us with a complete picture of the surface charge density over a broad pH range in presence of halides that could be useful in predicting many geochemical processes. The drastic effects of the halides on silica/water interface indicated that the influence of the anions must be considered in addition to cations to accurately model the surface charge density of negatively charged surfaces like silica above pH 2.

In addition to the surface specificity of SHG, this spectroscopic technique can also be molecule specific when the SHG wavelength is in resonance with the electronic transition of a particular molecule. By combining these two advantages of surface specificity and molecular specificity, resonant SHG is able to observe molecular recognition processes at the silica/water interface. To utilize SHG to study the molecular recognition of DNA strands where one strand was immobilized to the surface while the complement was in the solution phase, we functionalized the solution-phase strand with a commercially available SHG-active 3-nitropyrrole nucleotide, so that hybridization and thermal dissociation could be observed in real-time from the change in SHG signal. We found that the rate of hybridization for surface tethered DNA is much slower than the rate for solution DNA as also described in previous research of DNA duplexes at the gold/aqueous interface.[4,5] Moreover, the dissociation temperature of DNA immobilized at the silica/water interface is significantly lower than the analogous

203

duplex in solution. This decrease in melting temperature is more significant than that observed on other surfaces like gold indicating the destabilizing effect of silica, which we attributed to its negatively charged surface at neutral pH that repels the hybridizing complementary DNA. These observations on silica-supported DNA could be of pronounced interest in optimizing chip-based DNA biodetection platforms using DNA chips and microarrays.

After studying the molecular recognition processes at a monofunctional surface, our next goal was to deal with more complex bifunctional surfaces, which are desirable in many applications ranging from catalysis[6] to biodiagnostics.[7,8] To accomplish this objective azide and amine trimethoxysilanes were self-assembled to generate mixed monolayers on silica. We demonstrated that the orthogonal reactivity of azide and amine functional groups with alkynes and acid chlorides, respectively, allowed these monolayers to be a general platform for bifunctional surfaces. Using XPS, we quantified the ratio of amines and azides in the mixed monolayers and demonstrated how to tune their surface ratio by varying their ratio in the self-assembly mixture. The subsequent functionalization of the azide-amine surface resulted in a bifunctional surface that has a similar triazole/amide ratio to the azide/amine precursor SAMs demonstrating the generality of our approach. The exploitation of orthogonal reactivity as described in this thesis for making mixed monolayers should work with other reactive pairs beside azide and amine. Furthermore, the method that we presented herein to characterize the reactivity and surface ratio of the functional groups in mixed monolayers using XPS ought to be useful to many other substrates with different pairings of functionalities.

To summarize, one of the greatest accomplishments of this thesis has been the discovery of the specific ion effects that influence fundamental surface properties of silica like their ability to become charged, which is important to accurately predict a range of processes, from dissolution kinetics to pollutant transport. The strong dependence of the surface charge properties on the ions present at the interface may change the fundamental understanding of the geochemistry at the mineral oxide/aqueous phase interfaces. Another major achievement of this work is the use of a resonant SHG method for probing DNA recognition processes in real time removing the difficulties of studying DNA immobilized on insulating glass surface. Our findings suggest that the thermal dissociation temperature of the DNA immobilized on silica is significantly lower than what people observed on other surfaces like gold. This result could be vital in designing the DNA microarrays that are widely used in biodiagnostics and molecular biology. Last but not the least, the orthogonally reactive azide-amine mixed monolayers that we developed in this thesis could be used to generate more complex bifunctional surface, the behavior of which our group is aimed to study in future.

6.2 References

(1)   Stumm, W.; Morgan, J. J. *Aquatic Chemistry: Chemical Equilibria and Rates in Natural Waters; Third Edition*; Wiley, **1995**.

(2)   Karlsson, M.; Craven, C.; Dove, P. M.; Casey, W. H. *Aquat. Geochem.* **2001**, *7*, 13.

(3)   Appelo, C. A. J.; Postma, D. *Geochemisytry, Groundwater and Pollution*; 2 ed.; A. A. Balkema Publishers: Amsterdam, **2005**.

(4)   Meunier-Prest, R.; Raveau, S.; Finot, E.; Legay, G.; Cherkaoui-Malki, M.; Latruffe, N. *Nucleic Acids Res.* **2003**, *31*, e150.

(5)   Surkus, A.-E.; Flechsig, G.-U. *Electroanalysis* **2009**, *21*, 1119.

(6)   Huh, S.; Chen, H.-T.; Jerzy W. Wiench; Pruski, M.; Lin, V. S.-Y. *Angew. Chem., Int. Ed.* **2005**, *44*, 1826

(7)   Mrksich, M.; Whitesides, G. M. *Trends in Biotechnol.* **1995**, *13*, 228.

(8)   Frisk, M. L.; Tepp, W. H.; Johnson, E. A.; Beebe, D. J. *Anal. Chem.* **2009**, *81*, 2760.